

November 2019

LASTI Annual Report

Laboratory of Advanced Science and Technology for Industry
University of Hyogo

Vol.20 (2018)



PREFACE

This annual report reviews the research activities of the Laboratory of Advanced Science and Technology for Industry (LASTI) in the academic year of 2018 which is from April 2018 to March 2019) including research activities using NewSUBARU light source at the SPring-8 site and other research activities of the micro and nanoscale are carried out energetically at the Center for Advanced Science and Technology (CAST) II.

NewSUBARU facility has a 1.0-1.5 GeV electron storage ring, which provides light beams from IR to Soft X-ray regions, and the largest synchrotron light facility operated by the university in Japan.

The researches which are carried out are the light sources for next generation through a machine R and D, and the industrial applications such as EUVL lithography, LIGA process, material analysis.

The annual report describes mainly that topics of the NewSUBARU research activities of this year including 1) the research and development of gamma ray application at BL1 beamline, 2) the next generation lithography by Extreme UltraViolet (EUV) lithography at BL3, BL9B, BL9C, and BL10 beamlines, 3) Lithographie, Galvanoformung, and Abformung (LIGA) process technology at BL2 and BL11 beamlines, 4) the chemical analysis using soft X-ray absorption fine structure at (BL5, BL9A, and BL7 beamlines and soft X-ray emission spectroscopy at BL5 and BL9A beamlines at soft X-ray energy region.

Most of our research activities are being conducted in collaboration research works with industries, research institutes, and other universities, inside and outside Japan.

We will continue to respond to the community's demand by offering new science and novel technology.



Takeo Watanabe

A handwritten signature in black ink that reads "Takeo Watanabe". The signature is fluid and cursive, with a long horizontal stroke at the end.

Director of Laboratory of
Advanced Science and
Technology for Industry,
University of Hyogo

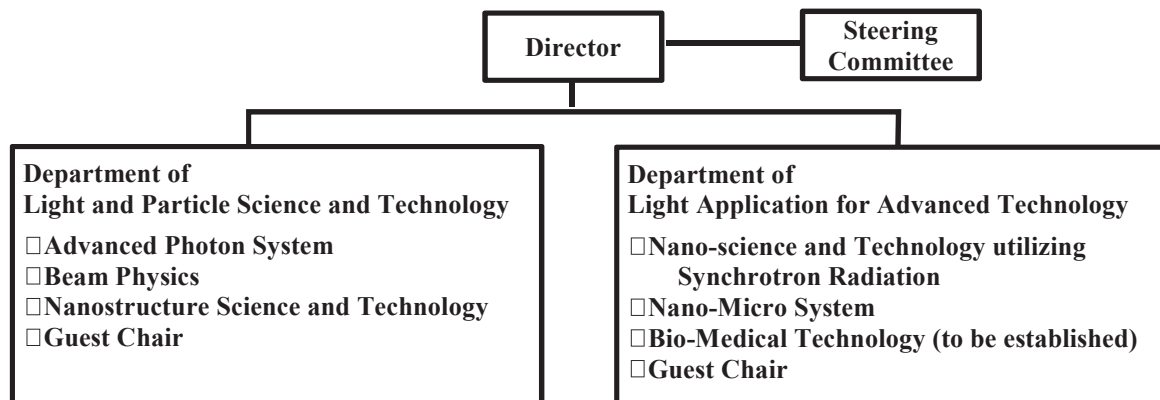


Staff of NewSUBARU
(In front of Advanced Research Building)



The Organization of Laboratory of Advanced Science and Technology for Industry University of Hyogo

The organization



Staff (FY 2018)

Research and faculty staff

WATANABE Takeo, Professor, Director
MIYAMOTO Shuji, Professor
KANDA Kazuhiro, Professor
UTSUMI Yuichi, Professor
SUZUKI Satoru, Professor
NIIBE Masahito, Associate Professor
SHOJI Yoshihiko, Associate Professor
HARUYAMA Yuichi, Associate Professor
YAMAGUCHI Akinobu, Associate Professor
AMANO Sho, Research Associate
HASHIMOTO Satoshi, Research Associate
HARADA Tetsuo, Research Associate

Specially appointed staff

TERANISHI Nobukazu, Professor

Administrative staff

HAYASHI Masahiko, General Manager
ISHIHARA Yasunori, Manager
KAYAHASHI Hidetoshi, Chief
KUWATA Ayami, NewSUBARU
HASEGAWA Miwa, CAST
AKAMATSU Sumiyo, CAST
SAKASHITA Yukiko, CAST
KONO Kimi, CAST
MITOME Naruhito, CAST
SENBA Ayako, CAST
KUSUMOTO Kumi, CAST

Coordinator

FUKADA Noboru, NewSUBARU
FUKUOKA Takao, CAST

Guest staff

MOCHIZUKI Takayasu, Professor
FUKUSHIMA Sei, Professor
OHKUMA Haruo, Professor
ASANO Yoshihiro, Professor
BAN Hiroshi, Professor
KUDOU Hiroto, Professor
WATANABE Yoshio, Professor
HORIBE Hideo, Professor
HARADA Yoshihisa, Professor
NAMAZU Takahiro, Professor
SUGIYAMA Munehiro, Professor
NAGATA Yutaka, Assistant Professor
IKEMOTO Yuka, Assistant Professor
MORIWAKI Taro, Assistant Professor

Contact address

Advanced Research Building

3-1-2 Kouto, Kamigori-cho, Ako-gun, Hyogo, 678-1205 JAPAN.
T:+81-791-58-0249 F:+81-791-58-0242

NewSUBARU Synchrotron Radiation Facility

1-1-2 Kouto, Kamigori-cho, Ako-gun, Hyogo, 678-1205 JAPAN.
T:+81-791-58-2503 F:+81-791-58-2504

Web URL <http://www.lasti.u-hyogo.ac.jp/>, <http://www.lasti.u-hyogo.ac.jp/NS/>

e-Mail lasti@lasti.u-hyogo.ac.jp

Access <http://www.lasti.u-hyogo.ac.jp/NS-en/access/>

CONTENTS

PREFACE

ORGANIZATION of LASTI

Part 1. Current Status of NewSUBARU and Other Light Source

NewSUBARU Storage Ring	1
Satoshi HAsimoto (<i>LASTI/University of Hyogo</i>)	

NewSUBARU Beamlines	4
Masahito Niibe (<i>LASTI/University of Hyogo</i>)	

Part 2. Research Activities

Study of laser Compton gamma-ray in side-pumping using laser-diode-array	12
Sho Amano (<i>LASTI/Univ. Hyogo</i>)	

New challenge of GiPS measurement for bulk alloys using LCS gamma beam at NewSUBARU

BL01	14
K. Sugita ¹ , S. Miyamoto ² , M. Terasawa ² , and F. Hori ¹ (¹ <i>Osaka Prefecture Univ.</i> , ² <i>LASTI/Univ. Hyogo</i>)	

XAFS Measurements with atmospheric pressure measurement system in BL05A	16
T. Hasegawa ^{1,2,3} , S. Fukushima ^{1,2,3} , and K. Kanda ³ (¹ <i>Synchrotron Analysis L.L.C.</i> , ² <i>Kobe Material Testing Laboratory Co., Ltd.</i> , ³ <i>LASTI/Univ. Hyogo</i>)	

Refractive-index changes in SiO₂ Films by Undulator Radiation with a multilayer spectrometer ...	18
K. Moriwaki ¹ , S.Tanaka ¹ , and K.Kanda ² (¹ <i>Kobe Univ.</i> , ² <i>LASTI/Univ. Hyogo</i>)	

Polymerization of pentacene-related molecules by soft X-ray irradiation	20
Akira Heya ¹ , Ryo Yamasaki ² , Naoto Matsuo ¹ , and Kazuhiro Kanda ³ (¹ <i>Eng./Univ. Hyogo</i> , ² <i>Tocalo Co., Ltd.</i> , ³ <i>LASTI/Univ. Hyogo</i>)	

Production of a high energy γ beam via backward Compton scattering of soft X-rays from a short undulator	22
---	----

Norihito Muramatsu¹, Masahiro Okabe¹, Shinsuke Suzuki², Schin Daté², Hajime Shimizu¹, Haruo Ohkuma³, Kazuhiro Kanda⁴, Shuji Miyamoto⁴, Tetsuo Harada⁴, Takeo Watanabe⁴, Manabu Miyabe¹, and Atsushi Tokiyasu¹
(¹Tohoku Univ., ²JASRI/SPring-8, ³Osaka Univ., ⁴LASTI/Univ. of Hyogo)

Determination of the valence band and Fermi level of organic-inorganic lead halide perovskite materials by soft X-ray photoelectron spectroscopy.....	24
Naoyuki Shibayama ^{1,2} , Yuichi Haruyama ³ , and Seigo Ito ¹ <i>(¹Eng./Univ. of Hyogo, ²The Univ. of Tokyo, ³LASTI/Univ. of Hyogo)</i>	
Evaluation of La doping effect in Sr₂IrO₄.....	26
R. Horie ¹ , S. Tsunoda ¹ , Y. Haruyama ² , and J. Akimitsu ¹ <i>(¹Okayama Univ., ²LASTI/Univ. of Hyogo)</i>	
Quasi-free-standing monolayer hexagonal boron nitride on Ni.....	28
Satoru Suzuki ¹ , Yuichi Haruyama ¹ , Masahito Niibe ¹ , Takashi Tokushima ¹ , Akinobu Yamaguchi ¹ , Yuichi Utsumi ¹ , Atsushi Ito ² , Ryo Kadowaki ³ , Akane Maruta ³ , and Tadashi Abukawa ³ <i>(¹LASTI/Univ. of Hyogo, ²Eng./Univ. of Hyogo, ³Tohoku Univ.)</i>	
Growth and Decomposition of Hexagonal Boron Nitride in the Diffusion and Precipitation Method Studied by X-ray Photoelectron Spectroscopy.....	32
Satoru Suzuki and Yuichi Haruyama (<i>LASTI/Univ. of Hyogo</i>)	
Analysis of chemical reactions at the Au-thin-film/Si interface by soft x-ray photoelectron spectroscopy under steam ambient.....	36
Tomoki Yamamoto ¹ , Satoshi Toyoda ² , Satoru Suzuki ¹ , Hirosuke Sumida ³ , Susumu Mineoi ³ , Kazushi Yokoyama ¹ , Akitaka Yoshigoe ⁴ , and Shizuka Nishi ⁴ <i>(¹LASTI/Univ. of Hyogo, ²Tohoku Univ., ³Mazda, ⁴JAEA)</i>	
Soft X-ray absorption and Emission Spectroscopy of Monolayer and Few-layer Graphene Sheet... 	38
Masahito Niibe ¹ , Satoru Suzuki ¹ , and Shin-ichi Honda ² <i>(¹LASTI/University of Hyogo, ²Eng./Univ. of Hyogo)</i>	
Photopolymer Technology for Extreme Ultraviolet Lithography.....	41
Takeo Watanabe and Tetsuo Harada <i>(Center for EUV lithography, LASTI/Univ. of Hyogo)</i>	
Diffraction Efficiency Measurement of a Transmission Grating for 10-nm EUV Resist Evaluation.....	47

Mana Yoshifuji, Shota Niihara, Tetsuo Harada, and Takeo Watanabe
(Center for EUV lithography, LASTI/Univ. of Hyogo)

Deterioration Analyses of CFRP Surface	51
Hideo Kobayashi ¹ , Yosuke Azuma ¹ , Shogo Suehiro ¹ , Sohta Hamanaka ² , Yuki Tobita ² , Takuya Motokawa ² , and Yasuji Muramatsu ² (¹ Sumika Chemical Analysis Service, Ltd., ² Eng./Univ. of Hyogo)	
Soft X-ray absorption measurements of self-standing polyethylene thin films using a transmission method	53
Yuya Matsumoto and Yasuji Muramatsu (Eng./Univ. Hyogo)	
Surface structural analysis of nanodiamond by using soft X-ray absorption spectroscopy and the first principle calculations	55
Tatsuki Maeda and Yasuji Muramatsu (Eng./Univ. Hyogo)	
Direct detection of PM2.5 collected on insulating membrane filters using a total-electron-yield soft X-ray absorption spectroscopy	57
Takuya Motokawa and Yasuji Muramatsu (Eng./Univ. Hyogo)	
Soft X-ray spectroscopy of coal tars	59
Kosuke Shirai and Yasuji Muramatsu (Eng./Univ. Hyogo)	
Controllability of copper particle synthesized by X-ray radiolysis using synchrotron radiation ...	61
Akinobu Yamaguchi ¹ , Ikuo Okada ² , Ikuya Sakurai ² , Takao Fukuoka ¹ , and Yuichi Utsumi ¹ (¹ LASTI/Univ. Hyogo, ² Nagoya Univ.)	
Deposition of Polytetrafluoroethylene Film via Synchrotron Radiation	63
Masaya Takeuchi, Akinobu Yamaguchi, and Yuichi Utsumi (LASTI/Univ. Hyogo)	
Modification of optical property of a Polytetrafluoroethylene by Synchrotron Radiation	66
Masaya Takeuchi, Akinobu Yamaguchi, and Yuichi Utsumi (LASTI/Univ. Hyogo)	
List of publications	
(1) Papers	70
(2) International meetings	75
(3) Academic degrees	80

Part 1. Current Status of NewSUBARU and Other Light Source



Staff of NewSUBARU
(In front of NewSUBARU Facility)

NewSUBARU storage ring

Satoshi Hashimoto
LASTI, University of Hyogo

1. Introduction

NewSUBARU synchrotron light facility has a 1.5 GeV electron storage ring, which is the largest accelerator among universities in Japan. The general layout of the ring is shown in Figure 1. The ring is consisted with 6 DBA cells with an inverse bending magnet with auxiliary coil. There are 6 straight sections between each cell, and they are used for an injection septum, an accelerating RF cavity, two undulators and a laser Compton scattering gamma ray source. Electrons are injected from the linac of SPring-8 through the beam transport line (L4BT). The main parameters are listed in Table I.

Table I Main parameters of the NewSUBARU storage ring

Circumference	118.73 m
Lattice	DBA + inv. Bends
Number of bends	12
Radius of curvature	3.217 m
RF frequency	499.955 MHz
Harmonic number	198
Betatron tunes	6.29(H), 2.22 (V)
Number of IDs	2
Radiation loss per turn	33.4 keV (@1.0GeV)

2. Operation Status

The ring has two operation modes for user-time, 1.0 GeV top-up mode and 1.5 GeV current decay mode. The basic operation time is 9:00 - 21:00 of weekdays. Monday is used for machine R&D, Tuesday is for 1.5 GeV user time, Wednesday and Thursday are for 1.0 GeV top-up user time, Friday is for 1.0 GeV or 1.5

GeV user time. Night period or weekend is used for machine study and user time with the special mode, such as a single bunch operation and a changing the electron energy, if necessary. Range of the electron energy is from 0.5 GeV up to 1.48 GeV with 1 MeV step.

The total machine time in FY2018 was 1922 hours, 78.1% of that of FY2017, excluding the beam down time. Figure 2 shows the breakdown of operation time of the electron storage ring. The beam down time includes not only the down by a failure, but also off-beam periods by a beam abort or others due to the beam instability. The total down time due to the machine trouble in FY2018 was 39hours, 2.0 % of the total operation time.

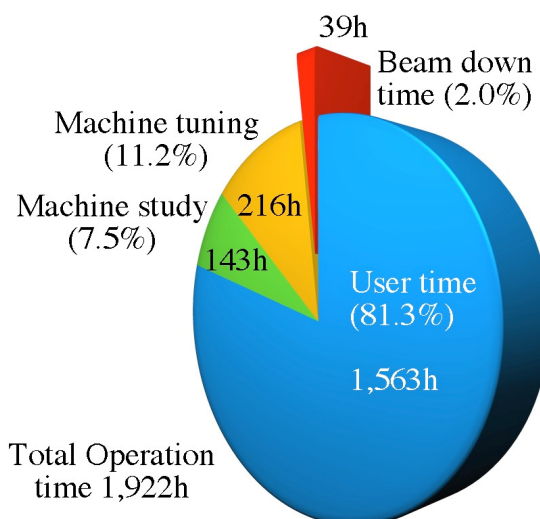


Fig.2 Operation time of NewSUBARU in FY2018.

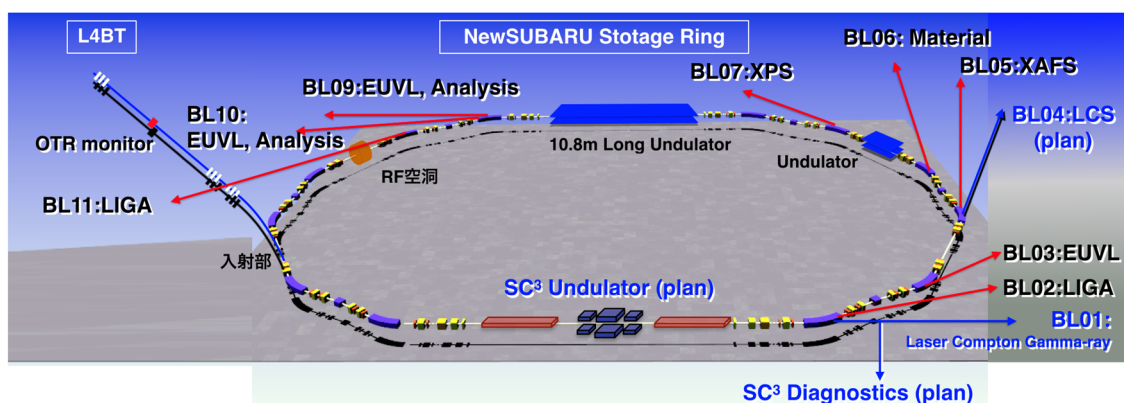


Fig.1 General layout of the NewSUBARU storage ring. Electron beams are injected from the 1.0 GeV linac of SPring-8 to the ring through L4BT beam transport line.

3. Machine Trouble

The typical hardware troubles in FY2018 were as follows.

3-1. Instability of the switching power supply for auxiliary coil of the inverse bending magnet.

This power supply occasionally oscillated at low operation current. In addition to changing the deceleration sequence to keep a sufficient current in auxiliary coil even at low energy operation, the trouble was settled by turning off a feedback circuit that induces the oscillation in the power supply.

3-2. Failure of bump magnet power supply.

One of the four bump magnets was failed due to the broken of the control power supply. All four control power supplies were replaced with new ones. And the stored beam current was reduced several times at the moment of beam injection. This was due to aged deterioration of thyatron in a power supply for bump magnet No.4. We replaced with spare parts.

3-3. RF related issues.

RF synthesizer generating 500 MHz signal was failed and replaced with the new one. And some modules consisting the timing circuit were replaced with the new ones.

3-4. Interlock alarm of power supplies.

Power supplies for quadruple magnet families often showed "Heat" alarm at start up time. The automatic startup sequence was often stopped due to this alarm. We are planning to update the quadruple power supplies.

4. Machine Study

In this section, several topics of the machine R&D are reported.

4-1. SC³ project

Under the collaboration with RIKEN and University of Hyogo Graduate School of Material Science, we have started SC³ project, where the generation of the extremely short radiation pulse corresponding to only a few wavelengths will be experimentally proved at NewSUBARU using tapered undulators, a magnetic chicane and a chirped seed laser. The new ID is under construction and will be installed in March 2020.

4-2. Stabilization of energy ramping.

The NewSUBARU ring can be operated with stored energy from 0.5 to 1.5 GeV after an

injection at 1.0 GeV. The energy ramping is executed according to the pre-defined ramping parameters. However, the reproducibility of ramping using these parameters is not so good all year around due to seasonal small changes of environmental temperatures and a ring circumference. Beam lifetime reduction or stored beam current decrease often occurred during ramping.

To solve this problem we have used a few parameter-sets, which properly depend on the season. Further, to reduce human error and tuning time, we have advanced the automation of ramping process. The first is automatic generation of the new data set from the standard data set that is well tuned. The second is the automatic generation of steering magnet parameters. The third is real-time betatron tune correction during energy ramping mentioned in the next section.

By combining the above three methods, the stability of the energy ramping can be drastically improved.

4-3. Betatron tune feedback

Betatron tunes drift and fluctuate due to stored current, energy ramping, filling pattern, ID gap and so on. These also depend on the small change of environmental temperatures in a year and a day.

To solve this problem, we have been developing the real-time tune measurement and feedback correction system. Development of this system was completed in FY2018. Using this system, the averaged injection efficiency from the linac to the ring could be increased from 80 to over 90 %. By keeping tunes to optimized values, the beam lifetime also could be kept high. This system was developed on PXI platform. The use of this system during the user time will start in October 2019.

4-4. Automatic ramping operation for gamma-ray experiments.

The energy of Compton gamma photon can be continuously changed by changing the stored electron beam energy. In search of the dependency on Gamma-ray energy, users had to stop and restart ramping process manually. It required lots of operational procedures.

We have solved this problem by developing the automatic ramping operation of the ring for the Gamma-ray energy dependency experiments. Using this system, users can start energy dependency experiments only by clicking a button. Once an experiment starts, all procedures such as ramping, measurement and

correction of electron beam orbit, measurement and correction of betatron tune and Gamma-ray measurement in BL01 are automatically repeated. This not only reduce operational costs, but also improves the reproducibility and accuracy of energy scans measurements.

5. New Building for Injector

In March 2019 the new building was completed adjacent to the existing L4BT tunnel. This building would be used as a klystron gallery for the new 1.0 GeV injector.



Fig. The new building for klystron gallery.

Acknowledgements

We are greatly thanks to Prof. Shuji Miyamoto of LASTI for his all activities in our laboratory. The stable operation of the ring is largely due to Dr. Yasuyuki Minagawa, Mr. Kazuyuki Kajimoto and Mr. Yousuke Hamada of JASRI. We also would like to thanks to all the staff of RIKEN and JASRI for their co-operation in the operation of our facility and the construction of the new building for klystron gallery.

Beamlines

Masahito Niibe
LASTI, University of Hyogo

The arrangement of the beamlines in the NewSUBARU synchrotron radiation (SR) facility is shown in Fig.1. Total nine beamlines are operating in the NewSUBARU SR facility.

Four beamlines of BL01, 03, 06 and 11 were constructed until 1999. Three beamlines of BL07, 09 and 10 were started the operation from 2000.

BL02 beamline was constructed for the usage of LIGA in 2003.

BL03B beamline branched from the BL03 beamline propose for the usage of the EUVL (extreme

ultraviolet lithography) microscope for the EUVL finished mask inspection.

BL05 beamline was constructed in response to a demand in the industrial world in 2008, which is the enhancement of the analysis ability in the soft X-ray region with the development of nanotechnology.

BL09B beamline branched from BL09 beamline for the usage of the EUV interference lithography to evaluate. And BL09C beamline branched from BL09B beamline for the usage of the thickness measurement of the carbon contamination originated to the resist outgassing during the EUV exposure.

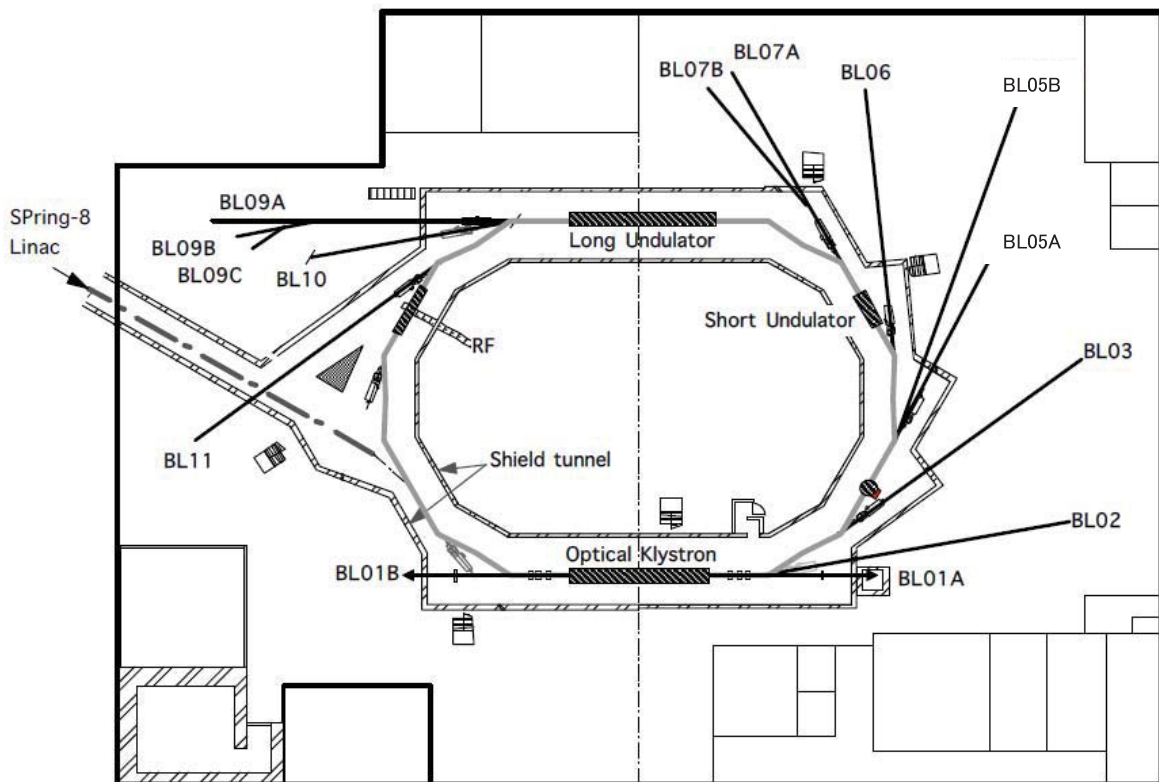


Fig. 1 Beamline arrangement in NewSUBARU.

I. BL01

BL01 is a beamline for research and developing new light sources. This beamline is one of two long straight section on NewSUBARU. Optical klystron was installed at this straight section. Upstream side of this beamline (BL01B) is intended to be used for visible and infrared light generated from free electron laser (FEL) or synchrotron radiation (SR). Downstream side of this beamline (BL01A) is used for laser Compton scattering gamma-rays source. Gamma-ray beamline hutch just outside of the storage ring tunnel was constructed in

Table 1. Specification of BL01 gamma beam

CO ₂ laser 10.52 □m 5W	Gamma energy : 1.7 - 4 MeV Gamma flux* : 9 x10 ⁶ γ/s : 6 x10 ⁵ γ/s (1.5-1.7 MeV) (with 3mmφ collimator)
Nd laser 1.064 □m 0.532 □m 5 W	Gamma energy : 17 - 40 MeV Gamma flux* : 7.5 x10 ⁶ γ/s : 3 x10 ⁵ γ/s (15-17 MeV) (with 3mmφ collimator)

*Electron beam energy : 1-1.5 GeV

*Electron beam current : 250 mA

*Gamma-ray beam divergence : 0.5 mrad

2004 for gamma-ray irradiation experiments. Specification of this gamma-ray sources are listed in Table 1. New gamma-ray irradiation hutch "GACKO" was installed at BL01A, collaborating with Konan University. Table 2 shows the specification of "GACKO".

Table 2. Specification of "GACKO"

Maximum gamma-ray power	0.33 mW
Maximum gamma-ray energy	1.7 MeV - 73 MeV
CO ₂ laser, wavelength/power	10.59 μm / 10W
1-1.7MeV gamma-ray flux	2×10 ⁷ γ/sec@10W/300mA
Nd:YVO ₄ laser, wavelength/power	1.064 μm/ 30W, 0.532 μm/20W
10-17 MeV gamma-ray flux	5×10 ⁷ γ/sec@30W/300mA

II. BL02

The LIGA (abbreviated name of Lithographic, Galvanoformung and Abformung) process which consists from deep X-ray lithography, electroforming, and molding process is one of the promising candidates for such 3D microfabrication. More than hundreds aspect ratio for microstructure can be attained by the usage of the higher energy X-rays (4-15 keV) from synchrotron radiation (SR) with deeper penetration depth to the photosensitive resist. In this system we have succeeded to enlarge the exposure area up to A4 size and the fabrication dimension from submicron to millimeter by varying the energy of the X-ray source in accordance with the size of desired microparts. Microstructure with high aspect ratio over several hundred will be achieved using the X-rays over 10 keV since high energy X-ray has deep penetration depth to the photo-sensitive resist materials. Whereas, in the case of lithography for low energy X-rays from 1 keV to 2 keV, submicron structures with high aspect ratio will be achieved

using the X-rays mask with precise line-width and thinner absorber, since low energy X-rays has low penetration depth. Based on this principle, the beamline for x-ray exposure have constructed with continuous selectivity of X-rays from 100 eV to 15 keV by using the X-ray mirrors (plane and cylindrical mirror) and Be film filters. The horizontal angle of the outgoing SR could be obtained up to 12.5 mrad, which corresponds to the horizontal size of 220 mm (A4 horizontal size) at the exposure position. The second characteristic performance of the beamline is the high efficiency differential pumping system. This was necessary for maintain the vacuum difference between the storage ring (<10⁻⁹ Pa) and the end-station (<10⁻⁹ Pa) at which gasses for substrate cooling will be introduced in the exposure apparatus.

The flexibility for the shapes and functions of microstructure will be enlarged by achieving 3D microfabrication process using multi step exposure at various configuration between X-ray mask and

substrates. The relative positions between X-ray mask and substrates, tilt and rotation angle to the SR incident direction can be moved simultaneously during SR exposure using 5 axis stages. The movement of each axis is controlled by the PC in terms of the scanning speeds, scanning length, and

repetition number. In order to decrease the heat load of sample substrate suffered during SR irradiation helium introduction and substrate cooling mechanism were also equipped. Specification of spectrometer is listed in Table 3.

Table 3. Specification of the LIGA exposure system

Optics	Plane and cylindrical mirror, Be filters
Exposure energy	100 - 2 keV, and 4 – 15 keV
Exposure method	Proximity and multi-step exposure
Wafer size	A4 or 8 inch
Exposure area	230 mm(H) ×300 mm(V)
Exposure environment	< 1 atm (He-gas)

III. BL03

BL03 is a beamline for the developing the next generation lithographic technology so called extreme ultraviolet (EUV) lithography. The extreme ultraviolet lithography (EUVL) is a promise technology for fabricating a fine pattern less than 7-nm node. There are (1) a EUV resist-sensitivity evaluation tools, (2) a VUV reflectometer, and (3) an EUV microscope with Schwarzschild optics. At (1) tool, EUV resist is exposed with SR light of EUV monochromatized by 7 Mo/Si multilayer mirrors. The exposure spectrum of this tool was same as the ASML exposure tools. The monochromator of (2) reflectometer was UV – VUV reflectometer. At EUV

lithography, out-of-band radiation (100 – 300 nm) of EUV source degrades image quality. Thus, optics and resist property of out-of-band region was essential to evaluate, for example EUV mask reflectivity, and EUV resist sensitivity. The monochromator specification was shown in Table 4. The EUV microscope (3) has Schwarzschild optics, which were fabricated with collaboration of Dr. Toyoda (Tohoku Univ.). The spatial resolution was quite high of less than 28 nm, which was equal to 7 nm at wafer printing size.

Table 4. VUV monochromator specification

Mount type	Collimate plane grating monochromator
Grating	Plane Grating (1,000 l/mm)
Energy range	4 - 120 eV (UV ~ VUV)
Resolving power (E/ΔE)	~1000

IV. BL05

BL05 was constructed in response to a demand in the industrial world, which is enhancement of the analysis ability in the soft x-ray region with the development of nanotechnology. BL05 consists of two branch lines for use in the wide range from 50 eV to 4000 eV. BL05A and BL05B are designed to cover the energy range of 1300-4000 eV and 50-1300 eV, respectively. The incident beam from the bending magnet is provided for two branch lines through different windows of a mask. Therefore, these two branch lines can be employed simultaneously. At the end stations of each branch, the transfer vessel systems were mounted for the measurements of

sample without exposure to air. In addition, globe box was placed for the preparation of samples into transfer vessel.

1) The double crystal monochromator was installed at the BL05A. InSb, Ge, Si, SiO₂, Beryl and KTP crystals are prepared for a double-crystal monochromator. Toroidal mirrors are used as a pre-mirror and a focusing mirror of BL05A. XAFS measurement in the total electron yield mode and fluorescence XAFS measurement using SSD (SII Vortex) can be performed. The fluorescence XAFS spectra can be measured for samples at the end station

filled with He gas. Table 5 shows the specification of monochromator.

Table 5. Monochromator specification

Monochromator	Double crystal monochromator
Monochromator crystals	SiO ₂ (1010) , InSb (111) , Ge (111) , Beryl (1010) , KTP (110) , Si (111)
Energy range	1300-4000 eV
Resolution	$E/\Delta E=3000$

2) The constant-deviation monochromator consisting of a demagnifying spherical mirror and a varied-line-spacing plane grating (VLSPG), which can provide high resolution, simple wavelength scanning with fixed slits, was mounted on BL05B. The optical system consists of a first mirror (M0), a second mirror (M1), an entrance slit (S1), a pre-mirror (M2), and three kinds of plane grating (G), an exit slit (S2) and a focusing mirror (M3). The including angle of the monochromator is 175°. Two measurement

chambers are prepared at the end station of BL05B. The XAFS spectra in the total electron yield mode and fluorescence XAFS spectra using SDD (Ourstex) can be measured in a high vacuum chamber. In addition, the photoelectron spectrum can be measured using spherical electron analyzer (VG Sienta, R3000) in an ultrahigh-vacuum chamber. The chambers can be replaced by each other within 1 hour. Table 6 shows the specification of the monochromator.

Table 6. Monochromator specification

Monochromator	Varied-line-spacing plane grating monochromator
Grating	100 l/mm, 300 l/mm, 800 mm/l
Energy range	50-1300 eV
Resolution	$E/\Delta E=3000$

V. BL06

BL06 has been mainly developed for irradiation experiments such as photochemical reaction, SR-CVD, photo-etching, surface modification. The white radiation beam from bending magnet is introduced to the sample stage using a pair of mirror, whose incident angle was 3°. The SR at BL06 sample stage had a continuous spectrum from IR to soft x-ray, which was lower than 1 keV. A differential pumping system can

be utilized for experiments in a gas atmosphere, which is difficult in the soft x-ray region. A sample holder can install four pieces of samples at a time. By using heater set in the sample holder, the sample can be heated from room temperature to 220°C. The temperature of sample is monitored using a Cr-Al thermocouple mounted on the sample holder.

VI. BL07A and BL07B

This beamline was designed for the development of new materials by SR technology. This beamline consists of two branch lines, which are provided with an incident beam from a 3-m-long undulator by switching the first mirror. One of them is a high photon-flux beamline with a multilayered-mirror monochromator for the study of SR-process (BL07A) and another is a high-resolution beamline with a varied line spacing grating monochromator for the evaluation of nano-structure characteristics by SR-spectroscopy (BL07B). The useful range of emitted

photons from 50 to 800 eV is covered at both beamlines. The light source of BL07 is a 3-m length planar undulator, which consists of 29 sets of permanent magnets, a period length of which is 76 mm. The incident beam from the undulator is provided for two branch lines by translational switching of first mirror.

1) BL07A

The multilayered-mirror (MLM) monochromator, which has high reflectivity in the soft X-ray region, was installed at the BL07A. It consists of a switching mirror chamber, a slit chamber, a MLM monochromator, a filter chamber and a reaction chamber. To obtain a large photon flux, we decided to use only first mirror (switching mirror), M0, for focusing. The MLM monochromator is designed to cover an energy range of up to about 800 eV by combination of three kinds of mirror pairs with 4 kinds of filter. The flux deliver by this design is estimated to be between a maximum of 10^{17} photons/s

at 95 eV and a minimum 2×10^{14} photons/s at 300 eV for a 500 mA ring current. Table 7 shows the summary of BL07A. In addition, X-ray fluorescence (XRF) apparatus using spherical varied line spacing grating was mounted at the downstream of irradiation chamber. The poly capillary was used to enhance beam-condensing efficiency. Measurement energy range was from 30 eV to 450 eV. This XRF apparatus was expected to utilize the chemical analysis on the light metals, Li and Be, and light elements, B, C and N.

Table 7. Summary of BL07A.

Energy range (eV)	Multilayer mirror					Filter	
	Material	spacing	Thickness Ratio	number of layers	$\Delta E/E$	material	Thickness
50-60	Mo/Si	20 nm	0.8	20	6.2 %	Al	100 nm
60-95						None	—
90-140	Mo/B ₄ C	11 nm	0.5	25	3.3 %	Ag	100 nm
140-194						Cr	500 nm
190-400	Ni/C	5 nm	0.5	60	2.5 %	Ni	500 nm
400-560							
550-800							

2) BL07B

The constant-deviation monochromator consisting of a demagnifying spherical mirror and varied line spacing plane grating (VLSPG), which can provide to high resolution, simple wavelength scanning with fixed slits, was mounted on BL07B. The optical system consists of a first mirror (M0), an entrance slit (S1), a premirror (M1), and three kinds of plane grating (G), an exit slit (S2) and two focusing mirrors (M2 and M3). The monochromator is

designed to cover the energy range 50-800 eV with three gratings, of which including angle are 168° . The VLSPG has been well known to obtain high resolution in extreme ultraviolet region by diminishing various kinds of aberration. The total resolving power about 3000 can be realized in the whole energy region. Table 8 shows the specification of the monochromator.

Table 8. Monochromator specification

Mount type	Hettrick-Underwood type
Grating G1, G2, G3	Plane VLS (600, 1200, 2400 l/mm)
Energy range	50-150 eV, 150 – 300 eV, 300-800 eV
Resolving power (E/ ΔE)	~ 3000

VII. BL09

A purpose of this beamline is studies on a soft x-ray interferometry or a holographic exposure experiment with making use of highly brilliant and coherent photon beams radiated from 11 m long undulator in NewSUBARU.

BL09 consists of M0 mirror, M1 mirror, G grating and M2 mirror. M0 mirror is used for horizontal deflection and beam convergence, M1 is used for vertical beam convergence at the exit slit, and M2 is used for vertical deflection and beam convergence. A monochromator is constructed by M1 and a plane grating. The maximum acceptance of the undulator beam is 0.64 mrad in horizontal and 0.27 mrad in vertical. The acceptance can be restricted by 4-jaw slits equipped at upstream of the M0 mirror.

BL09A beamline is used for material analysis: X-ray absorption spectroscopy (XAS) and X-ray

photoelectron spectroscopy (XPS). In 2013, X-ray emission spectrometer (XES) was introduced at the endstation of the BL-09A. The energy range and resolving power of the XES system was designed to be about 50-600 eV and 1500, respectively.

BL09B beamline branched from BL09 beamline for the usage of the EUV interference lithography for the evaluation of the exposure characteristics of EUV resist. Coherence length of 1 mm at the resist exposure position was achieved using BL09B beamline. And BL09C beamline branched from BL09B beamline for the usage of the thickness measurement of the carbon contamination originated to the resist outgassing during the EUV exposure. Table 9 shows the specification of the monochromator.

Table 9. Monochromator specification

Mount type	Monk-Gillieson type
Grating	Plane VLS (300, 900, 1200 l/mm)
Energy range	50 – 750 eV
Resolving power (E/ΔE)	~3000

VIII. BL10

BL10 is for EUV reflectometry and soft X-ray analysis. M0 mirror is used for horizontal deflection and beam convergence, M1 is used for vertical beam convergence at the exit slit, and M2 is used for vertical deflection and beam convergence. A monochromator is constructed by M1 and a plane grating. At the beginning, the multilayer reflectivity measurement was carried out at this beamline. The characteristics of this beamline and the result of the Mo/Si multilayer measurement are carried out for the development of the EUV-mask technology.

BL10 utilizes a monochromator of the varied-line-spacing plane grating (VLS-PGM). The line density of the monochromator in central region of the gratings were 600, 1800 and 2,400 lines/mm. The reflectometer has a two axis vacuum goniometer. One axis carries the sample, which may be a mirror surface at the center of the reflectometer vacuum chamber (□-motion). The other (□-motion) carries the detector on a rotating arm.

In addition there are linear motions to translate the sample in two orthogonal directions (x,y). All motors are controlled by computer. The reflectivity result obtained at BL10 has a good agreement with that at LBNL. Table 10 shows the specification the monochromator.

The micro-CSM tool was adapted at the most downstream of the BL10 beamline for the EUV mask defect inspection with coherent-diffraction-imaging method. This too is very effective for the inspection of the actinic patterned mask with phase imaging.

A large reflectometer was installed in a branch line for large EUV optical component including EUV collector mirrors. The reflectometer has a sample stage with y, z, □, □, and Tilt axis, which can hold large optical elements with a maximum weight of 50 kg, a diameter of up to 800 mm, and a thickness of 250 mm. The entire sample surface is able to be measured.

Table 10. Monochromator specification

Mount type	Monk-Gillieson type
Grating	Plane VLS (600, 1800, 2400 l/mm)
Energy range	50 – 1,000 eV
Resolving power (E/ΔE)	~1000

IX. BL11

A beam line BL11 is constructed for exposure Hard X-ray Lithography (DXL) in the LIGA (German acronym for Lithographie Galvanoformung and Abformung) process. LIGA process, that utilizes a useful industrial application of SR, is one of the promising technologies for fabrication of extremely tall three-dimensional (3D) microstructures with a large aspect ratio. This process was invented at the Institut Fur Mikrostrukturtechnik (IMT) of the Karlsruhe Nuclear Center (KfK) in 1980. Microstructures with height of over a few hundreds μm have been widely applied to various fields such as micro-mechanics, micro-optics, sensor and actuator technology, chemical, medical and biological engineering, and so on. This beam line was designed by the criteria ; photon energy range from 2 keV to 8 keV, and a density of total irradiated photons $\square 10^{11}$ photons/cm². The BL11 can provide the most suitable photon energy for microfabrication in X-ray lithography, while the BL2 is equipped for fabricating fine pattern submicron-scale structure and microstructure with high aspect ratio by selectivity of X-rays using movable mirror system. That is, LIGA process in NewSUBARU can provide the best 3D microfabrication because the BL11 and

BL2 are complementary. The beamline BL11 is consisting of an absorber chamber, a first-mirror chamber (M1), a 4-way slit chamber, a Be and polyimide window chamber, and an exposure chamber. The horizontal angle of the outgoing SR could be obtained up to 17.8 mrad, providing a beam spot size on the exposure stage $\square 80 \square\square\square\square \text{ mm}^2$. The micron-scale structure with high aspect ratio will be achieved using the toroidal typed mirror M1 which can produce a parallel collimated beam of X-rays. In addition, the homogeneity of the beam is excellently controlled by a novel adding system.

Using the precision stage in the exposure chamber, the flexibility for the shaped and functions of microstructure will be enlarged by achieving 3D microfabrication process using multi step exposure at various configuration between x-ray mask and substrates. The exposure area of 200 mm \times 200 mm is brought to fruition. In order to decrease the heat load of sample substrate suffered during SR irradiation, helium introduction and substrate cooling system were also equipped. The specification of the LIGA exposure system is listed in Table 11.

Table 11. Specification of the LIGA exposure system

Exposure method	Proximity exposure
Wafer size	8 inch
Exposure area	200 mm(H) \times 200 mm(V)
Exposure environment	< 1atm (He-gas)

Establishment of Research Center for Advanced Synchrotron Radiation Analysis

In order to respond to diverse analysis needs from industries, it is necessary to advance technological development for analyzing beamlines (BLs) of NewSUBARU SR facility to advance integrated and strategic development of analyzing technology. For this reason, the Research Center for Advanced SR

Analysis was launched in August 2016. As an organization crossing in university courses, this center is consulted and administered by all members of the LASTI related to analysis, and in collaboration with the SR Nanotechnology Center of Hyogo Prefecture, a wide range of energy from hard X-rays to soft X-rays. We aim to respond to various analysis needs of the area on a one-stop basis.

Acknowledgement

We would like to thank all the staff who work at NewSUBARU synchrotron radiation research facility for their help to describe the update details of the beamlines.

Part 2. Research Activities



M. Takeuchi in a doctor's course of a graduate school won the Best Presentation Award in JCK-MEMS/NEMS 2018"

Study of laser Compton gamma-ray in side-pumping using laser-diode-array

Sho Amano
LASTI, University of Hyogo

Abstract

We propose a new scheme with a “side-on-collision” between an electron-beam and laser beams emitted from high-power laser diode arrays in order to obtain high power laser Compton gamma-ray. To calculate a gamma-ray flux in NewSUBARU, we measured powers, spectra and spatial characteristics of a typical GaAlAs laser diode array. Using the measured results and the data of electron beam at BL01 in NewSUBARU, we calculated a laser gamma-ray luminosity to be 9 photons/mA/W/sec with the “side-on-collision”. This indicates that a laser cavity to enhance Compton backscattering is required in this scheme. We conclude that the “side-on-collision” scheme with the cavity is expected to generate gamma-ray flux more than 10^8 photons/sec.

Introduction

Based on a concept that more gamma-ray flux can be achieved by longer interaction length between electrons and photons, the laser Compton gamma-ray in “NewSUBARU” is generated at a long straight section of a race-track shaped electron-storage-ring. At present, a Nd:YVO₄ laser emitting at a wavelength of 1.06mm and a CO₂ laser at 10.6mm are used mainly. When each laser irradiated, obtained gamma-ray luminosity was 6000 photons/mA/W/sec [1] and 7300 photons/mA/W/sec [2], respectively. At both times, a maximum gamma-ray flux is achieved to be $\sim 10^7$ photons/sec.

The gamma-ray is now used in various applications but much more gamma-ray flux is expected. Then, we considered a novel collision scheme to obtain it. In generally, a “head-on” collision scheme as shown in Fig.1, where a laser beam is incident from an opposite direction toward a relativistic electron beam and collided it (at a point A or B), is used in laser Compton gamma-ray sources in many facilities. In this scheme, however, a number of laser source is limited to be only one, then the laser power of itself has to be increased keeping a good beam quality in order to achieve higher gamma-ray power. But this has a limitation. Therefore, in this study, we considered a “side-on” collision as shown in Fig.2, where laser beams are arranged along an electron beam side, to make a possibility of gamma-ray power scale-up rule. There are few examples of studies of laser Compton source with such 90-angle collision to generate femto-sec gamma-ray short pulse [3] or to diagnose electron beam bunch [4], but we don't know such study as ours for purpose to achieve higher power.

In this study, we developed a code to calculate gamma-ray flux. As the lasers for side-on collision, we considered GaAlAs laser-diode-

array (LDA) and measured its power, spectra and beam characteristics which are required for the calculation. Using these measured results, we simulated a laser Compton gamma-ray generation at the center point of the long straight section (A) in “NewSUBARU”, operating with electron storage energy of 1GeV.

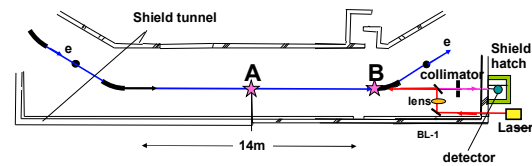


Fig.1 Head-on-collision at NS-BL01 for laser Compton gamma-ray generation (present status).

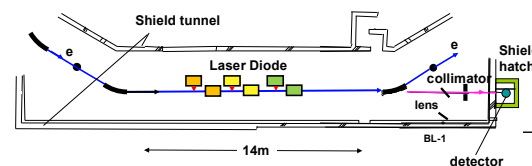


Fig.2 Side-on-collision at NS-BL01 for laser Compton gamma-ray generation (proposal).

Equations

Laser Compton gamma-ray flux n_γ (photons/sec) is expressed by Eq. (1).

$$n_\gamma = c(1 - \beta \cos \theta_1) \sigma \int U_e U_l dV \quad (1)$$

Here, U_e , U_l is a spatial distribution of electron and laser beam, respectively.

Collision cross-section σ can be obtained from differential cross-section of *Klein-Nishina formula*.

$$\frac{d\sigma}{d\Omega} = 2 \left[\frac{r_0 k_2}{x_1 \mu} \right]^2 \left[4 \left(\frac{1}{x_1} + \frac{1}{x_2} \right)^2 - 2 \left(\frac{1}{x_1} + \frac{1}{x_2} \right) - \left(\frac{x_1 + x_2}{x_2 x_1} \right) \right] \quad (2)$$

Here,

$$k_2 = \frac{k_1 (1 - \beta \cos \theta_1)}{\left[1 + k_1 / E - \beta \cos \theta_2 - k_1 \cos(\theta_2 - \theta_1) / E \right]} \quad (3)$$

$$x_1 = -\frac{2\gamma k_1 (1 - \beta \cos \theta_1)}{\mu} \quad (4)$$

$$x_2 = \frac{2\gamma k_2 (1 - \beta \cos \theta_2)}{\mu}$$

k_1, k_2 is a laser and a gamma-ray energy and θ_1, θ_2 is a collision and a scattering angle, respectively. r_0 is a classical electron radius and μ is a rest electron energy. $\theta_1 = \pi$ at a head-on collision and $\theta_1 = \pi/2$ at a side-on collision. And for backscattering, $\theta_2 = 0$.

For a calculation of a gamma-ray flux from Eq.(1), we have to know U_e, U_l . The U_e at the collision point in "NewSUBARU" has been already known [2] and a unknown value of U_l was measured.

Results & Discussion

We considered to use a compact high-power laser source of a linear GaAlAs laser-diode-array, which has an emitting area of $1\text{cm} \times 1\mu\text{m}$. Its output power and spectral wavelength peak was measured to be cw20W and 804 nm, respectively. Figure 3 shows emission spatial patterns measured with pin-hole scanning method. Fitting both the horizontal and vertical patterns to be gaussian curves, spatial propagations characteristics were obtained. From the results, beam wests (horizontal: 6.8 mm, vertical 0.48 μm) and M_2 factors (horizontal: 1.54, vertical 1.1) of the LDA were obtained and we could determine U_l .

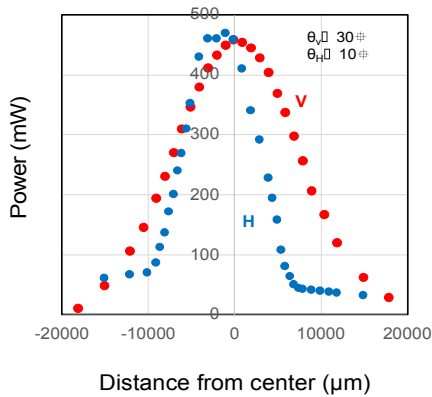


Fig.3 Spatial patterns of the LDA.

Using the measured results of the LDA, we simulated side-on collision at the center point of the long straight section of "NewSUBARU" with the electron energy of 1GeV. As results, it was found that a gamma-ray can be obtained, which has a photon energy of 11 MeV and a luminosity of 9 photons/mA/W/sec. This luminosity value is 3 orders smaller than 7000 photons/mA/W/sec at the present head-on collision. This difference is caused by the short interaction length between the laser and the electron beam. Although the interaction length is ~ 10 m in the head-on collision using the long straight section of "NewSUBARU", the interaction length is only ~ 1 cm of a horizontal diameter of the laser beam in the side-on collision. In conclusion, much gamma-ray flux cannot be obtained in side-on collision by laser single-path.

To overcome the demerit of a short interaction length in side-on collision, we propose to use a laser cavity that lengthen an interaction length. This is an application of a confocal multi-path cavity [5], which was proposed before by an author for head-on collision experiments. In a case study, when the cavity causes 30 times collisions, an electron current is 300 mA, an output power of single LDA is 200W (commercial available) and a number of LDA is 6, a gamma-ray flux is calculated to be 10^8 photons/sec that is on order higher than a present achieved value in "NewSUBARU". And the gamma-ray flux can be increased in proportion to a number of LDA and the gamma-ray power scale-up rule can be established in the side-on collision scherm.

Acknowledgments

This work was supported by the special study foundation of University of Hyogo in 2017 (Leading study A individual).

References

- [1] K. Horikawa *et al.*, Nucl. Instr. and Meth. A **618**, 2010, pp.209-215.
- [2] S. Amano *et al.*, Nucl. Instr. and Meth. A **602**, 2009, pp.337-341.
- [3] Y. Taira *et al.*, Nucl. Instr. and Meth. A **637**, 2011, pp.S116-S119.
- [4] W. P. Leemans *et al.*, Phys. rev. lett. **77**, 1996, pp.4182-4185.
- [5] S. Amano *et al.*, Jpn. J. App. Phys. **40**, 2001, pp.654-6

New challenge of GiPS measurement for bulk alloys using LCS gamma beam at NewSUBARU BL01

K. Sugita^A, S. Miyamoto^B, M. Terasawa^B, F. Hori^A
A: Osaka Prefecture University, B: LASTI, University of Hyogo

Abstract

We have tried a new positron annihilation method by directly implantation the 16.9 MeV Laser Compton scattering gamma beam into the bulk amorphous alloy. This method is called Gamma-ray induced Positron annihilation Spectroscopy (GiPS). GiPS can nondestructively measure the bulk material in the atmosphere. Although the confirmation by the X-ray diffraction of the sample after annealing was the formation of crystals, the result of GiPS suggests that the crystal and amorphous state are mixed in the annealing sample. The high energetic GiPS may give us new information about bulk materials in addition to the conventional positron annihilation method.

Introduction

Positron annihilation spectroscopy (PAS) is used as defects research for various materials such as metallic alloys and semiconductors. In general, positron searches open space type defects such as vacancy, void and open volume in a material with non-destructive. Radioisotope (RI) is usually used as a positron source and sometimes used pair-created positrons from gamma photon. Recently, a new PAS method is proposed, that is positron production by direct implantation of a high energetic gamma ray into a sample and annihilation gamma rays emitted continuously. In this method, positron source is not used but high energetic gamma photon induced positron in a sample is effectively used for positron annihilation. So far, GiPS has developed and succeeded at some facilities [1-3]. In this study, we have tried to perform GiPS for estimation of open volume change in the bulk amorphous alloys using MeV ordered Laser Compton scattering (LCS) gamma ray at NewSUBARU BL01 as a demonstration.

Sample

Bulk amorphous alloy of $Zr_{55}Cu_{30}Ni_{10}Al_5$ and crystalized one by annealing were prepared for positron annihilation measurement as shown in figure 1. The size of these samples is a diameter of 3 cm and a height of 4 cm cylinder shape. These samples were measured by X-ray diffraction, positron annihilation Doppler broadening. For these samples, different open volume exists in have already reported by measuring by using 8 MeV positron beam which is produced by Hori *et al.* at the facility [4].



Fig1. Bulk amorphous alloy (left) and crystalized one by annealing of the amorphous alloy (right).

GiPS setup

Figure 2 shows an illustration of GiPS setup on the BL01 at NewSUBARU. This apparatus has consisted of the sample, HP-Ge detector shielded by Pb block and signal measurement circuit of an amplifier (ORTEC 671) and a multichannel analyzer (Techno AP). Pb blocks surrounding the HP-Ge detector has 3 cm diameter hole faced to a sample as a window of passing the positron annihilation gamma. LCS gamma ray is generated from laser photon and relativistic electron in a storage ring. The energy of LCS gamma ray can be controlled by the wavelength of laser light and kinetic energy of an electron. In this measurement, using a wavelength of 1064 nm Nd:YVO₄ laser and energy of 982 MeV circling electron in the storage ring, 16.9 MeV gamma ray is produced and implanted it into directly. The implanted gamma ray is high enough to pass through the few mm thickness sample.

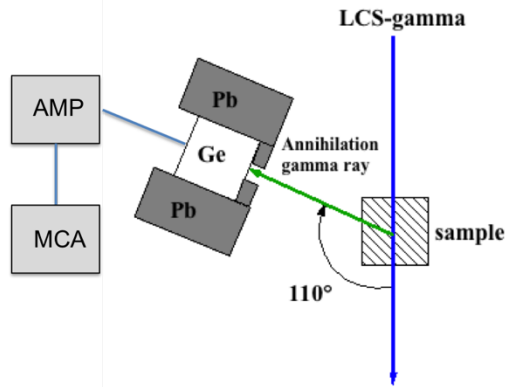


Fig2. Schematic illustration of the GIPS measurement system constructed at BL01 in NewSUBARU.

Measurement

We have measured positron annihilation Doppler broadening spectra for bulk amorphous and crystal alloy samples by GiPS as mentioned above. Figure 4 shows the positron annihilation Doppler spectra in bulk amorphous and crystal alloys. In this figure, the solid line and the broken lines are the amorphous alloy and the crystal alloy, respectively. The peak value of amorphous alloy is slightly higher than that of crystal alloy. These profiles are analyzed for S-parameter which is defined as annihilation ratio of the center part of the spectra. S-parameter is defined as MCA channel number from 1346 to 1350. S-parameter of the amorphous alloy is larger than that of crystal alloy as shown in table 1. This result shows that the amorphous alloy has a vacancy type of open space. This open space in this alloy corresponds to the free volume in amorphous reported by other positron measurements [4].

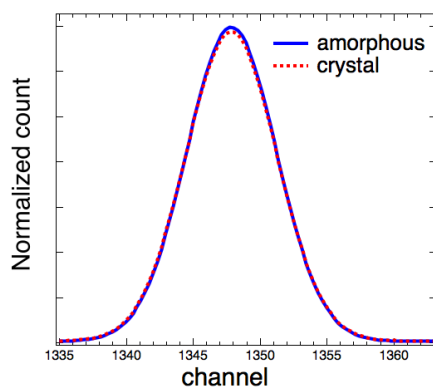


Fig3. Positron annihilation Doppler profiles in the amorphous alloy and crystallized one.

Table 1. S parameter of the sample.

Sample	S parameter
amorphous	0.486
crystal	0.480

Reference

[1] M. Butterling *et al.*, Nucl. Inst. and Meth. in Phys. Research B **269**(2011)2623-2629.
 [2] Y. Taira *et al.*, Rev. Sci. Instrum. **84**, 053305(2013).
 [3] K. Sugita *et al.*, LASTI Annual Report vol.19(2017) pp23-24.
 [4] F. Hori *et al.*, Jour. of Phys. Conf. Series **674**(2016)012025.

XAFS Measurements with atmospheric pressure measurement system in BL05A

T. Hasegawa^{1,2,3}, S. Fukushima^{1,2,3} and K. Kanda³

¹Synchrotron Analysis L.L.C., ²Kobe Material Testing Laboratory Co., Ltd., ³LASTI, University of Hyogo

Abstract

BL05A is a double crystal monochromator (DCM) beamline of NewSUBARU for X-ray absorption fine structure (XAFS) spectroscopy in the soft X-ray region. This beamline is available for atmospheric pressure measurements under He gas in a sample chamber with beryllium window. We tried to apply a liquid cell to measure the spectra of real samples and evaluated practical analysis with the cell. The diesel engine oils before and after the car running were used as real samples. Consequently, this cell enabled us to measure the spectra for the chemical states of elements in the oils.

Introduction

X-ray absorption fine structure (XAFS) spectroscopy has been applied to analyze the local structure and the electronic states of elements. XAFS measurement is a powerful tool for analyzing the characterization of materials, because it can investigate the local structure near specific atoms. XAFS measurements for the soft X-ray are most frequently performed under vacuum conditions. Because the energy range of this X-ray is harder to pass through the air, but it can travel in a vacuum efficiently. For that reason, it is difficult to be adapted for measurements of liquid sample and wet sample. But transmission rate of this X-ray become dramatically better under He gas compared with the air. Therefore, XAFS measurements under atmospheric pressure in He gas are normally performed for these samples. We have equipped BL05A of NewSUBARU with a sample chamber for atmospheric pressure measurement system to respond needs for industrial users. In addition, we succeeded in XAFS measurements of the standard aqueous solution by making the sealed cell for containing the liquid. In the next stage of the measurements, we tried to apply the liquid cell to the real samples and analyze the elements including in them. In this paper, we report on the preliminary research of the liquid samples for practical analysis of XAFS under atmospheric pressure.

Experiments

BL05A of NewSUBARU, a branch line of BL05, is a double crystal monochromator (DCM) beamline for XAFS spectroscopy [1, 2, 3]. BL05A is applied five different crystals to covers the X-ray energy range from 950 eV to

4150 eV. XAFS measurements can be performed in these energy range at the Na-, Mg-, Al-, Si-, P-, S-, Cl-, K- and Ca-*K* edges. BL05A is available for atmospheric pressure measurements under He gas. A beryllium window with thickness 45 μm is used to separate a high vacuum in the beamline from a He atmosphere in the sample chamber (Fig.1). This window is brazed high-vacuum gate valve with the front of the chamber. We have succeeded to make the polyethylene cell for liquid sample and performed XAFS measurements of various aqueous solutions in user analyses. We tried to apply the liquid cell to measure the spectra of the real samples through the use of diesel engine oils. The engine oils before and after the car running were prepared for the experiments, 0 km and 56,260 km running, respectively.

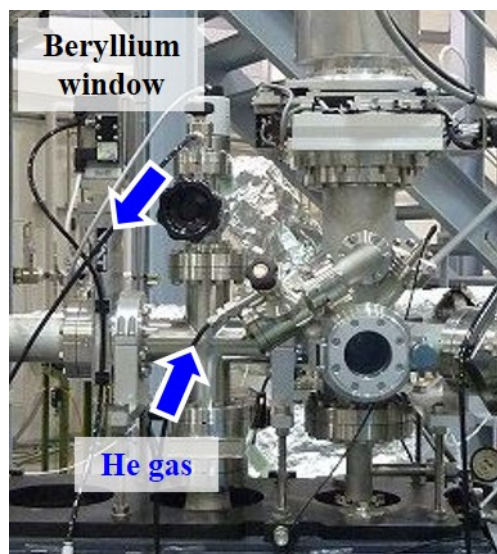


Fig.1 A sample chamber for atmospheric pressure measurement system.

These oil samples were injected into the polyethylene sheet sealed with a heat sealer by using a plastic syringe and mounted to a holder with double-sided conductive tape. X-ray fluorescence (XRF) and XAFS analysis were attempted to evaluate practical analysis with the cell in BL05A.

Results

The results of XRF spectra of the engine oils before and after the car running and the polyethylene sheet used in the cell measured in atmospheric pressure with He gas are shown in Fig.2. XRF is measured using SII Vortex silicon drift detector with 3100 eV incident beam. The measurement live time for each sample was set at 100 seconds. XRF spectra is indicated that several elements are present in the oils. Si was detected both in the oils and in the polyethylene sheet. On the other hand, P and S detected in the oils weren't virtually absent in the polyethylene sheet. The results of S-K edge XANES spectra of the engine oils before and after the car running and reference samples measured in atmospheric pressure with He gas are shown in Fig.3. The spectra of these samples were measured with the partial fluorescence yield mode by InSb (111) crystal. The oxidation state of organic and inorganic S species is commonly known as the oxidation numbers between -2 and +6. The spectra show that there are multiple oxidation states of sulfur in the oils that is higher than the oxidation number in S_8 . In addition, the peak at 2481.7 eV for S^{6+} in sulfates of engine oil after the car running is increased compared to before one. In this preliminary research, we succeeded to obtain the spectra for the chemical states of sulfur in oils and confirmed that this cell is applicable to practical analysis of XAFS under atmospheric pressure.

References

- [1] T. Hasegawa *et al.*, *Advances in X-ray Chem. Anal. Jpn.*, **41**, pp.99-106 (2010) [in Japanese].
- [2] K. Kanda *et al.*, *J. Phys.: Conf. Ser.*, **425**, 132005/1-4 (2013).
- [3] T. Hasegawa *et al.*, *LASTI Annual Report*, **vol.17**, pp.16-17 (2015).

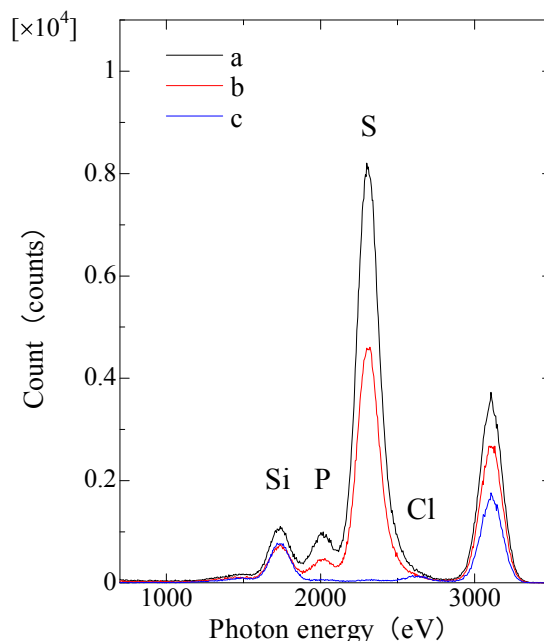


Fig.2 XRF spectra of the engine oils, (a) 0 km, (b) 56,260 km running and (c) polyethylene sheet used in the cell.

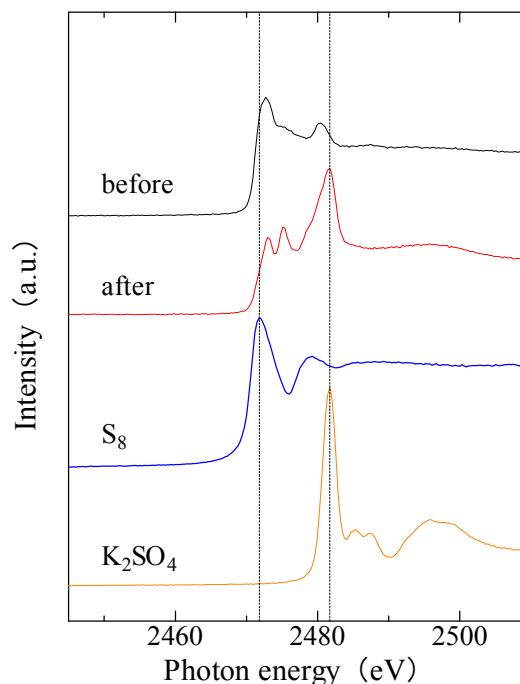


Fig.3 S-K edge XANES spectra of the engine oils before and after the car running and reference powder samples.

Refractive-index changes in SiO₂ Films by Undurator Radiation with a multilayer spectrometer

K. Moriwaki¹, S. Tanaka¹, and K. Kanda²

¹Graduate School of Eng., Kobe University, ²LASTI, University of Hyogo

Abstract

Undurator radiation (UR) with a multilayer spectrometer by the NewSUBARU (BL7A) is used for SiO₂ modification that can be applied to photonic devices. The measured refractive indices do not show sharp peaks by varying the UR peak-energy, although it has a slight increase in the lower peak-energy range. Optical absorbance is measured after the UR radiation, because defects generated in the SiO₂ films may be the main cause of the refractive index changes. Correlation between the optical absorbance increases and the refractive-index increase is found, while it is a slightly dispersive relation. An island-like morphology is found on the surface for UR irradiated samples without spectrometer that suggests nonuniform surface reduction.

Introduction

Synchrotron radiation (SR) and undurator radiation (UR) can be used especially for radiation-induced material modifications in SiO₂ material for optical devices like optical waveguides^{1,2)}. UR is a very useful tool for the material modifications, because it can select a useful wavelength, and has very high intensity. By using a multilayer spectrometer, UR becomes more useful for the device applications, because the most suitable wavelength without higher order ones can be used. The former experiments revealed various refractive index changes by the UR radiation with and without a spectrometer^{1,2)}. In this report, refractive-index modification effects are mainly investigated further, especially for irradiating peak energy dependences and for depth profiles by etching the samples

Experiments and Results

Thermally grown SiO₂ films (0.5 μm thickness) on Si substrates and fused quartz substrates were used for the UR radiation (BL-7A) with and without the spectrometer. UR with peak energy ranging from 80 to 390 eV is used with the spectrometer including the 3rd and the 5th order peaks. Irradiated samples were characterized by refractive-index measurements using a reflection spectrophotometry, optical absorption spectroscopy and atomic force microscopy (AFM).

Very high refractive index changes after the irradiation by UR without the spectrometer were found in the sample surface that were mainly by the surface reduction layer having Si-Si bonds¹⁾. By using UR radiation with the spectrometer, Si-Si bonds were not found, so that the refractive index rises were not as high as those without the spectrometer¹⁾. For those samples with the Si-Si bonds on the surface, AFM is used to find the surface morphology. Figure 1 shows the results

that suggest the nonuniform modification layer. Figure 1 shows surface morphology map of 2x2 μm² area, and a surface profile on the horizontal line shown in the map. It may mean that the reduction layer with Si-Si bonds is not uniform and has islands on the surface. It will be determined by measuring surface map of Si and O elements in the future.

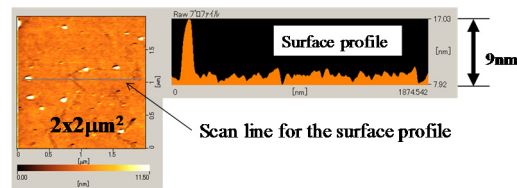


Fig.1 Surface morphology map (left) of 2x2 μm² area for a sample irradiated by UR without the spectrometer, and a surface profile (right) on the horizontal line shown in the map.

Figure 2 shows refractive index changes for an irradiated SiO₂ film as a function of the UR peak energy. The results in Fig. 2 shows relatively flat dependence on the peak energy, although it has a slight increase in the lower energy range. In those measurements, the refractive index values can be determined precisely²⁾ (1x10⁻³ or less) utilizing the accurate value of thermally grown SiO₂-films thickness (500 nm). The reason of the slight increase in the lower energy range is not clear yet.

Defects in SiO₂ films after UR radiation would be the main origin for the refractive index changes. Those defects can be measured by optical absorption measurements. By measuring optical absorbance for irradiated quartz substrates, a correlation between it and the

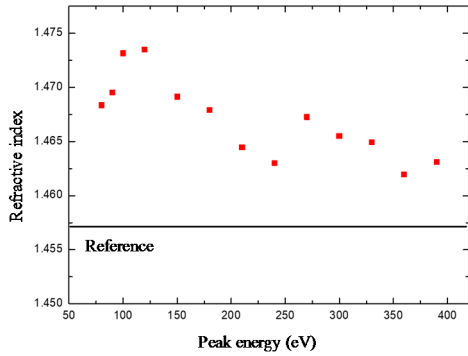


Fig.2 Refractive index changes at $\lambda=633\text{nm}$ for SiO_2 films after irradiation by UR with the spectrometer as a function of peak energy at a dose of $500 \text{ mA}\cdot\text{h}$.

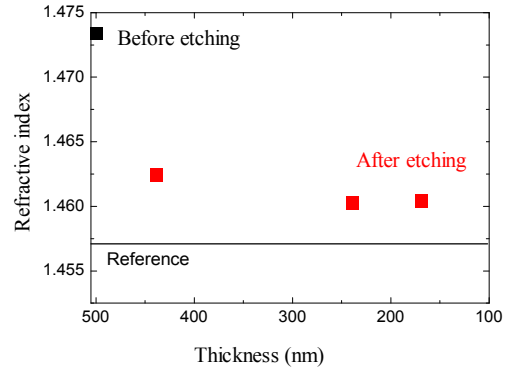


Fig.4 Refractive index changes in SiO_2 films after UR radiation with the spectrometer at a peak energy of 120 eV and a dose of $500 \text{ mA}\cdot\text{h}$ before and after etching.

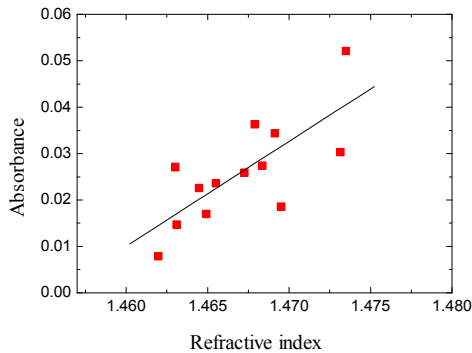


Fig.3 Correlation between absorbance and refractive-index changes for samples after irradiation by UR with the spectrometer. Absorbance peaks at a wavelength of 210 nm are used.

refractive index changes is found as shown in Fig. 3. Although the measured points in Fig. 3 are distributed around a linear line and are not so simple, the correlation is clear. It is not clear whether specific defects cause the refractive index changes or not.

For optical device applications, depth profile of the refractive index changes in the irradiated samples is extremely important. Figure 4 shows a measured depth profile where refractive indices are shown for samples before and after etching 3 times. The refractive indices are measured in Fig. 4 after etching the sample by 60 nm , 260 nm and 330 nm respectively. The refractive index decrease is sharp even after the 60 nm etching. It means that the refractive-index change region is not so deep so that an application to optical devices is not so easy, because it usually needs μm -deep changes for the application. Figure 5 shows results that also indicates the shallow

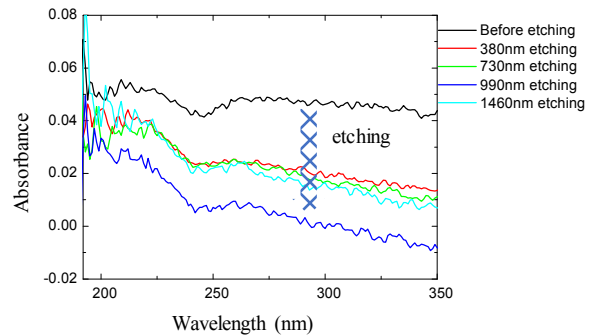


Fig.5 Optical absorbance for samples irradiated by UR with the spectrometer (at a peak energy of 120 eV and a dose of $500 \text{ mA}\cdot\text{h}$) before and after etching 4 times.

refractive index changes by measuring optical absorbance before and after etching the quartz substrates 4 times. Further investigation is necessary for an application to optical devices

Conclusions

SiO_2 films were irradiated by UR with and without the spectrometer, and characterized mainly by their refractive index changes. The refractive index changes were precisely analyzed at less than 1×10^{-3} . Refractive index changes as a function of photon peak energy showed relatively flat dependence without sharp resonant peaks. For a mechanism to increase the refractive index, further investigations are necessary. The authors thank R.Fujiwara for his help in the experiments.

References

- [1] K.Moriwaki et al., LASTI Annual Report vol.18 (2016)43.
- [2] K.Moriwaki et al., LASTI Annual Report vol.19 (2017)33.

Polymerization of pentacene-related molecules by soft X-ray irradiation

Akira Heya¹, Ryo Yamasaki², Naoto Matsuo¹, Kazuhiro Kanda³

¹ Graduate School of Engineering, University of Hyogo, ² Tocalo Co., Ltd., ³ LASTI, University of Hyogo

Abstract

We have tried to fabricate graphene nanoribbons (GNRs) from pentacene molecules by soft X-ray irradiation. The nanocarbon film consisting of pentacene (Pn) and 6,13-dihydropentacene (DHP) was prepared by hot mesh deposition (HMD). The nanocarbon film consisting of Pn and DHP was changed by soft X-ray irradiation. The combination of HMD and soft X-ray irradiation is expected as a novel method for GNR fabrication.

Introduction

The nanographene molecules are attractive two-dimensional materials consisting of carbon atoms arranged in a hexagonal lattice. The graphene nanoribbons (GNRs) have band gaps that depend on the ribbon width. Therefore, GNRs are expected to be used in next-generation semiconductor devices as part of logical elements, transistors, spin transistors, and gas sensors.

Several fabrication methods for GNR, including the patterning of graphene sheets by lithography, unzipping carbon nanotubes, and bottom-up processing using a precursor with a hexagonal lattice have been investigated.

We have also investigated the fabrication method of GNRs using pentacene (Pn), H₂ gas and W mesh. This method is named hot mesh deposition (HMD) [1]. The 6,13-dihydropentacene (DHP) was generated from Pn by HMD. In addition, we discovered that the threshold temperature for crystallization of inorganic semiconductor materials (Si, Ge and SiGe films) was reduced by irradiation of soft X-ray with high photon flux density generated from synchrotron facility NewSUBARU [2]. Therefore, the combination of HMD and soft X-ray irradiation is expected as novel method for GNR fabrication method.

In this study, we have tried to fabricate GNRs from pentacene by using HMD and soft X-ray irradiation.

Experimental

A W mesh (10×55 mm²) with a wire diameter of 0.1 mm and 30 holes/inch was used. Ni particles were supported on the W mesh surface with an atmospheric plasma spray. A mixture of Ar and H₂ was used as the plasma generation gas. The plasma power was 38.5 kW. The Ni was supported on both faces of the W mesh with supported Ni area ratios of 3% were prepared.

The HMD apparatus is already shown in

elsewhere [1]. The deposition of nanocarbon film was performed using a pentacene source. A W_{Ni(3%)} mesh was set between the pentacene source in a Mo boat and a quartz substrate 20×20 mm² in size. The flow rate of H₂ and gas pressure were 400 sccm and 30 Pa, respectively. The distance between the mesh and the quartz substrate was fixed at 100 mm. A pentacene source (30 mg) in a Mo boat was placed in a 26-mm diameter quartz tube. To vaporize the pentacene molecules, the Mo boat was heated to 315°C using a coil heater. The deposition time was fixed at 300 s. The W_{Ni(3%)} mesh temperature (T_{mesh}) was 1450 °C.

The irradiation of soft X-rays was carried out at BL07A of NewSUBARU. The light source of BL07A was a 2.28 m undulator. The storage-ring energy was 1 GeV. The beam size measured with a fluorescent plate on the sample surface was 7.5 × 7.5 mm². The photon energies was 300 eV. The storage-ring current and dose were 300 mA and 400 mA h, respectively.

The property of nanocarbon film was measured by laser desorption/ionization mass spectrometry (LDI-MS). The change in molecular structure by soft X-ray irradiation was evaluated by UV-Vis absorption spectroscopy and Raman scattering measurement.

Results and discussion

The LDI-MS spectra of the nanocarbon film prepared by HMD are shown in Figs. 1(a) and (b). The intensities from Pn and DHP were not significantly different. The Pn molecules likely came into contact with the heated Ni surface, and some became DHP at a T_{mesh} of 1450 °C. Conversely, the pentacene molecules that come in contact with the heated bare W surface did not decompose. From the Fig. 1(b), pentacene monomers and pentacene multimers (PMs) were generated under the present deposition conditions. Although the ratio of multimers to monomers was low as 11%, a nanocarbon film consisting

primarily of PMs was obtained from the pentacene source on the quartz substrate without a metal catalyst. The ratio of Pn : DHP: PMs was estimated to be approximately 0.5 : 0.4 : 0.1 from LDI-MS spectrum.

The UV-Vis spectra are shown in Fig. 2. The amorphous carbon (a-C) film prepared by reactive heating is also shown as a reference. The peak due to conjugated double bond was not observed in a-C film. On the other hand, the absorption peaks due to conjugated double bonds were observed in the UV region of both of before and after soft X-ray irradiation. The absorption peak changed from a sharp peak at 272 nm to a broad peak over visible region. The sample color was changed from light brown to black as shown in Fig. 2.

The Raman spectra of the nanocarbon film prepared by HMD before and after soft X-ray irradiation are shown in Fig. 3. The peaks due to Pn at 1179 and 1373 cm^{-1} were not observed before soft X-ray irradiation. It indicates that the molecular orientation of Pn was disordered by existence of DHP and PMs. The Raman spectra drastically changed and the broad peaks attributed to G and D bands were confirmed after soft X-ray irradiation. The polymerization reaction could occur by soft X-ray irradiation. It was considered that the decomposition reaction also occurred by soft X-ray irradiation simultaneously because the peak due to D band was observed.

Conclusions

The nanocarbon film with the ratio of Pn : DHP : PMs of 0.5 : 0.4 : 0.1 was obtained by HMD. Under the present soft X-ray irradiation condition, the polymerization and decomposition (C and H desorption) occurred by soft X-ray irradiation simultaneously. To fabricate the GNRs, it is considered that the control of not only molecular orientation and distribution but also optimization of soft X-ray irradiation are required.

References

- [1] A. Heya, R. Yamasaki, and N. Matsuo, *Thin Solid Films* **675** (2019) 143.
- [2] A. Heya, K. Kanda, K. Toko, T. Sadoh, S. Amano, N. Matsuo, S. Miyamoto, M. Miyao, T. Mochizuki, *Thin Solid Films* **534** (2013) 334.

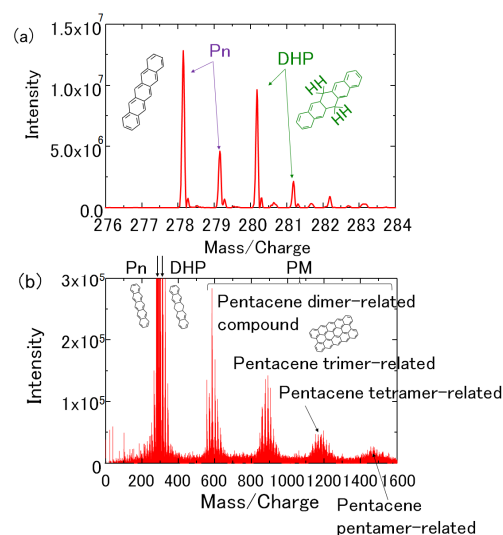


Fig. 1. LDI-MS spectra of the nanocarbon film prepared using the $\text{W}_{\text{Ni}(3\%)}$ mesh. (a) Mass numbers from 276 to 284. (b) Mass numbers from 0 to 1600.

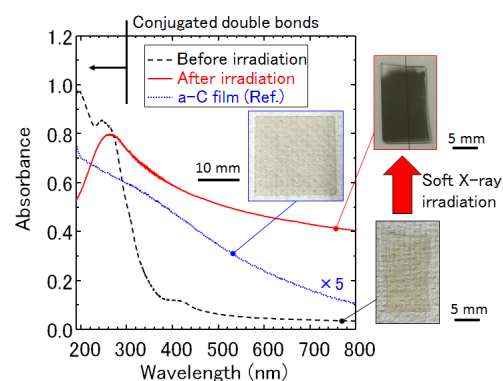


Fig. 2. UV-Vis spectra of the nanocarbon films prepared by HMD before and after soft X-ray irradiation. The a-C film is also shown as a reference. The optical images are also inserted.

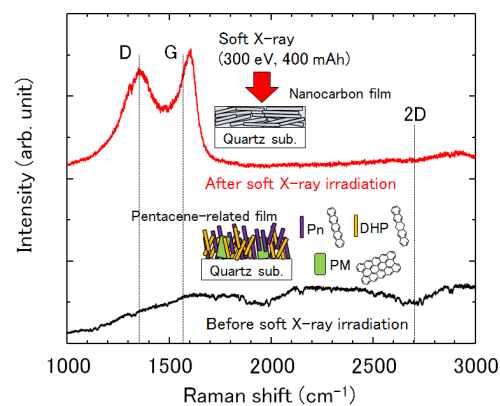


Fig. 3 Raman spectra of the nanocarbon films prepared by HMD before and after soft X-ray irradiation.

Production of a high energy γ beam via backward Compton scattering of soft X-rays from a short undulator

Norihito Muramatsu¹, Masahiro Okabe¹, Shinsuke Suzuki², Schin Daté², Hajime Shimizu¹, Haruo Ohkuma³, Kazuhiro Kanda⁴, Shuji Miyamoto⁴, Tetsuo Harada⁴, Takeo Watanabe⁴, Manabu Miyabe¹, Atsushi Tokiyasu¹
¹ELPH, Tohoku University, ²JASRI/SPring-8, ³RCNP, Osaka University, ⁴LASTI, University of Hyogo

Abstract

A high energy γ beam up to 0.6 GeV can be produced via backward Compton scattering of 92 eV X-rays from 1 GeV electrons at NewSUBARU. The soft X-rays will be obtained from the short undulator at BL07 with the backward reflection using a Mo/Si multi-layer mirror. For this purpose, a cylindrical mirror base to focus X-rays at the straight section has been prepared. In addition, we have carried out the installation of vacuum chambers and the development of several detectors for X-rays and a γ beam.

Introduction

A laser light is usually injected into the electron storage ring for the production of a high energy γ beam via backward Compton scattering. In our project, soft X-rays of about 92 eV are being injected instead in order to obtain much higher energy γ beam for new generation experiments of hadron physics. In case of the 1 GeV operation at NewSUBARU, the energy spectrum of such a γ beam is calculated as shown in Fig.1, where the Compton edge is extended to 585 MeV compared with 51 MeV by the injection of 355 nm ultraviolet laser.

For the demonstration experiment of X-ray Compton backscattering, we plan to use a short undulator (total length: 2.28 m, period length: 7.6 cm) at BL07 as an X-ray source, and then reflect the radiated X-rays backwardly into the original straight section. A Mo/Si multi-layer

mirror will be installed at BL07A for this reflection. A schematic view of our experimental setup is shown in Fig.2.

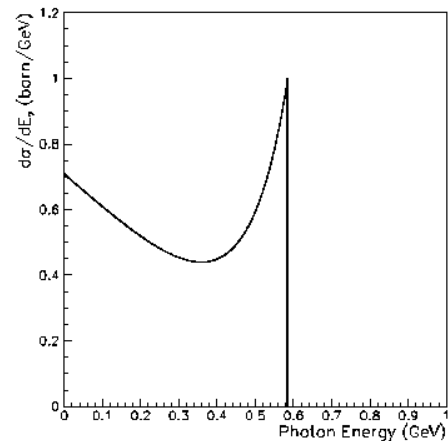


Figure 1 Energy spectrum of a γ beam via backward Compton scattering of 92 eV X-rays from 1 GeV electrons.

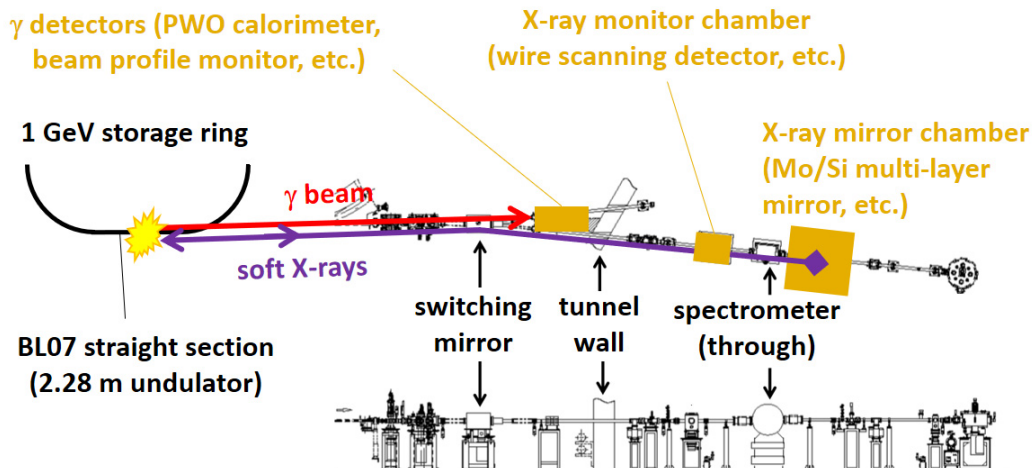


Figure 2 Experimental setup of X-ray Compton scattering at NewSUBARU BL07A.

Summary of achievements

In FY2018, we achieved the following preparation works:

- (1) The experimental setup was designed in detail. Accordingly, two vacuum chambers were newly installed at BL07A. One chamber will be used to set the multi-layer mirror on high precision stages with cooling water circulation. The other will be used for the monitor of radiated and reflected X-rays. A wire scanning detector was installed to measure their profiles with an increase of micro current.
- (2) A base plate for the Mo/Si multi-layer mirror was developed with a low thermal expansion glass ceramic (Zerodur). The reflection surface was formed in a cylindrical shape with a curvature radius of 16.7 m, as a result of the ray trace simulation by SHADOW.
- (3) For the energy measurement of a γ beam produced by backward Compton scattering, a high resolution electromagnetic calorimeter was made by assembling 9 PbWO_4 (PWO) crystals, the individual sizes of which are $20 \times 20 \times 200 \text{ mm}^3$. A γ beam profile monitor was also prepared by crossing 1 mm^2 scintillating fibers in the area of $50 \times 50 \text{ mm}^2$.

Development of an X-ray mirror base

Because the switching mirror of BL07 possesses a spherical surface, the X-rays at our reflection mirror chamber are parallel in the horizontal direction but divergent for the vertical component. This feature was confirmed by the SHADOW simulation, as shown in Fig.3. In order to focus the reflected X-rays at the straight section of BL07, we need a cylindrical mirror with a curvature radius of 16.7 m, which corresponds to the distance between the mirror and the Compton scattering point. A good focusing behavior was also confirmed by SHADOW.

Based on this study, we developed a

Acknowledgments

This research was supported in part by Grant-in-Aid for Challenging Research (Pioneering) No. 18H05325.

cylindrical X-ray mirror base by using a 5 mm-thick and $80 \times 80 \text{ mm}^2$ Zerodur plate. First of all, very thin SUS wires were sandwiched by two Zerodur plates. In the next step, the Zerodur plates were bended by applying a weight of a few tens kg at the edges, as shown in Fig.4. The adjustment of their curvature radius was done by changing the wire radius and the applied weight. The bended state was kept by putting epoxy adhesive between the two plates, and the outside surfaces were mechanically polished to flat planes with a roughness of several nm. The epoxy adhesive was removed by heat to release the bending force. The desired cylindrical mirror surfaces were finally achieved at outsides. The produced curvature was confirmed by measuring a variation of depth on the mirror surface and counting the number of Newton fringes with a flat plate under a Na lamp. The Zerodur plates have been cut in $50 \times 50 \text{ mm}^2$, and they are ready for the multi-layer coating of Mo/Si.

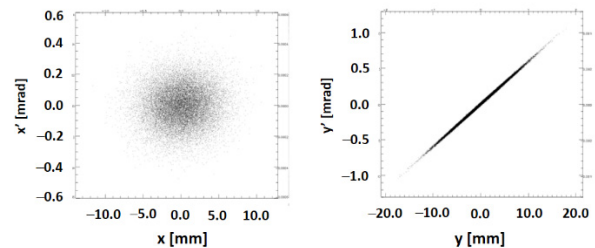


Figure 3 SHADOW simulation result of the X-ray positions and slopes at the reflection mirror chamber in the horizontal (x / x') and vertical (y / y') directions.

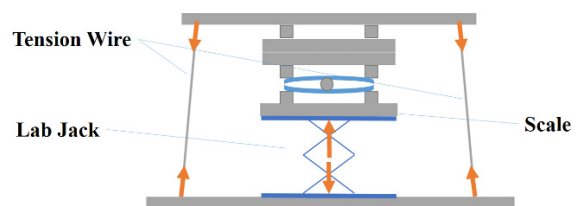


Figure 4 Method to produce two bended Zerodur plates with the application of weight.

References

- [1] <http://www.rcnp.osaka-u.ac.jp/~mura/kaitaku/>

Determination of the valence band and Fermi level of organic-inorganic lead halide perovskite materials by soft X-ray photoelectron spectroscopy

Naoyuki Shibayama^{1,2}, Yuichi Haruyama^{1,3}, Seigo Ito¹

¹Graduate School of Engineering, University of Hyogo, ²Graduate School of Arts and Sciences, The University of Tokyo, ³LASTI, University of Hyogo

Abstract

An understanding of the electronic structure of perovskite materials used in solar cells is essential for their performance improvement. Synchrotron photoelectron spectroscopy was used to experimentally delineate and energy position of the valence band structure and the Fermi level of the perovskite. The valence band of the perovskite was measured using photoelectron spectroscopy with ultraviolet photoelectron spectroscopy (He 1 α line: 21.22 eV) and soft X-rays photon energy (SX-PES: photon energy of 100 eV) and these results were compared. This work is important for the engineering and optimization of solar cells and their semiconductor properties.

1. Introduction

In the recent years, perovskite solar cells (PSCs) based on organic-inorganic halide perovskite absorbers have attracted considerable attention, due not only to their superb photo conversion efficiency but also to the low cost of the source materials. Since the first PSCs with 3.8% were reported by Prof. Miyasaka and co-workers¹, the PSCs conversion efficiency has reached above 24%^{2,3}. This surprising performance improvement is due to the excellent optical and electrical properties of the organometal halide perovskite materials, such as high absorption coefficient, long carrier diffusion length, and low recombination rate.

In the PSCs investigation, the energy diagram of the semiconductor material used for solar cells is important for understanding the charge separation process, and ultraviolet photoelectron spectroscopy (UPS) with He lights sources (21.22 and 40.81 eV) frequently used to obtain such information. A better understanding of the electronic structure of perovskite materials used in PSCs is essential for their performance improvement. In particular, photoelectron spectroscopy (PES) can provide unique information at the atomic level of properties of the interfaces.

In this study, we aimed to establish a method to investigate the valence band of perovskite crystals using soft x-ray photon energy (SX-PES).

2. Experiments

The perovskite polycrystalline thin film used for the measurement was manufactured according to the same experimental conditions and protocol as the previously published literature.⁴ Solutions (1.3 M) of CH₃NH₃PbI₃ of

DMSO were prepared by adding separate materials of PbI₂ and MAI with a molar ratio of 1:1. The FTO glass substrates (TEC-15, NSG-Pilkington) were cleaned ultrasonically with detergent, distilled water, and ethanol respectively, and treated with O₃ for 15 min to eliminate organic impurities and make the surface clean. A solution of CH₃NH₃PbI₃ was spin-coated on the FTO glass with 1000 rpm for 10 sec and with 5,000 rpm for 30 sec, subsequently, inside a drying room with a dewpoint temperature of -30 °C. During the spin coating, toluene was dripped on the perovskite layer. The film was annealed at 60 °C for 10 min and at 100 °C for 15 min, subsequently.

The measurement of SX-PES was performed using NewSUBARU BL07B.

3. Results and Discussion

3.1 Interpretation of the valence band structure

To validity was verified by comparing the valence band of the perovskite polycrystalline thin film obtained by SX-PES with the result of density functional theory (DFT) calculations. The valence band of the perovskite polycrystalline layer was delineated by SX-PES measurements (Figure 1). The results of DFT calculations of the CH₃NH₃PbI₃ model^{5,6} were assigned to the main structures observed in the experimentally observed valence band. The valence band formed from two components consists of the mixed orbital of Pb 6s - I 5p*, and the other component consists of Pb 6s - I 5p. The overlap of these orbitals is broadened in the crystal by dispersion in the band and formation of the lowest state in the conduction band. It is confirmed that the measured data with SX-PES

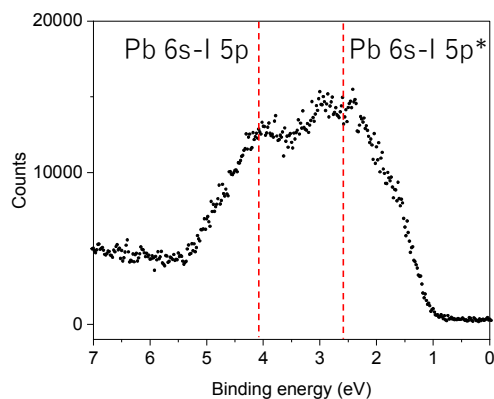


Figure 1 Measurement results of the valence band and Fermi level of the perovskite layer ($\text{CH}_3\text{NH}_3\text{PbI}_3$) with photon energy of 100 eV.

were in good agreement with the model predicted by the DFT calculations.

3.2 Estimation of the Fermi level

To deep understand the junction state, it is important to accurately determine the Fermi level of the semiconductor layer constituting a perovskite solar cells. In SX-PES measurement, the Fermi level corresponds to 0 eV from the rise of the Valence band edge. The difference between the valence band edge and the Fermi level of the produced perovskite polycrystalline thin film was 1.1 eV using SX-PES measurement. The band gap of perovskite polycrystalline thin film ($\text{CH}_3\text{NH}_3\text{PbI}_3$) of perovskite polycrystalline thin film was 1.59 eV from photoluminescence (PL) spectra (Figure 2), which showed to be an n-type semiconductor.

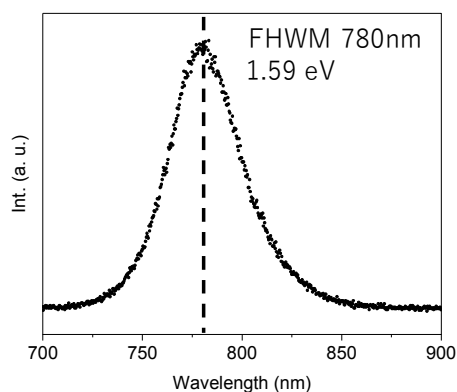


Figure 2 Measurement result of PL of the perovskite crystal layer. Excitation wavelength is 432 nm.

The measurement result of UPS with He 1α line (21.22 eV) of a perovskite layer is shown

in Figure 3. The results of SX-PES and UPS were in agreement. From the above results, it was confirmed that SX-PES can be evaluated up to the bonding state of the elements forming the valence band.

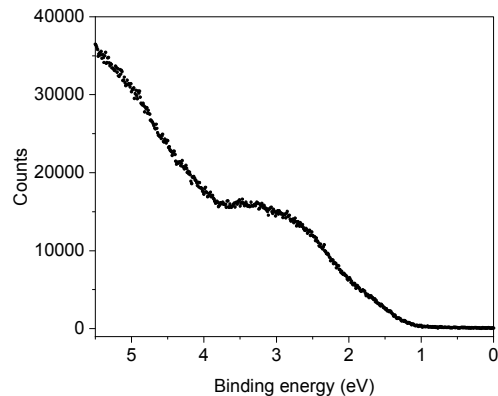


Figure 3 Measurement result of the Fermi level of Perovskite layer using UPS

Conclusions

We established a method to evaluate the formation state of the valence band of perovskite polycrystalline thin films using SX-PES measurement. The findings obtained this knowledge could be used in the material design of perovskite crystals.

References

- [1] A. Kojima, K. Teshima, Y. Shirai, T. Miyasaka, Organometal Halide Perovskites as Visible-Light Sensitizers for Photovoltaic Cells, *J. Am. Chem. Soc.* 131 (2009) 6050-6051.
- [2] E.H. Jung, N.J. Jeon, E.Y. Park, C.S. Moon, T.J. Shin, T.-Y. Yang, J.H. Noh, J. Seo, Efficient, stable and scalable perovskite solar cells using poly(3-hexylthiophene), *Nature*, 567, (2019) 511-515.
- [3] Q. Jiang, Y. Zhao, X. Zhang, X. Yang, Y. Chen, Z. Chu, Q. Ye, X. Li, Z. Yin, J. You, Surface passivation of perovskite film for efficient solar cells, *Nature Photonics*, 13, (2019), 460-466.
- [4] N. Shibayama, H. Kanda, T. W. Kim, H. Segawa, S. Ito, *APL Mater.* 7, (2019), 031117.
- [5] V. D'Innocenzo, G. Grancini, M. J. P. Alcocer, A. R. S. Kandada, S. D. Stranks, M. M. Lee, G. Lanzani, H. J. Snaith, A. Petrozza, *Nat. Commun.* 5, (2014) 3586.
- [6] K. Tanaka, T. Takahashi, T. Ban, T. Kondo, K. Uchida, N. Miura, *Solid State Commun.* 127, (2003) 619.

Evaluation of La doping effect in Sr₂IrO₄

R. Horie¹, S. Tsunoda², Y. Haruyama³, and J. Akimitsu¹

¹Research Institute for Interdisciplinary Science, Okayama University, ²Graduate School of natural science and technology, Okayama University, ³LASTI, University of Hyogo

Abstract

The 5*d*-electron system iridium oxide Sr₂IrO₄ is expected to become a high-temperature superconductor by doping carriers. We succeeded in synthesizing the highest electron-doped iridium oxide single crystal Sr_{1.88}La_{0.12}IrO₄ which has not been reported worldwide. However, a high-temperature superconductor has not been realized yet. In this material the effectiveness of the carrier doping by La doping is crucial. Hence, we examined the effect of La doping onto the valence of Ir and Sr by measuring core-level photoelectron spectroscopy using New-SUBARU synchrotron radiation (SR) facility. The narrowing effect of the core-level photoelectron peak has been found. These results are different from our original expectation of the chemical shifts of Ir 4*f* or Sr 3*d* core level. However, these results of the peak width narrowing may suggest some doping effect.

Introduction

The iridium oxide Sr₂IrO₄ of the 5*d* electron system has a layered perovskite type (K₂NiF₄ type) structure, which has the same crystal structure as La₂CuO₄ which is one of the mother substances of a copper oxide high-temperature superconductor. Its electronic structure is also similar. Hence it is expected that doping Sr₂IrO₄ with carriers may realize a high-temperature superconductor with multiple similarities such as magnetic structure, ARPES band structure and so on [1-3]. Sr₂IrO₄ is an antiferromagnetic insulator, and it is expected that a superconducting phase will appear over the antiferromagnetic metal phase with about 20% electron doping [2]. The author has succeeded in growing a single crystal with the highest La doping concentration in the world, La 0.2 (feed ratio) (Fig. 1). However, the superconductivity has not been realized yet. In this material the effectiveness of the carrier doping by La doping is crucial. Hence, we examined the effect of La doping onto the valence of Ir and Sr by measuring core-level photoelectron spectroscopy using New-SUBARU synchrotron radiation (SR) facility. In this study, using Sr₂IrO₄ and La-doped single crystals with various concentrations, we aimed to evaluate the change in the valence of Ir and Sr due to La-doping, and to obtain knowledge about the doping concentration and condition suitable to realize superconductivity.

Experiments and Results

The single crystal of Sr_{1.88}La_{0.12}IrO₄ was synthesized as shown in Fig. 1. X-ray Photoelectron Spectroscopy (XPS) experiments were performed at the beamline 07B end-station of the New-SUBARU synchrotron radiation (SR)



Fig.1 Single crystals of Sr_{1.88}La_{0.12}IrO₄.

facility, the University of Hyogo.

Figure 2 shows the setting of the sample on the sample holder. A clean surface of the sample was obtained by cleaving it in a preparation chamber at $\sim 2.0 \times 10^{-6}$ Pa by pushing the Cu rod attached on the sample as shown in Fig. 2. The vacuum of the main chamber at the time of XPS measurement was $\sim 1.2 \times 10^{-7}$ Pa.



Fig.2 Sample setting.

Figure 3 shows the La 4*d* XPS spectrum from Single crystal Sr_{1.88}La_{0.12}IrO₄. We could clearly obtain the doped La core-level peak. We could confirm that we can make holography experiment on La to elucidate the function of doped La atom.

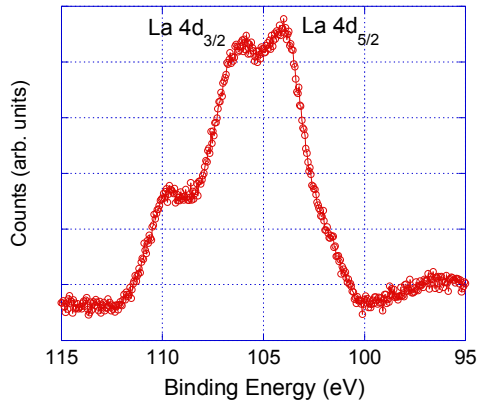


Fig.3 La 4d XPS spectrum from Single crystal $\text{Sr}_{1.88}\text{La}_{0.12}\text{IrO}_4$.

Figure 4 shows the Sr 3d XPS spectrum from single crystal with La doping ($\text{Sr}_{1.88}\text{La}_{0.12}\text{IrO}_4$) (red and blue) and without La doping (Sr_2IrO_4) (gray). The Sr 3d core peak from single crystal without La doping (Sr_2IrO_4) (gray) shows only one broad peak but those of La doping ($\text{Sr}_{1.88}\text{La}_{0.12}\text{IrO}_4$) (red and blue) show flat or even dip structure at the top of the peak. These two peak structures are the spin-orbit split of Sr 3d core. Hence, this spin-orbit split become more visible by La doping.

Figure 5 shows the Ir 4f XPS spectrum from single crystal with La doping ($\text{Sr}_{1.88}\text{La}_{0.12}\text{IrO}_4$)

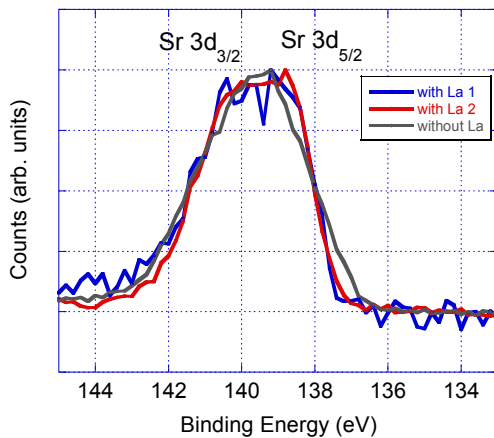


Fig. 4 Sr 3d XPS spectrum from single crystals with La doping ($\text{Sr}_{1.88}\text{La}_{0.12}\text{IrO}_4$) (red and blue) and without La doping (Sr_2IrO_4) (gray).

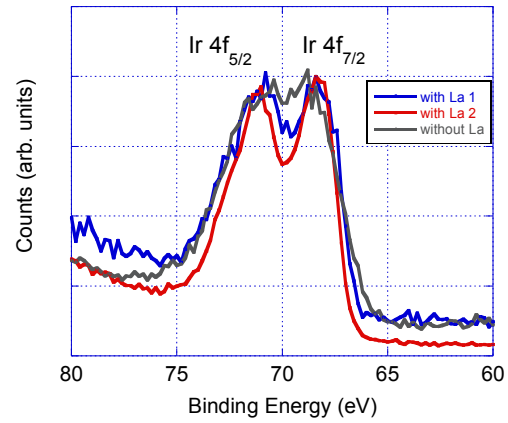


Fig. 5 Ir 4f XPS spectrum from single crystals with La doping ($\text{Sr}_{1.88}\text{La}_{0.12}\text{IrO}_4$) (red and blue) and without La doping (Sr_2IrO_4) (gray).

(red and blue) and without La doping (Sr_2IrO_4) (gray). The Ir 4f core peak from single crystal without La doping (Sr_2IrO_4) (gray) does not show clear two peaks again, but those of La doping ($\text{Sr}_{1.88}\text{La}_{0.12}\text{IrO}_4$) (red and blue) show clear two-peak structure which is the spin-orbit split of Ir 4f core. Hence, this spin-orbit split become more visible by La doping. These results are different from our original expectation of the chemical shifts of Ir 4f or Sr 3d core level. However, these results of the peak width narrowing may suggest some doping effect. Some theoretical works may be required to explain these narrowing effects.

The fact that we could observe the La 4d peaks is an important base of the photoelectron holography experiment in SPring-8, which realized as the proposal and execution of the experiment in 2018.

References

- [1] B. J. Kim, *et al.*, Science 323 (2009)1329.
- [2] H. Watanabe, *et al.*, Phys. Rev. Lett. 110 (2013) 027002.
- [3] K. Terashima, *et al.*, Phys. Rev. B **96** (2017) 041106(R).

Quasi-free-standing monolayer hexagonal boron nitride on Ni

Satoru Suzuki¹, Yuichi Haruyama¹, Masahito Niibe¹, Takashi Tokushima¹, Akinobu Yamaguchi¹, Yuichi Utsumi¹, Atsushi Ito², Ryo Kadowaki³, Akane Maruta³, and Tadashi Abukawa³

¹LASTI, Univ. of Hyogo, ²Graduate School of Engineering, University of Hyogo, ³Institute of Multidisciplinary Research for Advanced Materials, Tohoku University

Abstract

The electronic structure of monolayer hexagonal boron nitride grown on Ni by the diffusion and precipitation method was studied by x-ray absorption spectroscopy, emission spectroscopy, x-ray photoelectron spectroscopy and micro-ultraviolet photoemission spectroscopy. No indication of hybridization between h-BN π and Ni 3d orbitals was observed. That is, the monolayer h-BN was found to be in the quasi-free-standing state. These results are in striking contrast to those of previous studies in which h-BN was strongly bound to the Ni surface by the orbital hybridization. The absence of hybridization is attributed to absence of a Ni(111) surface in this study. The lattice-matched Ni(111) surface is considered to be essential to orbital hybridization between h-BN and Ni.

Introduction

Hexagonal boron nitride (h-BN) is a structural analogue of graphene. Now, monolayer h-BN is usually grown on transition metal substrates, such as Ni using chemical vapor deposition (CVD). In bulk h-BN, the neighboring layers are very weakly bound by the van der Waals interaction. However, previous studies using core level spectroscopies have shown that, in the CVD-grown h-BN/Ni system, there is strong hybridization between h-BN π and Ni 3d orbitals and that h-BN is chemisorbed on the Ni surface [1, 2]. Similarly, indications of strong hybridization have been also observed in h-BN/Ni systems grown by molecular beam epitaxy (MBE)[3] and by ion beam sputtering deposition methods [4]. Theoretical calculation even predicts that the large band gap of h-BN will disappear because of hybridization of the h-BN π state with Ni 3d at the Fermi level and that h-BN on Ni is metallic [5].

The diffusion and precipitation method is another way to grow atomically thin h-BN films [6-9]. This method utilizes only a solid phase reaction. Thus, it is much safer than the CVD, which uses flammable and toxic gases as source and carrier gases. In this study, monolayer h-BN was grown on Ni by the diffusion and precipitation method, and the bonding character between the monolayer h-BN and Ni, which has not yet been addressed, was studied using x-ray absorption spectroscopy (XAS), x-ray emission spectroscopy (XES), x-ray photoelectron spectroscopy (XPS), and photoemission electron microscopy (PEEM) [10].

Experiments and Results

Submonolayer h-BN films were grown on Ni foil using the diffusion and precipitation method, based on our previous studies [6-9]. Briefly, a ~100-nm-thick amorphous boron nitride (a-BN) film was deposited on a Ni foil (Nilaco Co., thickness: 25 μm) using the radio frequency magnetron sputtering method. The a-BN/Ni samples were heated either in the endstation of the beamline BL7B in the NewSUBARU synchrotron radiation facility or in a stand-alone PEEM apparatus. The heating temperature and time were about 900 $^{\circ}\text{C}$ and 30 minutes, respectively. During the heating, a fraction of B and N atoms of the a-BN film diffused through the Ni foil and formed h-BN on the opposite face of the Ni foil. The samples had been kept in an ultra-high vacuum until XAS, XPS and PEEM measurements were completed, without otherwise mentioning.

XAS and XES measurements were performed at the beamline BL7B and BL9A at NewSUBARU, respectively. To our knowledge, this is the first observation of takeoff angle dependence of XES from monolayer h-BN. In-situ PEEM observation was performed in a PEEM apparatus (IS-PEEM, FOCUS GmbH) equipped with a micro-analyzer [29, 30]. Local work function measurements by selected-area ultraviolet photoemission spectroscopy (micro-UPS) were also performed using the same apparatus. A field emission scanning electron microscope (SEM) (JEOL, JSM-7001F) was used for ex-situ electron backscatter diffraction (EBSD) measurements and SEM observation.

As shown in Fig. 1(a), bulk h-BN (unoriented

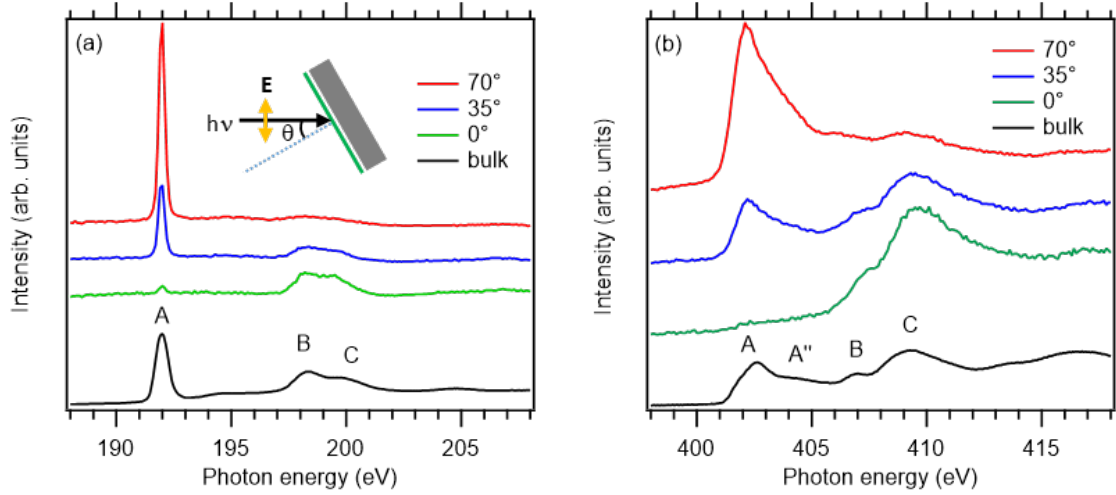


Fig. 1. Polarized (a) B-K and (b) N-K XAS of monolayer h-BN/Ni and bulk h-BN.

powder sample) shows a sharp and strong exciton peak at about 192 eV in the B-K absorption spectrum, as denoted by A. This peak is caused by the transition from B 1s to π^* ($2p_z$). The transition to σ^* ($2p_x, 2p_y$) components is observed at around 198 and 200 eV, as denoted by B and C. In the N-K spectrum, the transition from N 1s to π^* orbital is observed at about 402 eV. The small hump is observed at about 404 eV as denoted by A'. Here, we use these denotations in accordance with ref. 1. The transitions to σ^* orbitals are observed at around 407 and 409 eV, as shown in Fig. 1(b). The excitonic effect is much less prominent in the N-K spectrum, meaning that the unoccupied π^* state has larger B $2p_z$ (smaller N $2p_z$) character. This can be basically explained in terms of the higher electronegativity of N than B; that is, a certain degree of ionic character of B-N bonds.

In previous XAS studies of h-BN/Ni systems, the B-K spectra have been found to be considerably different from those of bulk h-BN. At both lower and higher energies of the original exciton peak, additional broad spectral features appear (often denoted by A' and A'') [1-3]. Alternatively, the sharp exciton peak A becomes broader and less intense. In the N-K spectrum, A' peak also appears at about 398 eV, at the low energy side of the threshold [1-3]. The A peak becomes less intense and the A'' peak becomes much more intense. Both the newly appeared features A' and A'' have been shown to have π^* symmetry [1, 3]. Based on these results, it has been concluded that there is a large degree of hybridization between h-BN π (π^*) and Ni 3d orbitals.

Figure 1(a) also shows the polarized B-K spectrum of h-BN/Ni grown by the diffusion and precipitation method. From SEM observation, the coverage of monolayer h-BN was evaluated to be about 0.8. For a planar h-BN sheet, absorption intensities of π^* and σ^* symmetries are expected to

be simply proportional to $\sin^2\theta$ and $\cos^2\theta$, respectively (θ : incidence angle). The large polarization dependence indicates that the h-BN atomic sheet is oriented parallel to the Ni surface, as reasonably expected. The incidence angle of 35° almost corresponds to the magic angle at which an unpolarized spectrum is obtained. In good contrast to previous studies, the spectrum of h-BN/Ni is very similar to that of bulk h-BN and the peaks A' and A'' do not appear. Similarly, the N-K spectra of h-BN/Ni is very similar to that of bulk h-BN and no additional features are observed. These results indicate that the monolayer h-BN grown by the diffusion and precipitation method on the Ni foil almost sustains the original electronic structure of h-BN.

B-K and N-K XES of bulk h-BN are shown in Fig. 2. Here, in the bulk h-BN sample, c axes of microcrystals are highly oriented by compressing. In this case, considering both s- and p-polarized light emission, intensities of π and σ symmetries are expected to be proportional to $\cos^2\theta$ and $(1+\sin^2\theta)/2$, respectively. In contrast to XAS, a prominent π peak is observed at about 394 eV in N-K XES of bulk h-BN and is not observed in B-K XES because the π electron more largely occupies the N $2p_z$ than the B $2p_z$ orbital because of the specific ionic character of B-N bonding. The other peaks in the N-K spectrum are attributed to σ orbitals. In the B-K spectrum, both π and σ spectra are broad and have considerable overlap. In a previous study on CVD-grown h-BN/Ni [2], a gap state due to h-BN π -Ni 3d hybridization was observed in the bandgap region (188-190 eV) in B-K XES. Changes observed in N-K XES were much more drastic. The π peak completely disappeared. Instead, the spectral intensity was mostly transferred to the gap state (396-398 eV).

XES of h-BN/Ni obtained at three incidence (take off) angles are also shown in Fig. 2. As shown in Fig.

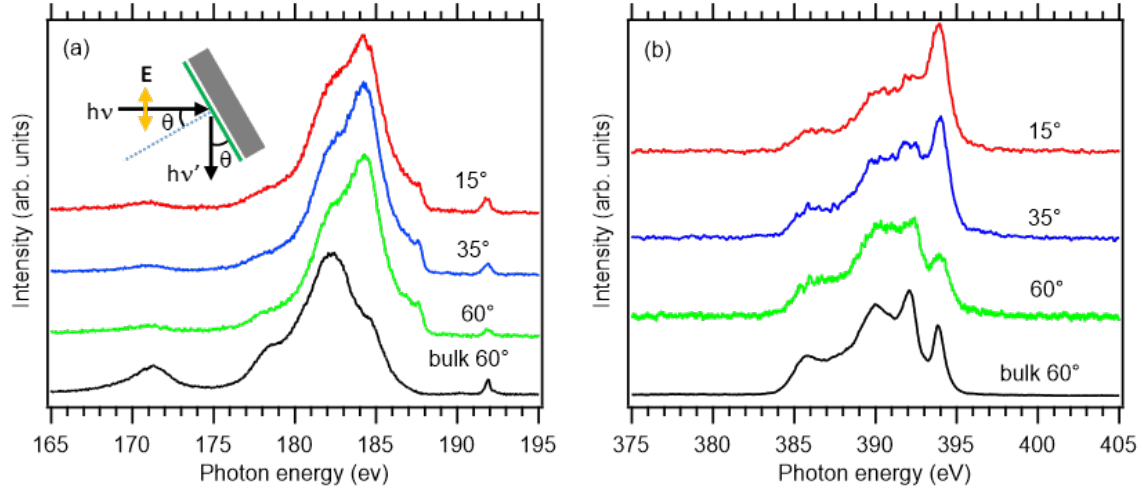


Fig. 2. (a) B-K and (b) N-K XES of monolayer h-BN/Ni and bulk h-BN.

2(a), B-K XES of h-BN/Ni largely differs from bulk h-BN and only a weak takeoff angle dependence is observed, strongly suggesting that a spectrum of some form of B other than h-BN is superposed. However, with the exception of a small amount of excess B and its oxide observed in XPS (not shown), no such considerable amount of another form of B has been observed in surface sensitive techniques, such as XAS (Fig. 1), XPS, micro-Auger spectroscopy, or in cross-sectional transmission electron microscope observation [6-8]. We think that the additional spectrum comes from B atoms that had diffused in the Ni foil. As mentioned in our previous report [6], the solubility of B in Ni reaches 0.3 at.% at 1085°C, although the solubility of N is negligibly small even at high temperatures. The B atoms in Ni would remain inside when the sample was quenched after heating. Considering that XES is bulk-sensitive, it is not surprising that the number of B atoms in the probing depth is comparable to or larger than that of 0.8 ML of h-BN at the surface. Now, we would like to focus on the bandgap region. No gap state is observed in the h-BN/Ni sample, suggesting the absence of h-BN π and Ni 3d hybridization. N-K XES of the h-BN/Ni sample is similar to that of h-BN, as shown in Fig. 2(b). The incidence angle dependences of the π and σ peaks are, again, consistent with the planar h-BN sheet. As clearly seen in the figure, the π peak still exists and the gap state does not appear.

These XAS and XES results are consistent with each other and indicate that there is little hybridization between h-BN π and Ni 3d and that h-BN is physisorbed on the Ni surface. In other words, the monolayer h-BN is in a quasi-free-standing state on Ni, in striking contrast to the findings in previous studies [1-4] in which h-BN was found to be strongly bound to Ni by the hybridization.

The work function of CVD-grown h-BN on Ni(111) (work function: 5.3 eV [1]) was reported to

be 3.6 eV [1]. That is, h-BN growth decreases the work function by 1.7 eV. The large work function decrease strongly suggests electron transfer from h-BN to Ni and dipole formation at the h-BN/Ni interface. Figure 3(a) shows a PEEM image of h-BN/Ni. Bare Ni surface and h-BN domains are observed darkly and brightly, respectively. The contrast is mainly considered to be due to work function change induced by h-BN formation. The enhanced photoemission from the h-BN-covered surfaces indicates that h-BN formation also decreases the work function in our case. However, the work function decrease is less prominent than in previous studies. Figure 5(b) shows secondary electron spectra obtained from several points. Curves A and B were obtained from bare Ni surfaces, and curves C, D, and E were from h-BN/Ni. From the cutoff energies of curves A and B, the work functions of the Ni surfaces are evaluated to be about 5.0 and 4.8 eV. The difference is considered to be caused by the difference in orientation of Ni grains due to the polycrystalline structure of the Ni foil. The work functions of h-BN/Ni are evaluated to be 4.6, 4.5, and 4.0 eV from curves C, D, and E. These values are considerably larger than that in a previous report (3.6 eV). The work function decreases are within a range of 0.2 to 1.0 eV, which is also considerably lower than those in previous studies (1.7 eV). The relatively large work functions and small work function decreases suggest the absence of a large dipole at the h-BN/Ni interface and thus, the absence of large charge transfer between h-BN and Ni.

Here, we discuss the possible reason for this. In all the previous studies, single-crystalline Ni was used, and monolayer h-BN films were grown on Ni(111) surfaces [1-4]. However, the Ni foil used in this study had a polycrystalline structure with a typical grain size of 100 μm . The z -direction EBSD map reveals that there is no (111) face after the h-BN

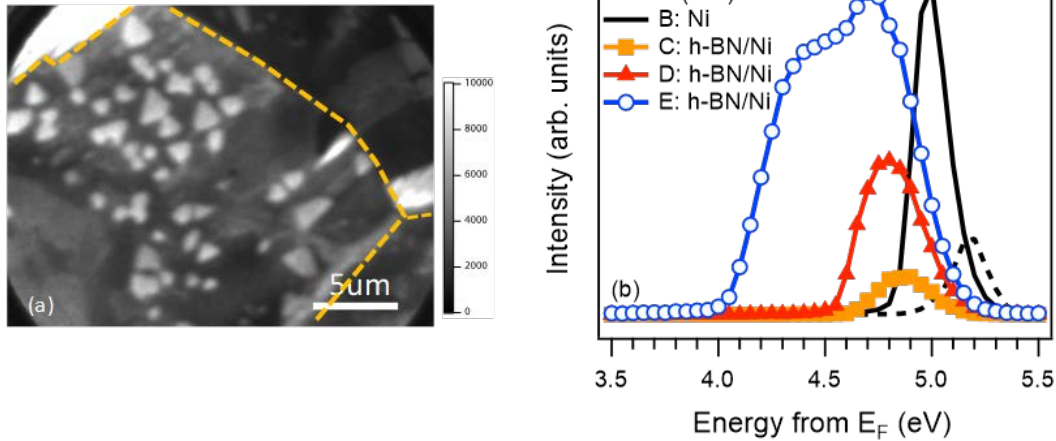


Fig. 3. (a) PEEM image of submonolayer h-BN/Ni. (b) Secondary electron spectra obtained from bare Ni surfaces (A and B) and h-BN/Ni (C, D, and E). In (a), the grain boundaries are denoted by the dashed lines.

formation. The Ni(111) surface has a six-fold symmetry. Its lattice constant is 0.249 nm, which is close to that of h-BN (0.250 nm). The translational symmetry may be essentially important for the chemisorption properties of h-BN/Ni(111). In this study, the symmetry and lattice constant of the Ni surface do not match those of h-BN at all. We think that the lack of hybridization is due to the absence of the Ni(111) surface in this study. That is, the

hybridization between h-BN π and Ni 3d is characteristic of the Ni(111) surface, which matches atomic structure of h-BN. Our results suggest that it is possible to grow quasi-free-standing h-BN on Ni by growth techniques other than the diffusion and precipitation method by using a non-(111) Ni surface.

References

- [1] A. B. Preobrajenski et al., *Surf. Sci.* **582** (2005) 21.
- [2] A. B. Preobrajenski et al., *Phys. Rev. B* **77** (2008) 085421.
- [3] D. Usachov et al., *Phys. Rev. B* **82** (2010) 075415.
- [4] A. A. Tonkikh, *Sci. Rep.* **6** (2016) 23547.
- [5] A. Miyashita et al., *Phys. Rev. B* **97** (2018) 195405.
- [6] S. Suzuki et al., *J. Phys. D: Applied Physics* **45** (2012) 385304.
- [7] S. Suzuki et al., *J. Vac. Sci. Technol. B.* **31** (2013) 041804.
- [8] S. Suzuki et al., *Jpn. J. Appl. Phys.* **56** (2017) 06GE06.
- [9] S. Suzuki et al., *Jpn. J. Appl. Phys.* **58** (2019) SIIB15.
- [10] S. Suzuki et al., *Mater. Res. Express* **6** (2019) 016301.

Growth and Decomposition of Hexagonal Boron Nitride in the Diffusion and Precipitation Method Studied by X-ray Photoelectron Spectroscopy

Suzuki and Yuichi Haruyama,
LASTI, University of Hyogo

Abstract

Submonolayer h-BN was grown on Ni foil in ultra-high vacuum by the diffusion and precipitation method and the growth and decomposition processes were studied by x-ray photoelectron spectroscopy. Formation of h-BN started at 600 °C. All through the process, the surface was always slightly B-rich, which is consistent with the fact that B which is soluble in Ni at a high temperature can diffuse in Ni by the conventional bulk diffusion and insoluble N cannot. Moreover, both formation and decomposition of h-BN were found to be competing at elevated temperatures possibly depending on provision of N atoms to the surface. On the Ni surface, decomposition of h-BN was observed at a relatively low temperature of 800 °C.

Introduction

The large chemical stability of hexagonal boron nitride (h-BN) is one of very important properties for various applications. The thermal decomposition temperature of bulk h-BN has been reported to be extremely high (2127-2327 °C).¹⁾ Recently, chemical vapor deposition (CVD) is commonly used for growth of large-area and atomically thin h-BN. CVD growth is normally performed under gas flow with relatively high or ambient pressure. Therefore, direct characterization of the growth process by electron spectroscopy is very difficult. In fact, there have been few reports on spectroscopic observation of the growth process of h-BN CVD.

The diffusion and precipitation method is an alternative way to grow atomically thin h-BN film.²⁻⁴⁾ This method utilizes only solid phase reaction of a metal (Ni was used in this study) substrate and solid source (a-BN). B and N atoms diffuse from the bottom surface to the top surface of the metal foil at an elevated temperature and form h-BN on the top surface. Therefore, h-BN can be grown in an ultra-high vacuum (UHV). Thus, this method is very suitable for analysis of growth process in a UHV environment. In the diffusion and precipitation method, it is considered that feeding mechanism of B and N atoms to the surface is different. Although B is known to be slightly soluble in Ni at high temperature, the solubility of N is negligibly small even at high temperature. Grain boundary diffusion (in Ni) and surface migration (on top surface) were considered to be responsible for feeding N atoms from our previous studies. In this report, we studied the growth process of monolayer h-BN in the diffusion and precipitation method by using x-ray photoelectron spectroscopy (XPS).⁵⁾

Experiments and Results

A submonolayer h-BN film was grown on Ni foil using the diffusion and precipitation method, based on our previous studies.²⁻⁴⁾ Briefly, an amorphous boron nitride (a-BN) film (thickness: about 100 nm) was deposited on a Ni foil (Nilaco., thickness: 25 μm) using radio frequency magnetron sputtering in Ar/N₂ atmosphere (Ar/N₂ flow rate: 1:1). The a-BN/Ni sample was loaded in the sample preparation chamber connected to the XPS analysis chamber at BL7B in NewSUBARU. In the preparation chamber,

Table 1. Sequential heating processes.

Process no.	Heating temperature and time
0	Before heating
1	600 °C, 10 min
2	800 °C, 10 min
3	800 °C, 10 min
4	850 °C, 10 min
5	850 °C, 10 min
6	850 °C, 10 min
7	850 °C, 10 min
8	850 °C, 10 min
9	900 °C, 10 min
10	900 °C, 20 min
11	950 °C, 10 min
12	1000 °C, 10 min

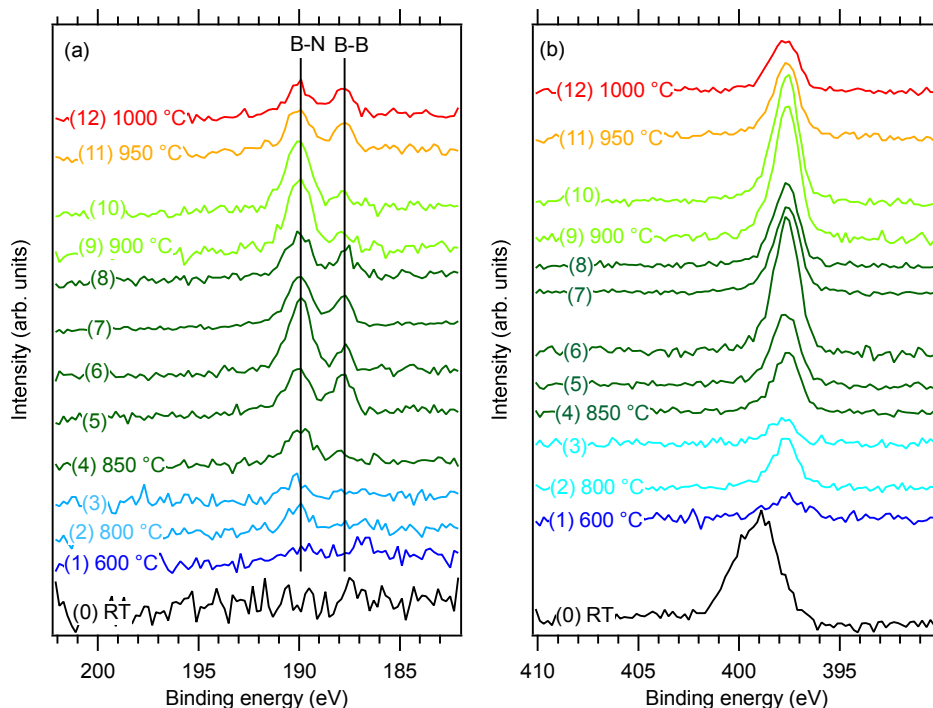


Fig 1. (a) B 1s and (b) N 1s XPS obtained at each process. The numbers in parenthesis correspond to the process numbers in Table 1.

the sample was heated at a certain temperature in a range of 600 to 1000 °C by electron bombardment to the a-BN-deposited face. Then, the sample was transferred to the analysis chamber and XPS of undeposited face was measured at room temperature. Unmonochromatized Al K α line (1486.6 eV) was used for XPS measurements. Heating and XPS measurements were repeated. Heating temperature and time at each process were summarized in Table

1. In this study, the maximum h-BN coverage was observed at process 6 and estimated to be about 0.5 from B 1s (N 1s)/Ni 2p XPS intensity ratio.

B 1s and N 1s XPS obtained at each process are shown in Fig. 1. The N 1s signal centered at 399 eV observed before heating (process 0) is not due to h-BN formation, but surface nitridation during the a-BN deposition, as mentioned above. In fact, the N 1s binding energy differs from that of h-BN (397.6 eV),

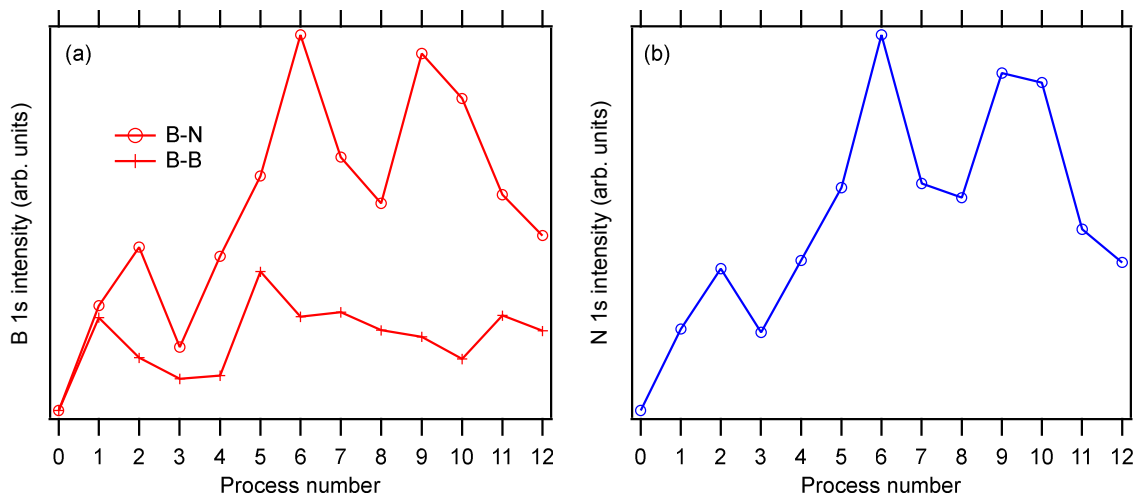


Fig 2. (a) B 1s and (b) N 1s integrated XPS intensity at each process. In (a), B 1s intensities from h-BN and elemental B are shown, respectively. In (b), the initial N intensity observed at process 0 was excluded in order to focus on N 1s intensity from h-BN.

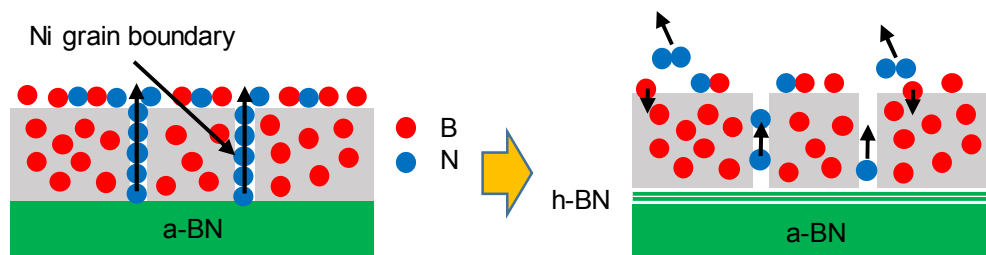


Fig 3. Schematic model for formation and decomposition of h-BN. When provision of N atoms through Ni grain boundary is large, formation of h-BN is dominant (left). When provision of N atoms is small, decomposition becomes dominant (right).

and no B 1s signal is observed. The spectra shows that h-BN formation slightly started at 600 °C (process 1). In the B 1s spectrum, h-BN formation is still barely visible. However, in the N 1s spectrum, a small peak is observed at about 397.6 eV, which corresponds to N 1s binding energy of h-BN. Instead, the peak initially observed at 399 eV disappeared. After annealing at 800 °C and higher temperatures (process 2-12), h-BN formation is also clearly visible in B 1s spectra. However, the B 1s spectra split into two peaks. The peak at 190.0 and 188.0 eV are assigned to h-BN and elemental B, respectively. The results indicate that feeding of B and N atoms are not balanced, but the surfaces are B-rich. The elemental B component is likely to appear on the surface during cooling, because B is slightly soluble in Ni at a high temperature.⁶⁾ The B-rich surfaces are consistent with our previous conclusion that h-BN formation is restricted by provision of N atoms to the surface.²⁻⁴⁾ The elemental B is quickly oxidized when the sample is exposed to air, as shown in our previous report.⁷⁾

As can be seen in Fig. 1, the B 1s and N 1s intensity evolution is not monotonic. Figure 2 shows B 1s and N 1s intensity evolutions obtained from Fig. 1. The B 1s (B-N) and N 1s intensity evolutions are reasonably similar to each other due to h-BN formation. Interestingly, heating sometimes caused B 1s and N 1s intensity decreases. Heating at constant temperatures of 800 (processes 2, 3), 850 (4-8), 900 °C (9, 10), the B 1s and N 1s intensities increased at first, and then, they declined. In this heating process, further temperature increase merely decreased the coverage of h-BN (11, 12). These results indicate that not only formation of h-BN but also decomposition occurs at these temperatures. The decomposition was even observed at a relatively low temperature of 800 °C (process 3).

Recently, we could directly observe B atoms solved in Ni foil after h-BN formation by using B-K x-ray emission spectroscopy.⁷⁾ This is consistent with the fact that B is slightly soluble in Ni at a high

temperature. Thus, B atoms can reach the top surface by conventional bulk diffusion. On the other hand, our previous study strongly suggest that provision of N atoms is caused by grain boundary diffusion and surface migration.²⁻⁴⁾ Figure 3 shows a schematic model for explaining the XPS intensity evolutions observed in this study. Heating causes recrystallization of Ni. Then, N atoms in the a-BN film can reach the top surface through the grain boundary. N atoms migrate on the top surface and form h-BN by bonding to B atoms. This study shows that formation and decomposition of h-BN are competing at the elevated temperatures. At first, the provision of N atoms is relatively large and formation of h-BN is dominant. However, repeated heating (processes 3, 7, 8, 10-12) results in decreased provision of N atoms. Then, decomposition becomes dominant. We think that h-BN layers formed at the a-BN/Ni interface²⁾ is highly responsible for the decrease of N atom provision. The h-BN layers would act as a barrier for N atoms in the a-BN film to diffuse into the Ni foil. We did not observe any N 1s signal other than N-B bond in XPS except for process 0. Thus, insoluble N atoms created by decomposition are released to vacuum possibly by forming inert N₂ molecules. B atoms created by decomposition can either melt into Ni or remain on the surface.

Decomposition of h-BN was observed at a relatively low temperature of 800 °C. This temperature is much lower than the decomposition temperature of bulk h-BN (2127-2327 °C).¹⁾ A catalytic effect of the Ni surface is also considered to be important for decomposition of h-BN at such a low temperature.

References

- [1] S. Gleiman et al., *J. Mater. Sci.* **37** (2002) 3429.
- [2] S. Suzuki et al., *J. Phys. D: Applied Physics* **45** (2012) 385304.

- [3] S. Suzuki et al., J. Vac. Sci. Technol. B. **31** (2013) 041804.
- [4] S. Suzuki et al., Jpn. J. Appl. Phys. **56** (2017) 06GE06.
- [5] S. Suzuki et al., Jpn. J. Appl. Phys. **58** (2019) SIIB15.
- [6] P. C. Yang et al., J. Electric. Mater. **34** (2005) 1558.
- [7] S. Suzuki et al., Mater. Res Express **6** (2019) 016301.

Analysis of chemical reactions at the Au-thin-film/Si interface by soft x-ray photoelectron spectroscopy under steam ambient

Tomoki Yamamoto¹, Satoshi Toyoda², Satoru Suzuki¹, Hirosuke Sumida³,
Susumu Mineoi³, Kazushi Yokoyama¹, Akitaka Yoshigoe⁴, and Shizuka Nishi⁴
¹Univ. of Hyogo, ²Tohoku Univ, ³Mazda, ⁴JAEA

Abstract

We focused on the alloying reaction at the contact interface of Au and Si, and traced the reaction process by soft x-ray photoelectron spectroscopy in H₂O atmosphere with heating the Au/Si sample. In this study, it is suggested that H₂O atmosphere promotes Au/Si alloying even at a very low partial pressure of 1×10^{-6} Pa.

Introduction

To improve the function of semiconductor devices such as diodes and transistors, many studies have been conducted on the reaction control at the contact interface between semiconductor and metal. Among them, it is known that an interesting phenomenon occurs at the interface between semiconducting Si and metallic Au. Although the eutectic point of bulk Si and Au is 370 °C, when Au thin film is deposited on the Si substrate, Si atoms diffuse into Au at a temperature lower than 370 °C and SiO₂ is formed on the Au surface. Even at room temperature, the diffusion of Si can be observed if Au/Si sample is left for about two weeks [1]. From these phenomena, Au/Si has been studied by various surface analysis methods as an important alloy system for interface control of semiconductor devices. We are conducting research with the aim of establishing a technology for quantitatively analyzing chemical reactions that occur at material interfaces from photoelectron spectroscopy data, using this Au/Si interface as a model system. Here, we report the influence of H₂O atmosphere on the reaction of Au/Si system [2].

Experiments and Results

The experiments were carried out at SPring-8 BL23SU by using atmosphere controlled soft x-ray photoelectron spectrometer (surface chemistry experimental station). A water exposure device was added to the analysis tank to introduce H₂O into the analysis chamber. The alloying temperature of Au/Si was observed by the shift of the binding energy of the Au4f_{5/2} and 4f_{7/2} levels accompanying alloying, as shown in Figure 1.

Annealing in Steam: Au 4f core-level

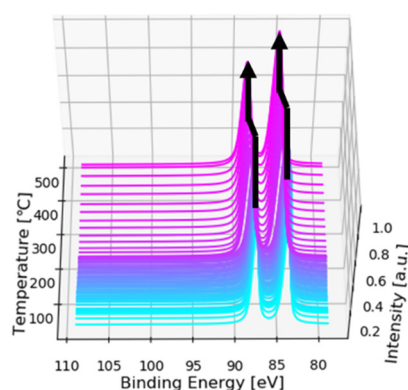


Fig.1. Au 4f photoelectron spectra obtained at various temperatures. The positions of peak tops are determined by fitting Au4f_{5/2} and Au4f_{7/2} respectively with Pseudo Voigt function.

A sample with an Au film deposited up to a thickness of about 60 nm on a Si substrate was subjected to photoelectron spectroscopy measurement with raising the temperature of the sample.

Figure 2 shows the temperature dependence of the Au4f binding energy of Au/Si sample (Au/Si (VAC)) and Au/mica sample (Au / mica (VAC)) in ultra-high vacuum (1×10^{-8} Pa), and Au/Si sample (Au/Si (H₂O)) under H₂O atmosphere (1.0×10^{-6} Pa).

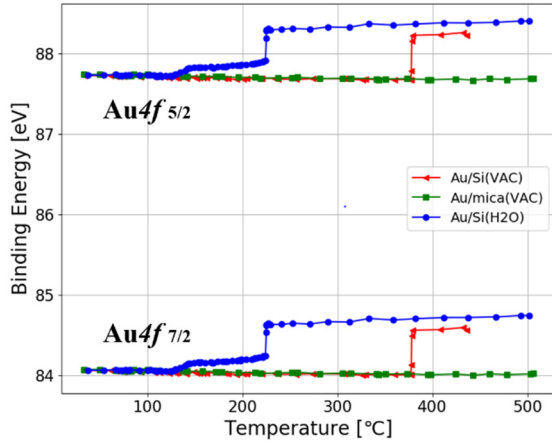


Fig. 2 Temperature dependence of Au4f binding energy of Au/mica and Au/Si samples

In the sample where Au was deposited on mica, alloying was not observed even when heated to 500 °C. However, when the Au/Si sample was measured in H₂O atmosphere, the transition temperature was lowered to about 225 °C. When measured even under an O₂ atmosphere (1×10^{-4} Pa) before, the transition temperature was lowered to the same extent [3], but this time it is under a pressure about 100 times lower. Thus, it is considered that the H₂O atmosphere has a function to promote the alloying of Au/Si even at a very low partial pressure of 1×10^{-6} Pa.

References

- [1] A. Hiraki et al., J. Japan Inst. Met. **15**, 665 (1976)
- [2] T. Yamamoto et al., 80th Japanese Society of Applied Physics Autumn Meeting 2019, September 2019, Sapporo, 20a-E318-5.
- [3] S. Toyoda et al., 79th Japanese Society of Applied Physics Spring Meeting 2018, September 2018, Nagoya, 18p-212B-7.

Soft X-ray absorption and Emission Spectroscopy of Monolayer and Few-layer Graphene Sheet

Masahito Niibe¹, Satoru Suzuki¹, and Shin-ichi Honda².

¹LASTI, University of Hyogo, ²Graduate School of Eng., University of Hyogo

Abstract

We measured soft X-ray absorption (XAS) and emission (XES) spectra in C K-edge region of monolayer and few-layer graphene including incident/take-off angle dependence, in the BL-09A at the NewSUBARU SR Facility. Spectra similar to HOPG, which is a standard substance, were obtained for both the XAS and the XES. However, the incident/take-off angle dependence of π/σ ratio was smaller than that of HOPG. The band structure of monolayer graphene constructed using the results of XAS and XES spectra has the characteristics of a semimetal.

Introduction

From pioneering experiments on two-dimensional (2D) graphene by A. Geim and K. Novoselov [1], graphene is noted as a Van der Waals 2D layered material, and much research has been performed from both basic and applied aspects. In particular, monolayer graphene has a unique band structure called Dirac cone and has a very large electron mobility [2], and thus is attracting attention as a next-generation semiconductor device material. From these backgrounds, information on the electronic state of monolayer graphene is very important in the nano-carbon field.

As an effective means for directly observing the band structure of a solid state substance, there is a method using soft X-ray absorption spectroscopy (XAS) [3] and emission spectroscopy (XES) [4] in combination. The spectrum of XAS reflects the density of states of the conduction band of the solid, while XES can obtain information of the valence band. An excellent report has been made by Pacile et al. on C-K absorption spectra of graphene sheets from a monolayer to five or more layers [5]. Although the XES spectra of monolayer graphene are reported by Zhang et al. [6] and Ilkov et al. [7], their energy resolution is not sufficient. And also, the take-off angle dependence of the soft X-ray emission has not been reported.

We have developed a soft X-ray emission spectrometer that can measure the K-emission of light elements such as boron (B), carbon (C), nitrogen (N) and oxygen (O) with high energy resolution in the NewSUBARU SR Facility at the University of Hyogo [8]. As a result, we have reported on the large take-off angle dependence of the XES spectra of highly oriented pyrolytic graphite (HOPG) [9]. We have also reported the B K-emission spectrum of a trace (0.32%) B-doped HOPG sample [10]. Therefore, the spectrometer is suitable for emission spectroscopy of light element films of monoatomic layer. We have prepared nano-

carbon materials of monolayer and few-layer and tried to measure the soft X-ray absorption and emission spectra at the C K-edge region.

Experiment

The measured samples are a graphene sheet in which a monolayer graphene (Graphene Platform Corp.) and a few-layer of graphene (National Taiwan University of Technology and Science) grown on Cu substrates. The monolayer graphene sample was transferred onto a SiO₂ (285nm)/Si substrate by using commonly used PMMA method [11]. With regard to few-layer graphene, graphene grown by CVD method on a Cu substrate was exfoliated by etching the underlying Cu in FeCl₃ solution, and it was fixed on a Si substrate by skimming it. The number of layers of few-layer graphene is estimated to be 2 to 3 from the 2D/G ratio (= 0.816) of the Raman spectrum.

The soft X-ray absorption and emission spectra were measured at the “Long Undulator” beamline BL-09A at the NewSUBARU SR facility [12]. Absorption spectroscopy was based on the total electron yield (TEY) method using sample current measurement. The emission spectra were measured with the excitation energy of 310 eV, which is considered to be non-resonant condition at the C K-edge. The XES spectrometer is placed to receive an emitted X-ray beam in a direction rotated 90° from the incident beam in the horizontal plane. The incident light is linearly polarized, where the electric vector is in the horizontal direction. In this study, the incident/take-off angle dependence of the spectrum was also measured by rotating the sample manipulator around the vertical axis. Here, the incident angle in the XAS measurement is represented as an angle measured from the sample surface normal, and the take-off angle in the XES

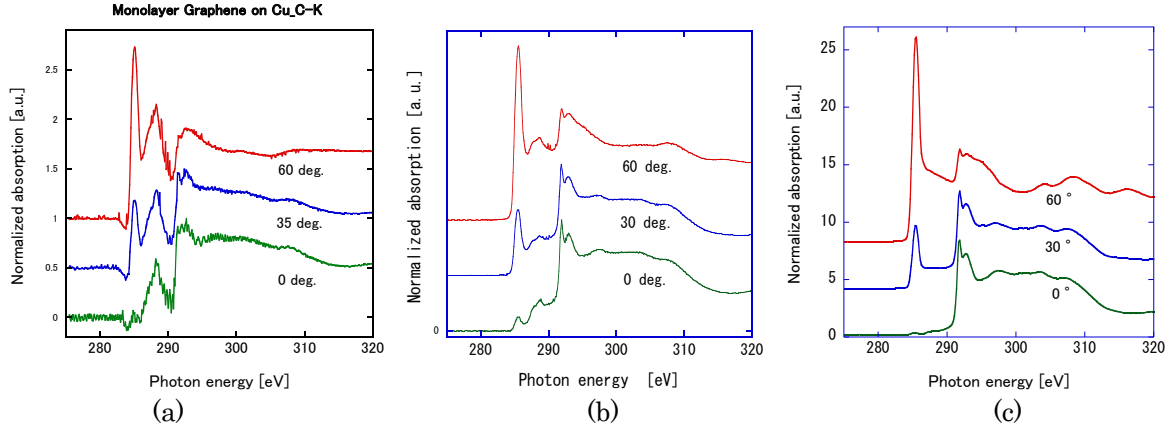


Fig 1. Incident angle dependence of C K-edge absorption spectra of (a): monolayer graphene, (b): few-layer graphene, and (c): HOPG as reference.

measurement is represented as an angle measured from the sample surface.

Results

Figure 1 shows the incident angle dependence of C K-edge absorption spectra of (a): monolayer graphene, (b): few-layer graphene, and (c): HOPG as reference [13]. For the C-K absorption spectrum of monolayer and few-layer graphene samples, spectra similar to HOPG was obtained. In particular, the π^* peak around 285.4 eV has a very small intensity at an incident angle of 0 deg., and significantly increases with the increase of the incident angle. In the spectra of monolayer and few-layer graphene, multiple peaks not observed in HOPG were observed in the region of 287 to 290 eV. These are considered to be peaks derived from an airborne contamination carbon-oxide. Monolayer graphene is thought to be relatively stable and oxidation does not proceed even in the atmosphere. Therefore, the oxide observed here is considered to be derived from the contaminant deposited on the graphene during the sample storage in air [14].

Figure 2. shows the take-off angle dependence of

C K-edge emission spectra of (a): monolayer graphene, (b): few-layer graphene, and (c): HOPG as reference [9]. Although, soft X-ray emission from monolayer graphene is considered to be very weak, one of these spectra could be acquired at an exposure time of 20 to 30 min.

The emission intensities change depending on the take-off angle, but when normalized so that the rising part of 277 eV or less (lower energy side foot of the peak) become equal, it can be roughly divided into two components depending on or independent of the take-off angle. They are component with less angle dependence of about 280 eV or less and the angle dependent peak at 282 eV. These take-off angle dependences are similar to that of HOPG previously reported by us [9], and it can be identified that the peak of 280 eV or less is derived from the σ orbital and the peak at 282 eV is derived from the π orbital of graphene/graphite honeycomb network.

The incident angle dependence of the ratio of the π peak to the σ peak, ie, the π/σ ratio, appears to have a smaller rate of change than that of HPOG in both the XAS and XES spectra. As one of the reasons, it

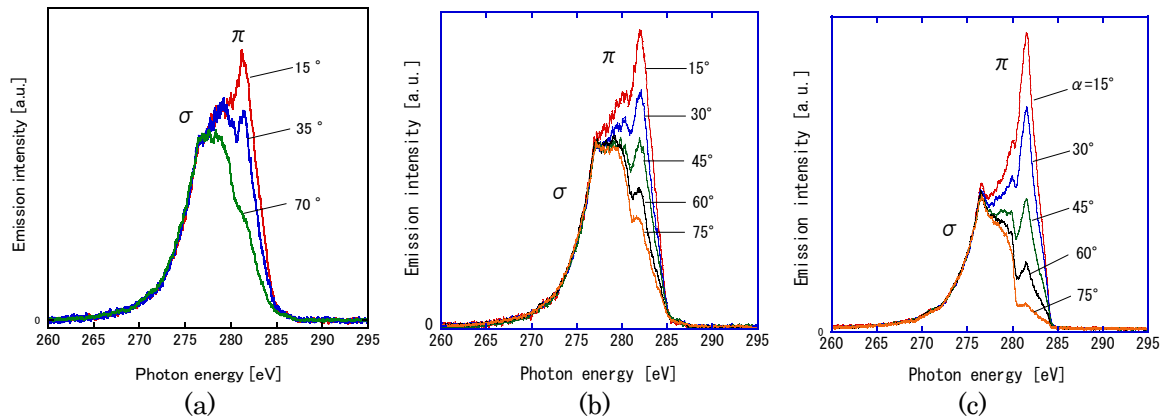


Fig 2. Take-off angle dependence of C K-edge emission spectra of (a): monolayer graphene, (b): few-layer graphene, and (c): HOPG as reference.

has been reported that when a monolayer / few-layer graphene was transferred to a SiO₂ / Si substrate, corrugation or wrinkles in the film was generated [15].

Figure 3 shows the band structure of monolayer graphene obtained by combining the results of XAS and XES measurements. As can be seen from the figure in the monolayer graphene, the valence band and the conduction band are in contact at an energy of about 284 eV measured from C1s level, and have a semi-metallic property.

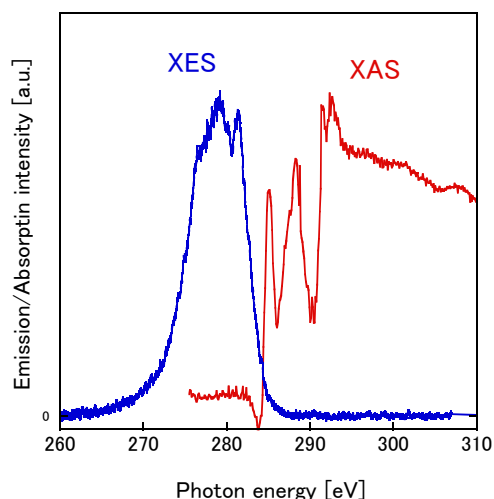


Fig 3. Combining results of the XES and XAS spectra of monolayer graphene (band structure).

As summary, we were able to measure for the first time soft X-ray absorption and emission spectra at C K-edge of monolayer and few-layer graphene, including dependence of incident/take-off angles. The shapes of the absorption and emission spectra

are similar to that of the standard sample of HOPG. However, the incident/take-off angle dependency of π/σ ratio was smaller compared to HOPG. An oxide peak was observed in the spectrum of monolayer and few-layer graphene, which is considered to be derived from airborne contamination on the surface.

References

- [1] A. K. Geim and K. S. Novoselov: *Nature Materials* **6**, 183–191 (2007).
- [2] J. Avila et al.: *Sci. Rep.* **3** 02439 (2013).
- [3] J. Stoehr: *NEXAFS Spectroscopy* (Springer Berlin, 2003).
- [4] U. Bergmann, and P. Glatzel: *Photosynth. Res.*, **102**, 225 (2009).
- [5] D. Pacile et al.: *Phys. Rev. Lett.*, **101**, 066806 (2008).
- [6] L. Zhang et al.: *Phys. Rev. B* **86**, 245430 (2012).
- [7] B. Ilkiv et al.: *J. Nanosci. Nanotechnol.*, **12**, 8913-8919 (2012).
- [8] M. Niibe and T. Tokushima: *AIP Conf. Proc.*, **1741**, 030042 (2016).
- [9] M. Niibe, et al., *J. Electron Spectrosc. Relat. Phenom.*, **220**, 118-120 (2017).
- [10] M. Niibe, N. Takehira and T. Tokushima, *e-J. Surf. Sci. Nanotechnol.*, **16**, 122 (2018).
- [11] S. Suzuki et al., *J. Phys. Chem. C* **117**, 22123 (2013).
- [12] M. Niibe et al.: *AIP Conf. Proc.* **705**, 576 (2004).
- [13] R.A. Rosenberg et al.: *Phys. Rev. B* **33**, 4034 (1986).
- [14] Z. Li et al.: *Nature materials* **12**, 925 (2013).
- [15] V. Lee et al.: *J. Phys. Chem. Lett.* **1**, 1247 (2010).

Photopolymer Technology for Extreme Ultraviolet Lithography

Takeo Watanabe, Tetsuo Harada
Center for EUVL, LASTI, University of Hyogo

Abstract

EUV (extreme ultraviolet) lithography is the next generation lithography for the fabrication of semiconductor electronic devices in 10 nm node and beyond. The research group which was involved in national EUVL project in Japan has been processing the research and development of EUV lithographic technology including resist and mask technologies in collaborating with many research institutes, companies, and university in worldwide. This paper focuses on the development of EUV resist technologies including materials and evaluation tools for its exposure characteristics. The research group of University of Hyogo is playing an important role for the processing the EUV technology in worldwide. The future prospect for EUV lithographic technology is also discussed.

Keywords: EUV lithography, EUV resist, sensitivity, LER

Introduction

The semiconductor market is announced to be 421 billion dollars in 2017, and it achieved 21.7% market growth in comparison with total market of 2016. The market growth of Internet of Things (IoT) own to the advanced lithographic technology, because the advanced lithographic technology can lead semiconductor devices to have the low power consumption, low fabrication cost, fast speed data acquisition of large scaled data. According to the many progress of technologies related to Extreme ultraviolet lithography (EUVL), EUVL are facing to use in high volume manufacturing as an advanced lithographic technology for the fabrication of semiconductor devices around 2019. However, technical issues of EUVL for HVM still remains, which are the development of 1) EUV light source with high power and high stability, 2) EUV resist which satisfies high resolution, high sensitivity, low line edge roughness (LER), and low outgassing simultaneously, 3) EUV pellicle to protect from the particles from the surface of EUV mask, 4) defect free EUV mask including metrology. The research and development of EUV technology has been carried since 1995 at University of Hyogo. In 1989 NTT research group developed two aspherical imaging system, the 150 nm resist pattern was replicated. In 1996 semiconductor market required more advanced patterning tool using EUV lithography which can use in the production line to fabricate semiconductor devices. Thus, at NewSUBARU [1] synchrotron light facility of University of Hyogo, three aspherical imaging optics were designed and fabricated for the patterning of 70 nm hp on a 8 inches wafer using the synchronized

system between mask and wafer stages to enlarge the exposure area to be 30 mm×28 mm, which can fabricate two chips of DRAM. This was a collaboration work between University of Hyogo, Hitachi Central Research Lab. and Nikon research groups [2]. The three aspherical mirror optics was design by University of Hyogo in 1997 [3]. From 1999 to 2001, this work continues to the collaboration with University of Hyogo and ASET [4]. Figure 1 shows the EUV exposure tool which was developed at University of Hyogo and which was installed at BL03 beamlines of NewSUBARU. The figure error of each aspherical mirror was 0.58 nm in rms, and the substrate was Zerodur™. The exposure wavelength and numerical aperture were 13.5 nm and 0.5.

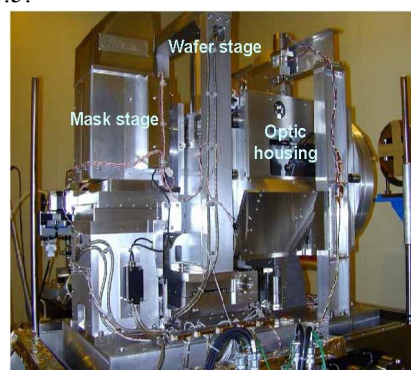


Fig.1. World 1st large exposure field EUV exposure tool for advanced lithography employing three aspherical mirror imaging optics for the patterning 60 nm resist pattern by synchronizing mask and wafer stages.

We succeed to replicate 60 nm hp and 45 nm isolated resist pattern on a 8 inches wafer with a large exposure area [4]. At NewSUBARU synchrotron light facility opened for common usage for EUVL, and Center for EUVL was established in 2010. Many companies, research institutes, and universities are visiting to use the EUV resist evaluation tools such as sensitivity measurement tool, EUV interference exposure tool, resist outgassing evaluation tool, resist transmission measurement tool, the soft X-ray absorption evaluation tool for EUV resist chemical reaction analysis, and the bright-field EUV microscope and EUV coherent EUV scatterometry microscope for EUV mask defect inspection. These tools were installed at BL03, BL09, and BL10 beamlines of NewSUBARU which are introduced in Fig 2. The paper focuses and describes the detail of the EUV resist evaluation tools. In addition, it describes EUV PAG bounded polymer resist for low LER. On a basis of these research and development, the advanced progress of EUV lithography for HVM is contributed.

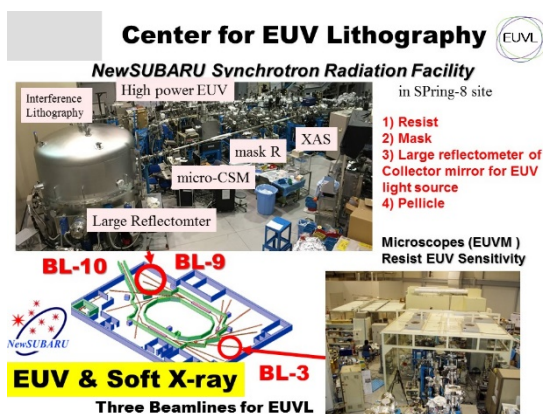


Fig. 2. Three beamlines such as BL03, BL09, and BL10 beamlines dedicate for research and development for resist and mask in EUV lithography.

EUV PAG bound resist for low LER and high sensitivity

As for EUV resist development, the most significant issues are the achievement of low LER and high sensitivity simultaneously. Specially to achieve of LER, the stochastic issue should be resolved. The LER causes by many origins which were listed in Table 1. We expected the most significant origin of stochastic is the spacial distribution of the chemical content such as PAG in the resist film in the case of chemical amplified resist (CAR). The PAG bounded polymer for CAR

which is shown in Fig.3(a) was introduced, designed, and synthesized [5-8], to reduce line edge roughness (LER) and increase sensitivity for a resist in extreme ultraviolet lithography (EUV) and electron beam (EB) lithography. A sulfonium salts group was supplied at side chain of base polymer system. The base polymer consists of copolymer of polyhydroxy styrene, solution inhibitor and monomer containing PAG as a backbone. Under EB exposure, a LER of 2.0 nm (3σ) is achieved using PAG bounded polymer. A LER of PAG bounded polymer is smaller than that of PAG blended polymer as shown in Fig.3(b). Under EUV exposure, E_0 sensitivity of 0.9 mJ/cm² and low outgassing characteristics are achieved.

Finally, it is succeeded to reduce LER to be 1/2 size with comparison of conventional CAR.

Table 1. The expected origins of LER which causes stochastic.

1)	Spatial distribution of functional material in resist functional groups, photosensitizers (photoacid generators), additives such as amines, etc.
2)	Solvent distribution in prebake process Spatial distribution of free volume
3)	EUV photon shot noise
4)	2ndry electron blur
5)	Solvent effect in PEB process Acid diffusion
6)	Development and rinse effects Spatial distribution of developer penetration and development process yield
7)	Out of band (OoB) light effect

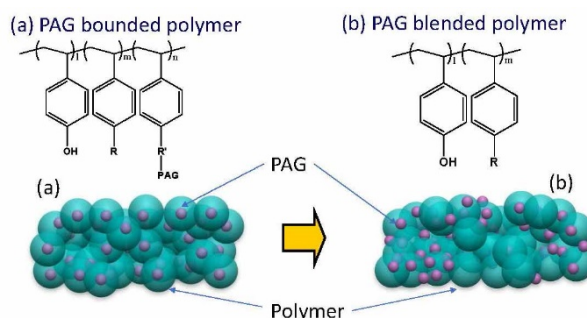


Fig. 3. PAG bound polymer and PAG blended polymer in chemically amplified resist materials.

EUV interference lithographic exposure tool

To accelerate the EUV resist development of 10-nm order, it is very significant to develop the EUV interference lithographic (EUV-IL) [9] exposure tool. The EUV interference lithography had been developed and replicated 15 nm line and

space (L/S) resist pattern by using two window-type transmission diffraction grating (TDG) on which has 30 nm L/S grating pattern. In addition, 28-nm-diameter-hole resist pattern had been replicated by four window-type TDG which has 40 nm L/S grating pattern [10, 11]. The SEM image of the replicated resist patterns of 15 nm L/S and 28 nm hole on a silicon wafer are shown in Fig. 4(a) and 4(b), respectively [12, 13].

The reduction of the vibration amplitude from a dry pump is a significant factor for the resist patterning of a small feature size in the EUV-IL exposure. The displacement of the vibration amplitude between the transmission diffraction grating and the wafer should be reduced to approximately 1/3 of the target resolution of 10 nm in EUV-IL [14]. In order to reduce the vibration, the high-rigidity trestle and low-vibration-dry-pumping system are employed adapted to the EUV-IL exposure chamber, and the relative-vibration amplitude suppressed to be less than 1 nm which is enough for the 10 nm patterning. In addition, 20 nm hp TDG has been fabricated using organic developer instead of 2.38%TMAH to change positive-tone to negative tone of the chemical amplified resist and adopted using dry development rinse (DDR) process [15]. As the results, it is now ready to evaluate the resolution of 10 nm using EUV-IL at NewSUBARU.

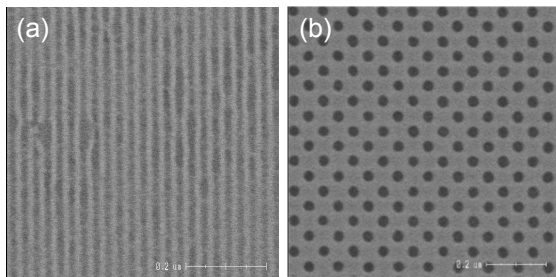


Fig. 4. The replicated a) 15 nm line and space and b) 28 nm hole pattern replicated by EUV interference lithographic exposure tool.

Resist outgassing evaluation tool

The Mo/Si multilayers used as imaging optics and a mask can be contaminated by carbon, which is originally an outgassing species of the hydrocarbons that decompose from the resist materials during EUV exposure. This carbon contamination reduces the total reflectivity of the imaging optics and mask, and affects the lithographic performance, including the

throughput and resist pattern replication resolution. This contamination should be reduced to maintain the lithographic performance; thus, the relationship between the carbon contamination and the outgassing species should be clarified.

ASML proposed a double-electron beam (EB) system to evaluate the contamination. They used one EB gun for exposure of the resist to induce outgassing from the resist, and they used another EB gun for exposure of the Mo/Si witness sample to reduce the adhesion of the contaminant. Because the outgassing and contamination efficiency seem to be quite different under EB and EUV exposure conditions, it is necessary to compare the contamination and outgassing behavior between the two types of exposure. It is also necessary to study the differences in contaminant adhesion between the exposure using a low EUV power and the exposure using a high EUV power that is comparable to that used in HVM EUV lithography. The novel tool for in situ evaluation of contaminating carbon layer thickness was therefore developed using an EUV power as high as that used in HVM. The photograph of this contamination evaluation system is shown in Fig. 5., and it was installed in the 10.8-m-long undulator BL-09C beamline at the NewSUBARU. This system has the quadropole mass spectrometer to measure the outgassing species and the in-situ ellipsometer to measure the carbon growth on a witness plate during the EUV exposure. This system can handle a resist/wafer size of 8 inches and a witness diameter of 1 inch. On a resist coated wafer, the exposure area size is approximately 2 mm (H) and 4 mm (V), and the exposure using a total power of in-band EUV light (300 mW/cm^2) that is as high as that required for high-volume manufacturing ($>100 \text{ mW/cm}^2$). The measured spot size of the *in-situ* visible light ellipsometer was focused to be area size of approximately $750 \mu\text{m} \times 750 \mu\text{m}$ on a witness sample of Mo/Si multilayers mirror to be able to detect the carbon layer thickness of 0.03 nm. In addition, the resist/wafer and witness stages have extremely low outgassing characteristics. Using the rotation stage for the resist/wafer, a fresh surface of the resist can be exposed continuously. Using this tool, a starting time of the adhesion point can be observed, and both the carbon contamination layer thickness and the outgassing species can be evaluated during the resist exposure by EUV light.

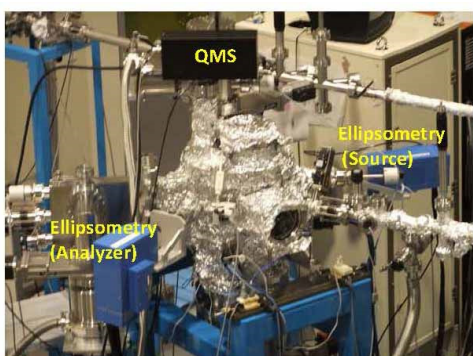


Fig. 5. Photographs of the resist outgassing evaluation tool which can measure the carbon growth on a Mo/Si MLs mirror surface using visible light *in-situ* ellipsometry.

Transmission measurement of EUV resist

Since the resist thickness in EUV lithography of which base material mainly consists of an organic material is thin, the EUV photon energy is not be used efficiently for the EUV chemical reaction. In order to increase the EUV photon energy chemical reaction efficiently, a resist having a high-absorption material compounds for the EUV photons has been developed. It has been studied to increase the absorption including high-absorption materials such as hafnium and zinc, tin oxide, tellurium. For the development of the next-generation highly sensitive resist materials, since it is significant to measure the EUV absorption coefficient accurately, it is necessary to measure the transmittance and resist thickness to obtain the absorption coefficient accurately. Thus, we have developed to evaluate the absorption coefficient of the EUV resist at BL10 beamline of NewSUBARU synchrotron light facility. In the previous paper [16], we measured the EUV resist transmittance on a freestanding membrane. However, since it was very difficult to coat resist on a membrane with high uniformity, the transmittance could not be measured accurately. Thus, we have developed the precise transmittance measurement method by coating resist on a photodiode directly [17], and the resist thickness on a photodiode was measured by XRR accurately instead on conventional method. Figure 6 shows the absorption coefficient computed with the transmittance and thickness measurement results by both NanoSpec6100 and XRR methods. The error bar indicates the 1% transmittance measurement error. The absorption coefficient using NanoSpec6100 result did not

have same value at 108 nm thickness. This error was due to the inappropriate optical structural model of the photodiode which has unknown layer structures. The values of the absorption coefficient obtained from the four film thicknesses measured by XRR are all within the measurement error range. As a result, the absorption coefficient was measured accurately with combining the photodiode substrate and XRR thickness measurement method. Since the error bar was minimized with the thickest resist sample, the sample resist thickness should be thick for accurate absorption evaluation in the photodiode method. The calculated absorption coefficient of this resist takes in account of the resist composition and the density of 1.3 g/cm² was approximately 4.6 and this value is quite different of our result of 3.8. As the results, the accurate measurement of EUV resist absorption coefficients using the method with combining the photodiode substrate and XRR thickness measurement were achieved.

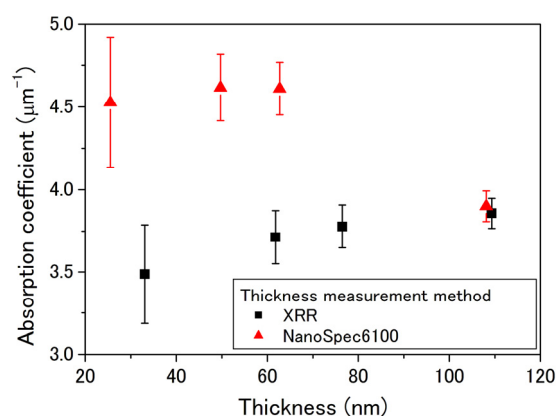


Fig.6. Absorption coefficient computation results in two methods of resist thickness measurement.

EUV resist chemical reaction analysis using soft X-ray absorption spectroscopy

The EUV resist technical issue is to achieve the high resolution, high sensitivity, low line-edge-roughness (LWR), and low outgassing. Since there is a trade-off relationship between the resolution, sensitivity, and LWR, the simultaneous achievement of the requirement has a difficulty. In this situation, the high sensitivity achievement has the highest priority, because the most significant issue of the EUV lithography is the achievement of the high power EUV source to

maintain the wafer throughput for HVM. If the highly sensitive EUV resist will achieve, it might be relaxing the requirement of the power of the EUV light source. In order to achieve high sensitivity of the EUV resist, the chemical reaction analysis using real EUV light is significant. In general, the content of the photosensitizing agent such as a photoacid generator (PAG) in the EUV chemically amplified resist material is approximately from 10 to 15% of the base resin. To analysis of the cation and anion of PAG, the conventional analysis methods such as XPS, FT-IR, and Raman spectroscopy have not enough sensitivity for the analysis of the chemical reaction analysis of the EUV resist. Thus, we applied x-ray absorption fine structure (XAFS) method for the chemical reaction analysis of the EUV resist material. In this method, the total electron yield method is used for the analysis of the chemical reaction, because this method is very sensitive even if the content of PAG is small. Since it is found that the decomposition reaction of the fluorine which consist of the onium salts employed as a PAG is significant in the previous study [19-21], we increase the detection sensitivity in the TEY method by refinement of the monochromator at the BL10 beamline. The W/Si aperiodic multilayer coated grating is employed for the monochromator to extend the photon energy region from 500 to 1100 eV as shown in Fig. 7 [22]. As the results, the absorption peak signal of the fluorine 1s core level can be measured clearly as shown in Fig. 8. As the results of the TEY-XAFS analysis applied to the EUV CA resist, it is found that to satisfy the specification of the EUV

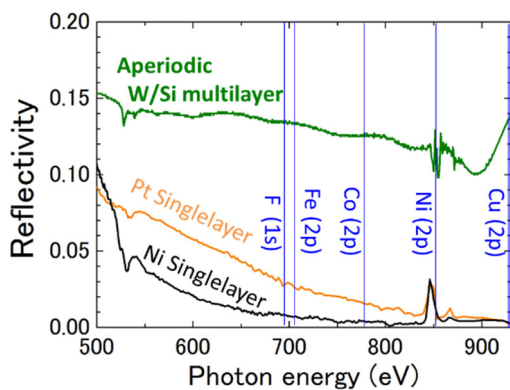


Fig.7. Reflectivity comparison of the wideband W/Si-multilayer, the Ni single-layer, the Pt single-layer samples

resist which require for high volume manufacturing, all the chemical reaction should be taken in account, such as the ionization and the direct excitation reactions, as shown in Fig.9. Increasing the sensitivity, it might have more space to achieve the low LWR resist [21].

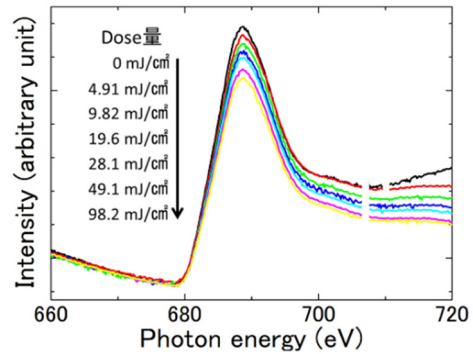


Fig.8. TEY-XAFS measurement result of the resist at fluorine absorption edge

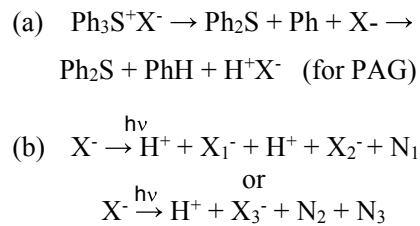


Fig.9. (a) The decomposition reaction by the secondary electron generated from the ionization reaction and (b) the decomposition reaction of the anion of PAG by the direct excitation reaction under EUV irradiation.

Conclusions

EUV (extreme ultraviolet) lithography is next generation lithography for the fabrication of semiconductor electronic devices in 10 nm node and beyond. The Center for EUVL of University of Hyogo plays the important role to contribute to progress the technology of resist and mask in EUV lithography. This paper only focused on the resist research and development. The research group which was involved in many national EUVL projects in Japan to process the research and development of EUV lithographic technology including resist and mask technologies in collaborating with many research institutes, companies, and university in worldwide.

Reference

1. Hashimoto S., Ando A., Amano S., Haruyama Y., Hattori T., Kanda K., Kinoshita H., Matsui S., Mekaru H., Miyamoto S., Mochizuki T., Niibe M., Shoji Y., Utsumi Y., Watanabe T., and Tsubakino H. *Trans. Mater. Res. Soc. Jpn.* **2001**, 26 783-786.
2. Murakami K., Oshino T., Kinoshita H., Watanabe T., M. Niibe M., M. Ito M., H. Oizumi H. and H. Yamanashi H. *J. Photopolym. Sci. Technol.* **1998**, 11, 565-570.
3. Watanabe T., Mashima K., Niibe M., and Kinoshita H. *Jpn. J. Appl. Phys.* **1997**, 36 (12B), 7597-7600.
4. Watanabe T., Kinoshita H., Nii H., Li Y., Hamamoto K., Oshino T., Sugisaki K., Murakami K., Irie S., Shirayone S., Gomei Y., and Okazaki S. *J. Vac. Sci. Technol.* **2000**, B18, 2905-2910.
5. Watanabe T., Fukushima Y., Shiotani H., Hayakawa M., Ogi S., Endo Y., Yamanaka T., Yusa S., and Kinoshita H. *J. Photopolym. Sci. Technol.*, **2006**, 19, 521-524.
6. Fukushima Y., Watanabe T., Ohnishi R., Kinoshita H., Shiotani H., Suzuki S., Hayakawa M., Endo Y., Yamanaka T., and Yusa S. *J. Photopolym. Sci. Technol.* **2007**, 20, 419-422.
7. Fukushima Y., Watanabe T., Ohnishi R., Shiotani H., Suzuki S., Hayakawa M., Endo Y., Yamanaka T., Yusa S., and Kinoshita H. *Jpn. J. Appl. Phys.* **2008**, 47, 6293-6296.
8. Nakahara T., Watanabe T., Kinoshita H., Mochizuki T., Takahara Y., Uozumi Y., and Nakagawa K. *Jpn. J. Appl. Phys.* **2009**, 06FC10.
9. Solak H. H., David C., Gobrecht J., Golovkina V., Cerrina F., Kim S. O., Nealey P. F. *Microelectronic Engineering* **2003**, 67, 56-64.
10. Yamaguchi Y., Fukushima Y., Iguchi T., Kinoshita H., Harada T. and Watanabe T. *J. Photopolym. Sci. Technol.* **2010**, 23 681-686.
11. Fukushima Y., Yamaguchi Y., Iguchi T., Urayama T., Harada T., Watanabe T., and Kinoshita H. *Microelectric Engineering* **2011**, 88, 1944-1947.
12. Urayama T., Watanabe T., Yamaguchi Y., Matsuda N., Fukushima Y., Iguchi T., Harada T., Kinoshita H. *J. Photopolym. Sci. Technol.* **2011**, 24, 153-157.
13. Tanino H., Fukui T., Emura K., Hayashi Y., Fukuda Y., Kuki M., Yamaguchi M., Harada T., Watanabe T., Kinoshita H., *I. E. E. Jpn.* **2014**, 7.
14. Fukui T., Tanino H., Fukuda Y., Watanabe T., Kinoshita H., and Harada T. *J. Photopolym. Sci. Technol.* **2015**, 28, 525-529.
15. Yoshifuji M., Niihara S., Harada T., and Watanabe T. *J. Photopolym. Sci. Technol.* **2018**, 31, 215-210.
16. Ohnishi R., Watanabe T., Fukushima Y., Osugi M., and Kinoshita H. *Jpn. J. Appl. Phys.* **2009**, 48, 06FA08.
17. Mamezaki D., Watanabe M., Harada T., Watanabe W. *J. Photopolym. Sci. Technol.* **2016**, 29, 749-752.
18. S. Niihara S., D. Mamezaki D., M. Watanabe M., T. Harada T. , and T. Watanabe T. *J. Photopolym. Sci. Technol.* **2017**, 30, 87-93.
19. Watanabe T., Haruyama Y., Shiono D., Emura K., Urayama T., Harada T., and Kinoshita H. *J. Photopolymer Sci. Technol.* **2012**, 25, 569-574.
20. Watanabe T., Emura K., Shiono D., Haruyama Y., Muramatsu Y., Ohmori K., Sato K., Harada T., and Kinoshita H. *J. Photopolym. Sci. Technol.* **2013**, 26, 635-641.
21. Emura K., Watanabe T., Yamaguchi M., Tanino H., Fukui T., Shiono D., Haruyama Y., Muramatsu Y., Ohmori K., Sato K., Harada T., and Kinoshita H. *J. Photopolym. Sci. Technol.* **2014**, 27 631-638.
22. Kuki M., Uemura T., Yamaguchi M., Harada T., Watanabe T., Muramatsu Y., and Kinoshita H., *J. Photopolym. Sci. Technol.* **2015**, 28, 531

Diffraction Efficiency Measurement of a Transmission Grating for 10-nm EUV Resist Evaluation

Mana Yoshifuji, Shota Niihara, Tetsuo Harada, and Takeo Watanabe
Center for EUV lithography, LASTI, University of Hyogo

Abstract

We have developed the EUV interference lithographic exposure tool at BL-9 beamline to evaluate the resist patterning performance. The transmission grating is a key component in the EUV interference lithography (EUV-IL), which generate EUV interference pattern. To replicate 10 nm line-and-space (L/S) resist pattern on a wafer, 20 nm L/S pattern is required for the transmission grating. The pitch size of the interference fringes is a half size of the absorber pattern of the transmission grating. We fabricated very high-aspect-ratio grating made from spin-on-carbon material using the dry development process. EUV diffraction efficiencies of the fabricated grating were measured at BL-10 beamline. The measured EUV diffraction efficiencies are 14%, 11%, and 4% for 40 nm, 30 nm, and 20 nm L/S pattern grating, respectively. Using this grating, 20 nm, 15 nm, and 10 nm resist pattern could be replicated on a resist.

Introduction

EUV lithography is a lithographic technology for the manufacturing of semiconductor electronic devices, and it is used for high volume manufacturing of logic device. In addition, a patterning technology of 5 nm node which corresponds to 10-nm half pitch is required in 2024, which requirement was listed in the international roadmap for devices and systems (IRDS2017)¹⁾. There are several issues for high-volume manufacturing of semiconductor-device fabrication in EUV lithography. One of the critical technical issues in EUV lithography is the development of EUV resist which should have the high resolution, the high sensitivity, the low line-width roughness, and low outgassing simultaneously. Thus, the EUV interference lithographic exposure tool had been installed at the BL-9 beamline which had employed the 10.8-m-long undulator of the NewSUBARU synchrotron light facility²⁾ as a light source.

EUV-IL system can generate EUV interference fringes to replicate the line-and-space (L/S) resist pattern on a wafer without any optical aberrations, because these fringes were generated by the two-beam interference from a transmission diffraction grating. In addition, the pattern has high optical contrast due to very low flare. In the case of the EUV exposure system which employs the imaging optics such as reflection type mirrors, the flare degrades the light contrast of the resist pattern. The fringe-pitch size generated on a resist in EUV-IL is a half-pitch size of the diffraction grating, which is not depended on the exposure wavelength. Thus, to replicate 10-nm-L/S-resist pattern on a wafer, the diffraction grating with 20-nm L/S pattern is required to fabricate.

In our previous work, the 15-nm L/S resist pattern was generated on a wafer using the 30-nm-L/S-diffraction grating^{3,4)}. TaN material was employed as the grating-absorber material, which had both the high diffraction efficiency and nano-pattern replication property. Required diffraction efficiency in the IL system is more than 5%. The calculated diffraction efficiency of the 30-nm-thick TaN grating is approximately 7%. However, the fabrication of the TaN grating was difficult due to etching difficulty. Thus, we applied spin-on-carbon (SOC) material to the grating absorber.⁵⁾ The calculated diffraction efficiency of the SOC grating with

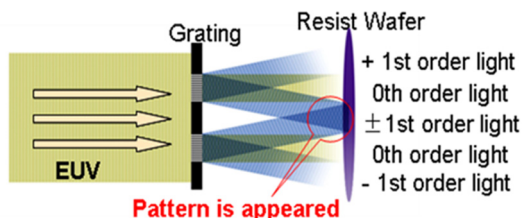


Fig. 1 Schematic drawing of EUV-IL system. Fringe pattern is generated by the two-beam interference of the diffraction light.

The principal of the EUV interference lithography (IL) is shown in Fig. 1. The

90-nm-thick is 6% shown in Fig. 2. A dry-development-rinse (DDR) process was applied to fabricate the SOC diffraction grating pattern with high aspect ratio. The 20-nm L/S SOC diffraction grating with the high-aspect ratio of 5.9 was fabricated shown in Fig. 3. This report focuses on the measurement of the diffraction efficiency of fabricated SOC diffraction grating.

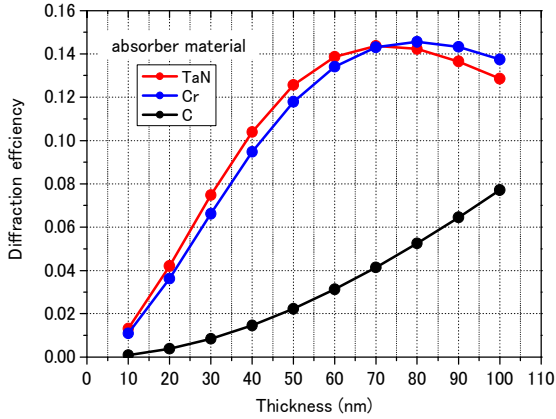


Fig. 2. The diffraction efficiency of a transmission grating with TaN, Cr, and carbon materials at EUV region.

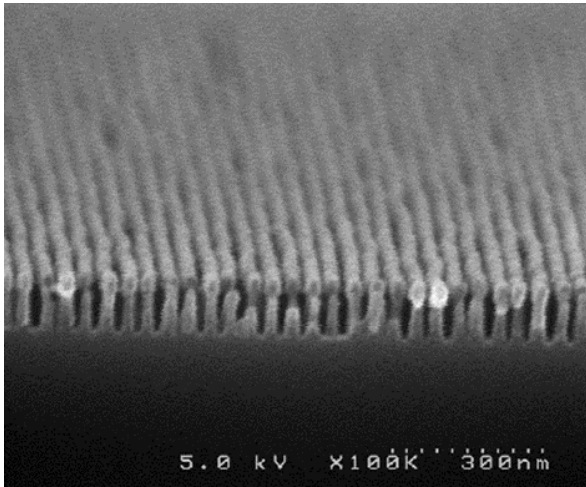


Fig. 3 Cross-sectional SEM image of the 20-nm L/S SOC grating pattern which has quite high aspect ratio of 5.9.

Experiments and Results

The diffraction efficiency of the fabricated transmission grating was measured at BL-10 beamline. A photograph of the measurement setup are shown in Fig. 4. At the end stations of this beamline, the measurements of the reflectivity of EUV optics and soft X-ray scattering from the polymer sample are carried out usually.

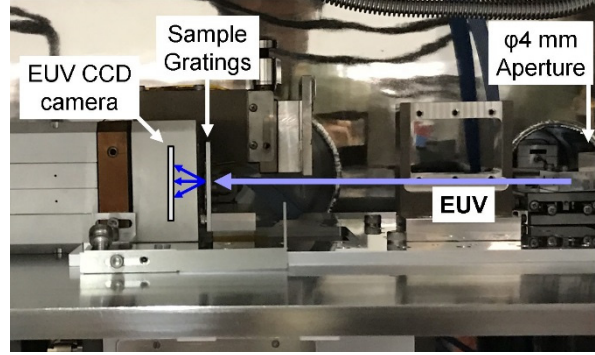


Fig. 4 Photograph of the diffraction efficiency measurement setup.

EUV light was exposed to the sample gratings from right side to left side. The wavelength resolution of $\lambda/\Delta\lambda$ is approximately 1,300 at the EUV wavelength of 13.5 nm. The beam size is 5 mm in horizontal and 15 mm in vertical directions, which was cut by the 4-mm-diameter pinhole. The beamline focal point is at the distance of 2.1 m upstream from the sample. Thus, the incident beam is almost parallel. The higher diffraction-order light generated from the monochromator was completely reduced by a reflection-type high-order-cut filter using two Mo mirrors at the grazing incidence angle of 15° . In-vacuum CCD camera (MTE-2048B, Princeton instruments) was located just after the sample. The distance from the sample to the CCD image sensor was approximately 14 mm. The active area size of this CCD was $27.8 \text{ mm} \times 27.8 \text{ mm}$. The acceptance angle of the CCD camera was approximately 45° . We measured CCD image with and without samples. With the sample, the diffractions from the samples were recorded by the CCD image.

The diffraction efficiency ε of +1st order diffraction without considering the absorption of the Si_3N_4 membrane was calculated by the following Eq. 1.

$$\varepsilon_{D+1} = \frac{I_{D+1}}{I_0 \cdot T_{\text{Si}_3\text{N}_4}} \quad (1)$$

Where $T_{\text{Si}_3\text{N}_4}$, I_0 , and I_{D+1} show the calculated transmittance of Si_3N_4 layer, the intensity of the incident EUV light, and the diffraction intensity of +1st order, respectively. The calculated transmittance of the Si_3N_4 material was 45.8% for the 91-nm thick Si_3N_4 membrane. This thickness was measured by x-ray reflectivity of

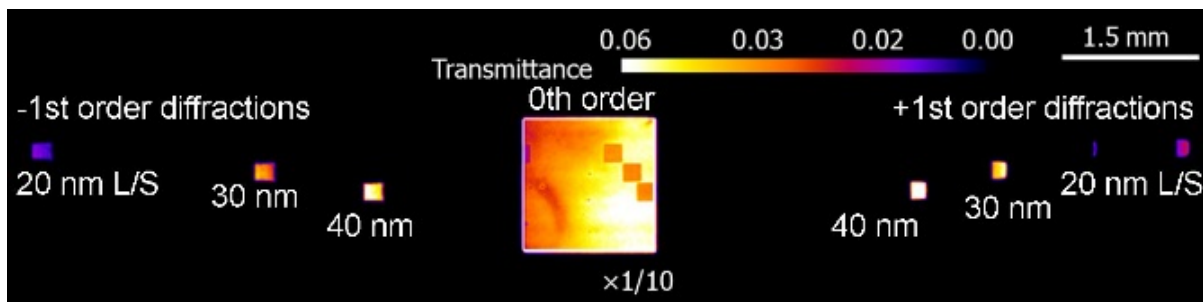


Fig. 5 CCD camera image of EUV diffraction measurements for 20-nm, 30-nm, and 40-nm L/S diffraction gratings. +1st and -1st order diffractions were recorded.

the Si_3N_4 wafer.

Fig. 5 shows the diffraction image of a grating which was recorded by the CCD camera. The intensity scale shows the transmittance. In the center region of 0th order diffraction, the intensity is shown in 1/10 scale in comparison with the other weak diffractions, and the square membrane and 0th order diffraction are observed and recorded. There were -1st and +1st order diffractions at bothside. The diffraction angle depends on the pattern size. The patterns sizes of the diffractions are 20 nm, 30 nm, and 40 nm L/S grating from the top to bottom. As the results, the diffraction efficiency of the 20-nm L/S SOC-pattern was approximately 4.4% for the grating. This diffraction efficiency of 4.4% is acceptable for the EUV-IL system to replicate the 10-nm resist pattern on a wafer. Those of 30 and 40 nm L/S pattern were 10 and 14% for the grating, respectively. These high diffraction efficiencies were very effective for the EUV-IL system to replicate resist pattern on a wafer.

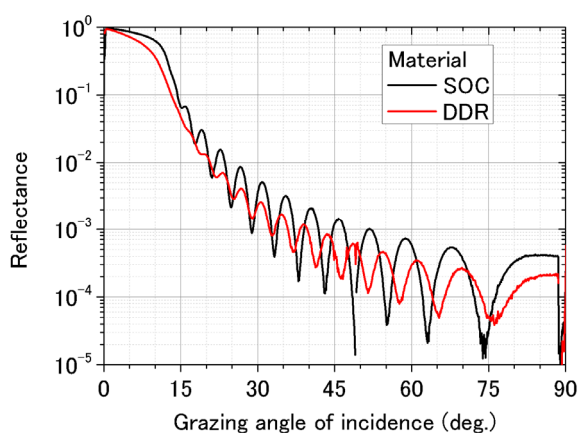


Fig. 6 Measurement result of EUV angular reflection spectra of the SOC and the DDR material coated on a Si wafer.

At large-pitch-size gratings of 30-nm and 40-nm L/S, the diffraction efficiency were quite higher than the calculation value of 6% as shown in Fig. 2. In this calculation, pure carbon material with a density of 1.2 g/cm³ is used for the grating material such as SOC. Since the SOC material will not be pure carbon, the actual diffraction efficiency might be higher than the calculation. Thus, we measured the actual optical index of the SOC and the DDR material using reflection measurement. The angular reflection spectra are shown in Fig. 6, which were measured at the same BL-10 beamline. The SOC and DDR materials are coated on the Si wafer under the same condition. The analyzed optical index of the SOC and DDR material are n: 0.9777 and k: 0.0038, and n: 0.980 and k: 0.0074, respectively. The calculated diffraction efficiency on a basis of these actual optical index are 11%. The residual difference might be caused by the difference of the actual Si_3N_4 -layer thickness, or the difference of its optical index in the transmission calculation by Eq. 1.

The EUV diffraction efficiencies of the fabricated gratings were measured to be 14%, 11%, and 4% for 40 nm, 30 nm, and 20 nm L/S pattern grating, respectively. Using these gratings, 20 nm, 15 nm, and 10 nm resist pattern might be replicated on a resist. And it was found that it has sufficient diffraction efficiency for interferometric exposure using synchrotron radiation.

We will evaluate the 10-nm-L/S-patterning performance of the EUV resists using this high-aspect-ratio grating adapted to the EUV-IL system in near future. This high-aspect-pattern-fabrication process can also be applied for the fabrication process of Fresnel-zone plate (FZP) for the usage in the soft x-ray region. A metal-absorber FZP could be fabricated using this high-aspect organic

pattern, where the expected metal thickness was over 50 nm. Especially in soft-x-ray region, such metal structure will have high diffraction efficiency.

References

1. International Roadmap for Devices and Systems (IRDS) 2017 [<https://irds.ieee.org/>].
2. Y. Fukushima, N. Sakagami, T. Kimura, Y. Kamaji, T. Iguchi, Y. Yamaguchi, M. Tada, T. Harada, T. Watanabe, and H. Kinoshita; *Jpn. J. Appl. Phys.*, 49 (2010) 06GD06.
3. Y. Yamaguchi, Y. Fukushima, T. Harada, T. Watanabe, and H. Kinoshita; *Jpn. J. Appl. Phys.*, 50 (2011) 06GB10.
4. T. Urayama, T. Watanabe, Y. Yamaguchi, N. Matsuda, Y. Fukushima, T. Iguchi, T. Harada, and H. Kinoshita; *J. Photopolym. Sci. Technol.*, 24 (2011) 153.
5. M. Yoshifuji, S. Niihara, T. Harada and T. Watanabe; *J. Photopolym. Sci. Technol.*, 31 (2018) 251.

Deterioration Analyses of CFRP Surface

Hideo Kobayashi¹, Yosuke Azuma¹, Shogo Suehiro¹,
Sohta Hamanaka², Yuki Tobita², Takuya Motokawa², and Yasuji Muramatsu²

¹ Sumika Chemical Analysis Service, Ltd., ² Graduate School of Engineering, University of Hyogo,

Abstract

We conducted the deterioration analyses of CFRP by using soft X-ray absorption spectroscopy at BL10 / NewSUBARU. In this report, we discuss the change in the surface condition due to heat treatment.

Introduction

Carbon fiber reinforced plastics (CFRP) is widely used in many products, such as airplanes and mechanical parts. CFRP composite materials have excellent mechanical characteristics such as specific strength, specific stiffness, and corrosion resistance. Evaluation of the degradation properties of CFRP is necessary and important to enhance its reliability.

The purpose of this study is to analyze heat treatment effect for CFRP by using soft X-ray absorption spectroscopy (XAS) with total electron yield (TEY) method at BL10 / NewSUBARU.

Experiments

CFRP was heated at 200 °C for 0.5 h, 4 h, 8 h, 24 h and 48 h. After heat treatment, CFRP was cut about 20 mm × 10 mm.

XAS measurement was performed across carbon *K*-edge, nitrogen *K*-edge and oxygen *K*-edge (CK, NK and OK) with TEY method. The incident angle of soft X-ray was tuned to 90°, 54.5° and 30°. All XANES spectra were normalized at σ^* peaks at 290 – 295 eV in CK-edge and 537 – 541 eV in OK-edge.

Results and Discussion

Figure 1 shows microscope images of CFRP surface. The CFRP surfaces of 0 h, 0.5 h, 4 h and 8 h look smooth and those of 24 h and 48 h look rough. This is because the polymer of CFRP was melted and carbon fiber was exposed.

Figure 2 and 3 show X-ray absorption near-edge structure (XANES) spectra for CK-edge and OK-edge of CFRP. The incident angle of soft X-ray was 54.5°.

Peak intensities of 285.5 eV and 288.0 eV in CK-XANES, and 532.5 eV in OK-XANES obviously changed depending on heating time. In addition, the subtle difference could be observed in 0.5 h for heating. This difference could not be observed by microscope. Those peak intensities indicate that the melting of polymer and the exposure of carbon fiber began from the beginning

of heating.

Figure 4 shows the orientation angle of C=O bond by OK-XANES. The angle between the perpendicular π^* orbital to the substrate surface and the molecular plane was calculated according to the method of previous study^[1]. We judged the orientation random if the orientation angle is around 54.7°.

The orientation angle decreased at 0.5h, and that increased and became random structure as the heating time increased. It is speculated that the C=O orientation was detected at the beginning of heating, however the melting of polymer and the exposure of carbon fiber made C=O orientation random.

Figure 5 shows the intensity ratio $O\sigma^* / C\sigma^*$ of CFRP for heating time. $O\sigma^*$ is a σ^* peak intensity of OK-XANES and $C\sigma^*$ is that of CK-XANES before normalization.

The intensity ratio gradually increased in 8 h or less although that increased sharply after 8 h. It is probable that the oxidization behavior of XANES spectra was due to a functional group of the oxidized polymer and that of the exposed carbon fiber. XAS measurement for a carbon fiber alone and a polymer alone also need to be examined in future studies.

Reference

[1] F. Zheng, B. N. Park, S. Seo, P. G. Evans, F. J. Himpsel: *J. Chem. Phys.*, **126**, 154702 (2007).

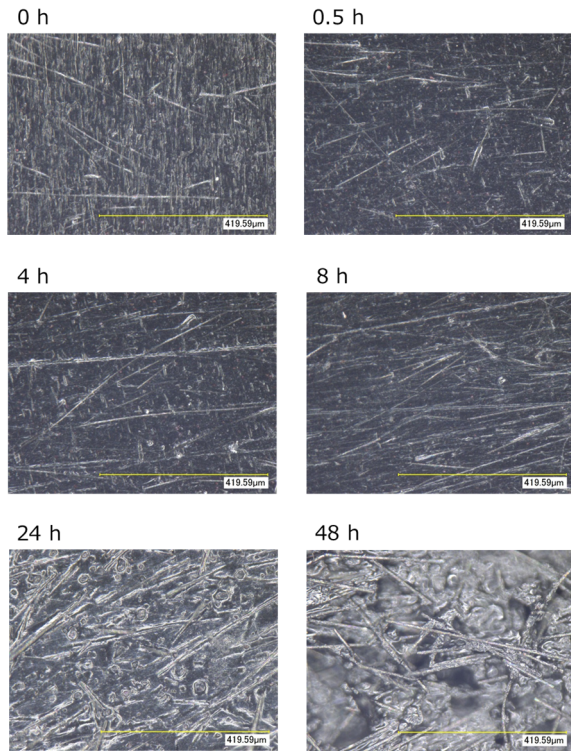


Figure 1. Microscope images of CFRP surface.

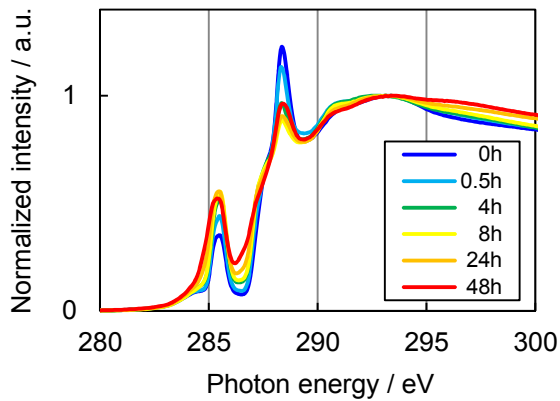


Figure 2. CK-XANES spectra of CFRP.

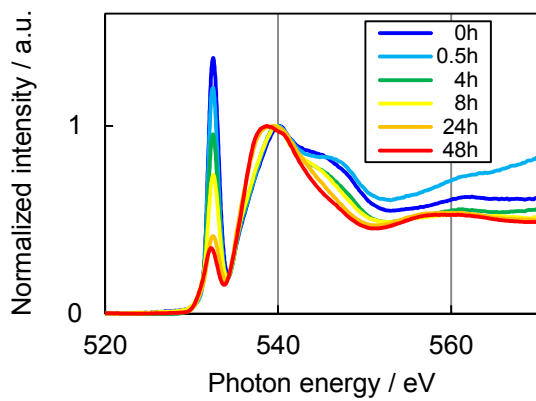


Figure 3. OK-XANES spectra of CFRP.

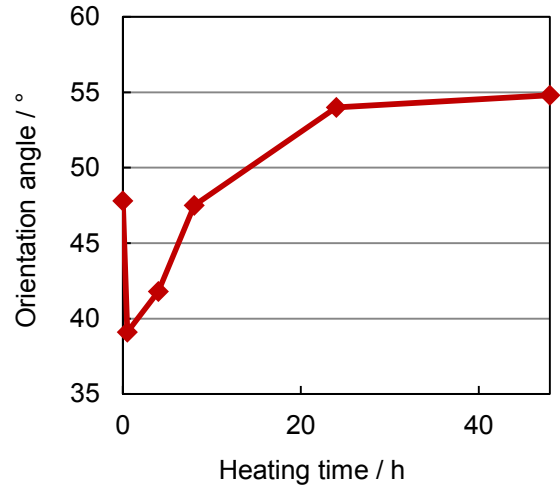


Figure 4. Orientation angles of C=O bond for heating time.

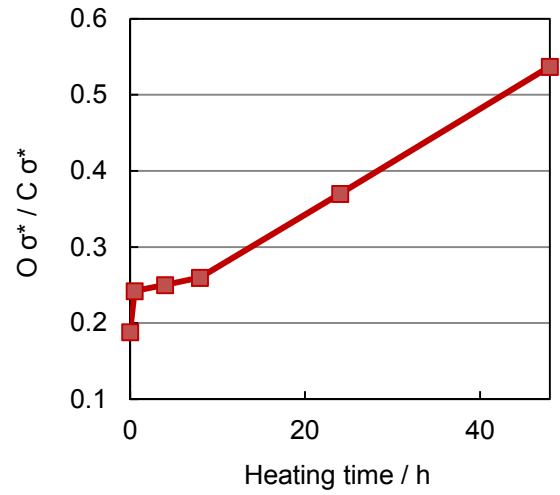


Figure 5. Intensity ratio $O\sigma^* / C\sigma^*$ for heating time.

Soft X-ray absorption measurements of self-standing polyethylene thin films using a transmission method

Yuya Matsumoto and Yasuji Muramatsu
Graduate School of Engineering, University of Hyogo

Abstract

To experimentally determine the mass absorption coefficient (μ) in soft X-ray regions of sp^3 carbon atoms, we have measured X-ray absorption spectra of polyethylene (PE) thin films using a transmission mode in BL10/NewSUBARU. Thickness of the measured PE films were 1.4 ~ 2.8 μm . Measured μ spectra in the 400~600 eV region were approximately agree to the theoretical spectrum. However, the measured μ spectra in CK region were smaller than the theoretical spectrum. This shows that the measured PE films were too thick to correctly measure μ in CK region.

1. Introduction

To determine the mass absorption coefficient (μ) from X-ray absorption measurements, a transmission method should be basically used according to the Lambert-Beer's law. However, in soft X-ray region, the value of μ is generally so large that self-standing thin samples should be prepared and it is experimentally hard to perform the transmission method. Therefore, a total-electron-yield (TEY) method is often used in soft X-ray absorption measurements.

Recently we have tried to determine the μ of sp^2 -carbon atoms by using ultra-thin graphite films [1]. In the next step, we are trying to determine the μ of sp^3 -carbon atoms. The most typical material consisting of sp^3 -carbon is diamond. Transmission length in CK region of diamond (density, $\rho=3.5 \text{ g cm}^{-3}$) is estimated to be less than 50 nm. However, it is difficult to get such the self-standing ultra-thin diamond films. Hence, we have focused on polyethylene (PE) films, because its low density ($\rho < 1 \text{ g cm}^{-3}$) and longer transmission length in CK region. Figure 1 shows the calculated transmission length of PE in soft X-ray region. The calculations were performed with the on-line system of the Center for X-Ray Optics (CXRO) [2,3]. The 200 nm-thick PE sufficiently transmits X-rays in CK region, and 1 μm -thick PE transmit ~500 eV X-rays. This means that μ in soft X-ray region can be experimentally determined by using 200 nm ~ 1 μm -thick PE films with a transmission mode.

In the present study, as the first attempt, we have measured soft X-ray absorption spectra of 1.4 ~ 2.8 μm -thick PE films.

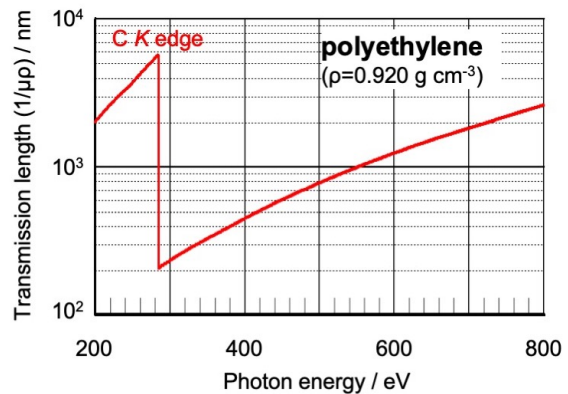


Fig. 1 Calculated transmission length in the 200 ~ 800 eV region of polyethylene film.

2. Experiments

Linear-low-density PE thin films (thickness : 2.8 μm , density: 0.920 g cm^{-3}) were supplied from Shibataya Kakoshi Co., Ltd. The 2.8- μm thick PE film was manually stretched to the thickness of 1.4 μm and 1.7 μm . These self-standing 1.4 ~ 2.8 μm -thick PE films were placed on an Al substrate which opened $3\text{mm}^{\text{H}} \times 5\text{mm}^{\text{W}}$ window, and held at both edges of the window frame using conductive carbon tapes, as shown in Figure 2.

Soft X-ray absorption measurements of the PE films were performed in the XRR (X-ray reflectivity) chamber at the BL10/NewSUBARU.

Intensity of transmitted X-rays through the PE films were measured with a photodiode detector. TEY spectra of the PE films were measured by monitoring sample current through the Al substrate during soft X-ray irradiation onto the PE film adhered to the carbon tape.

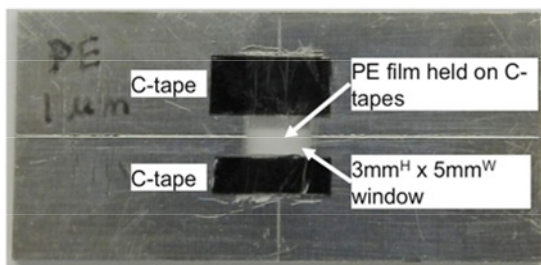


Fig. 2 Photo of PE film put on an Al substrate.

3. Results and Discussion

Measured transmittance, absorbance and μ in the 200 ~ 600 eV region of the PE films are shown in Figure 3. Transmittance and absorbance varied systematically with film thickness and showed a reasonable trend. CK edge can clearly observed near 280 eV both in the transmittance and absorption. The μ spectra were converted from absorbance spectra with a standard density of 0.920 g cm^{-3} and film thickness. Calculated μ spectrum is described on the measured μ spectra. In the 400 ~ 600 eV region, the measured μ spectra are in good agreement to the calculated spectrum. This is almost consistent with the transmission length shown in Figure 1, and it is considered that the μ spectra of PE can be correctly measured. However, in the CK-edge ~ 400 eV region, the measured μ spectra are significantly lower than the calculated μ , because the measured PE thickness is too thick to measure μ in the region. Actually, CK-XANES measured with a transmission mode (*i.e.* absorbance) were different from that with a TEY mode. This confirms that the 1.4 ~ 2.8 μm -thick PE films was too thick to measure μ in CK region.

We are now preparing to make thinner PE films with a spin-coating method.

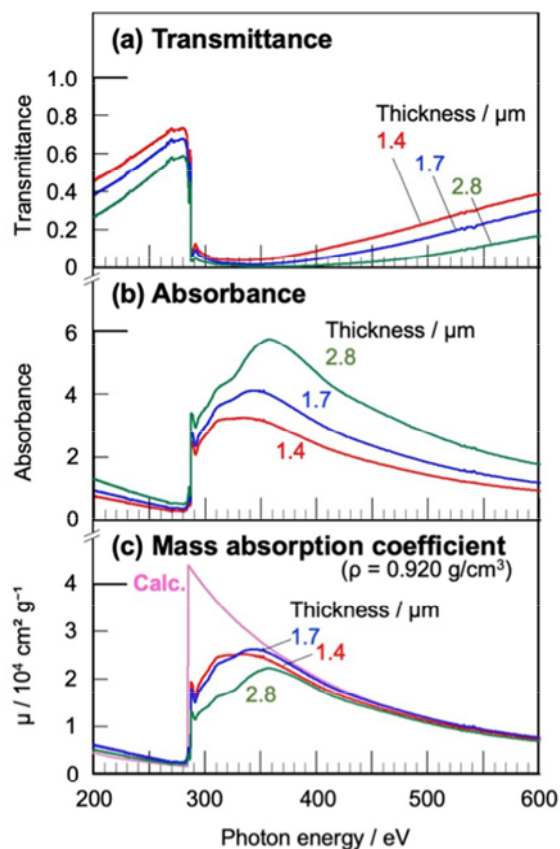


Fig. 3 Comparisons of the soft X-ray transmittance (a), absorbance (b), and μ (c) in the 200 ~ 600 eV region of PE films of each thickness.

References

- [1] Y. Muramatsu, Y. Soneda, and E. M. Gullikson, The 40th International Conference on Vacuum Ultraviolet and X-ray Physics, VUVX19, Poster 28 (2019).
- [2] http://henke.lbl.gov/optical_constants/
- [3] B.L. Henke, E.M. Gullikson, and J.C. Davis, Atomic Data and Nuclear Data Tables Vol. **54**, 181-342 (1993).

Surface structural analysis of nanodiamond by using soft X-ray absorption spectroscopy and the first principle calculations

Tatsuki Maeda and Yasuji Muramatsu
Graduate School of Engineering, University of Hyogo

Abstract

To clarify the surface structure of nanodiamond, soft X-ray absorption spectra of various detonation nanodiamond (DND) samples were measured in BL10 / NewSUBARU. CK-XANES of DND were theoretically analyzed by using the first principle calculation package of CASTP. XANES analyses suggest that surface of DND particles can be covered with sp^2 carbon atoms forming polycyclic hexagonal and/or pentagonal rings.

1. Introduction

Nanodiamonds have attracted much attention as functional materials because of their excellent mechanical and electrical properties. To develop the excellent functional nanodiamonds, surface structural analysis is important, because surface effect should become significant in the nano-scale particles.

Soft X-ray absorption spectroscopy (XAS) is a powerful tool for characterization of low-Z materials. Especially, XAS with a total-electron-yield (TEY) method easily provides electronic structure information on quasi-surface of materials. Local structure can be clarified from the XAS analysis using the first principle calculations.

In this study, to clarify the surface structure of nanodiamond, we have measured XAS spectra of various DND samples and theoretically analyzed the spectra.

2. Experiments and calculations

Sixteen DND powder samples were prepared by Daicel Corporation. Depending on the detonation conditions, the samples were labelled as NDD1 ~ 3, NDA1 ~ 7, and NDT1 ~ 6. These samples were held on indium substrate for XAS measurements. XAS measurements including CK- and OK-XANES were performed in the analysis chamber at BL10/NewSUBARU [1] using a total-electron-yield (TEY) method.

Theoretical XANES analysis was performed by using the first-principle calculation package of CASTEP [2]. Appropriate nanodiamond cluster was put in the center of a supercell. In order to suppress intermolecular interaction, the distance between the supercell boundaries and the model was set to longer than 5 Å. After the structure optimization by the Material Studio package, ground-state

calculations were performed. Then, excited-state calculations were carried out by providing core hole in the 1s orbital of the target atom. Transition energy was corrected by the Mizoguchi method [3].

3. Results and Discussion

Fig.1 shows the CK-XANES of the DND samples with a reference HOPG. XANES of DND samples exhibit the similar profile of diamond. However, each DND sample exhibits

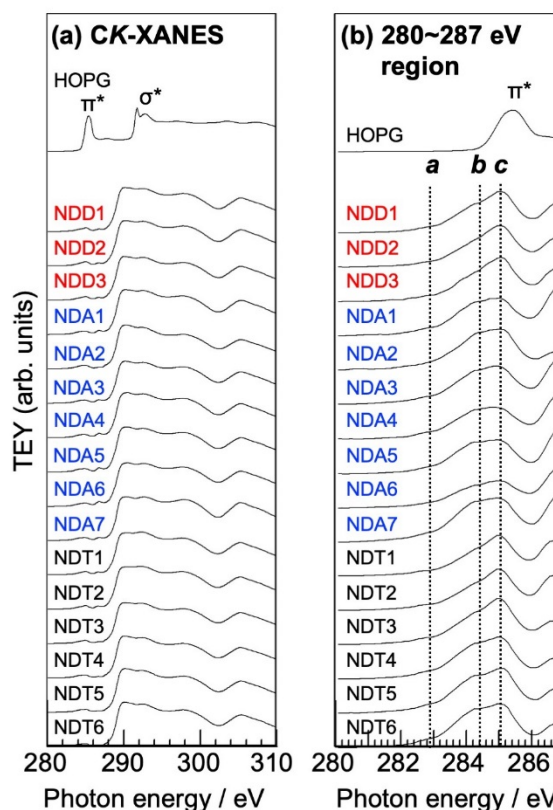


Fig. 1 CK-XANES (a) of nanodiamond samples with a reference HOPG. Right panel (b) shows the enlarged spectra in the 280 – 287 eV region.

small peaks near 285 eV corresponding to the π^* peak of HOPG. The enlarged spectra in the 280 ~ 287 eV region clearly shows the three structures (denoted as $a \sim c$) as π^* peak. This indicates that DND includes slightly sp^2 carbon atoms, which agrees to the previous studies on bucky diamonds [4].

To clarify the local structure of DND having sp^2 carbon atoms, we have calculated CK-

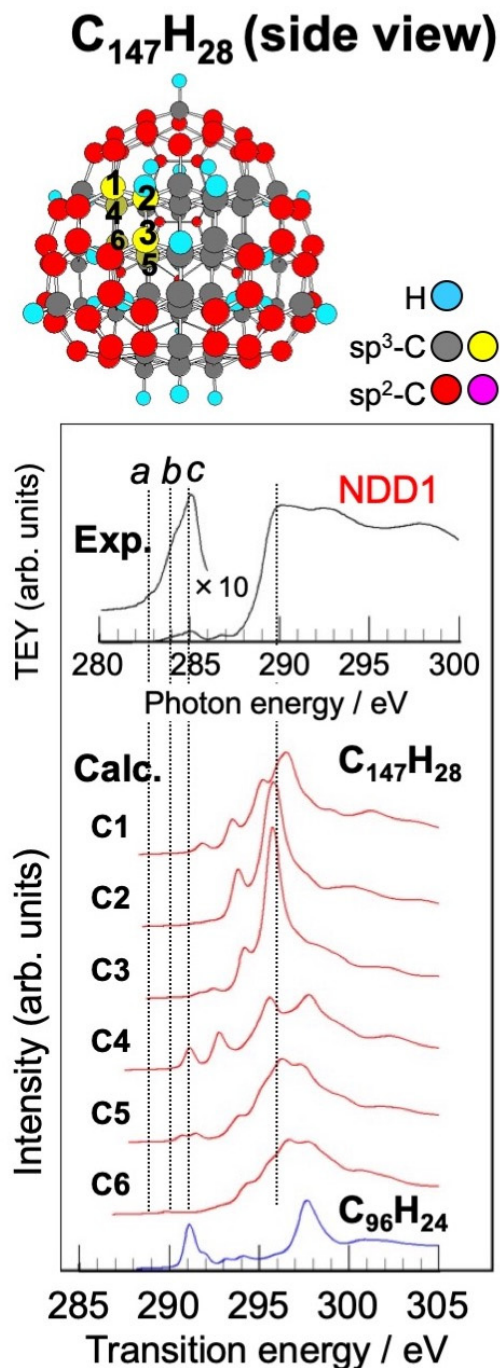


Fig. 2 Calculated CK-XANES of surface carbon atoms in the bucky diamond model ($C_{147}H_{28}$), compared to the measured CK-XANES of NDD1.

XANES of proposed bucky diamond model by using CASTEP. Figure 2 shows a calculation model ($C_{147}H_{28}$) and calculated CK-XANES of the focusing carbon atoms labelled as C1~C7 in the figure, comparing to the measured CK-XANES of NDD1. This calculation model has a diamond core cluster consisting of sp^3 carbon atoms and is covered with polycyclic hexagonal and/or pentagonal rings consisting of sp^2 carbon, which is called as bucky nanodiamond. The σ^* peak of the calculated XANES was adjusted to the σ^* peak energy position in the measured XANES. In the calculated XANES of sp^2 -carbon atoms, small peaks are observed in the lower-energy position from the σ^* peak. Such the lower-energy peaks of surface sp^2 -carbon atoms result in the measured small π^* peaks. However, the measured peaks cannot be completely reproduced by the calculated XANES. Other surface structures including oxidized structures should be considered to assign them. Actually, OK-XANES was clearly observed in the DND samples.

XANES calculations of surface-oxidized bucky diamond cluster models have been in progress.

Reference

- [1] Y. Muramatsu, A. Tsueda, T. Uemura, K. Nambu, T. Ouchi, T. Harada, T. Watanabe, and H. Kinoshita, LASTI Annual Report, 17, 29-30 (2015).
- [2] J. Clark, M. D. Segall, C.J. Pickard, P. J. Hasnip, M. J. Probert, K. Refson, and, M. C. Z. Payne, *Krystallogr.*, 220, 567-570 (2005).
- [3] T. Mizoguchi, I. Tanaka, S.-P. Gao, and C. J. Pickard, *J. Phys. Condens. Matter*, 21,104204 (2009).
- [4] J.-Y. Raty, G. Galli, C. Bostedt, T. W. van Buuren, and L. J. Terminello, *Phys. Rev. Lett.* 90, 037401 (2003)

Direct detection of PM2.5 collected on insulating membrane filters using a total-electron-yield soft X-ray absorption spectroscopy

Takuya Motokawa and Yasuji Muramatsu
Graduate School of Engineering, University of Hyogo

Abstract

We have proposed a new method for direct detection of particulate matter (PM) 2.5 collected on membrane filters by using a total-electron-yield (TEY) soft X-ray absorption spectroscopy. TEY-XANES of the PM2.5 sample on insulating membrane filters can be successfully measured in BL10/NewSUBARU. Comparing to XANES of reference compounds, chemical state analysis of PM2.5 can be easily performed by the TEY-XANES measurements.

1. Introduction

We have recently developed a new method for total-electron-yield (TEY) measurements of insulating bulk samples [1, 2]. In this method, insulating film samples, whose thickness is less than 100 μm , are put on conductive substrates. Sample current of the film samples can be sufficiently detected through the substrate, during soft X-ray irradiation onto the samples. Such the TEY method enables to easily measure X-ray absorption near-edge structure (XANES) of insulating materials.

To utilize this method for chemical analysis of insulating materials, we have measured XANES of particulate matter (PM) 2.5 collected on insulating membrane filters.

2. Experiments

Figure 1 shows membrane filters (blank) and PM2.5 collected on the filters. The PM2.5 samples were collected at the Hyogo Prefectural Environmental Research Center in Kobe on June, 2017. Two kinds of commercially available membrane filters were used; one is PM 2.5 air monitoring PTFE membrane filter (Whatman) labeled as WFT and another is KFT-730 (Kimoto Electric) labeled as KFT. PM2.5 were collected with high concentration (labeled as HPM) and with medium concentration (MPM) on each membrane filter. Thus, PM2.5 samples are labelled as HPM/WFT, MPM/WFT, HPM/KFT, and MPM/KFT. The filter samples were cut into 5 mm square and held on a conductive carbon tape on an aluminum sample plate. Sample current was measured through the carbon tape.

TEY X-ray absorption measurements in CK, OK and 200 ~ 600 eV regions of the PM2.5 samples were performed in the analysis chamber at BL10/NewSUBARU [3]. Incident soft X-ray

intensity (I_0) was monitored with sample current of a clean gold (Au) plate. Then, TEY can be obtained as the sample current (I) divided with I_0 .

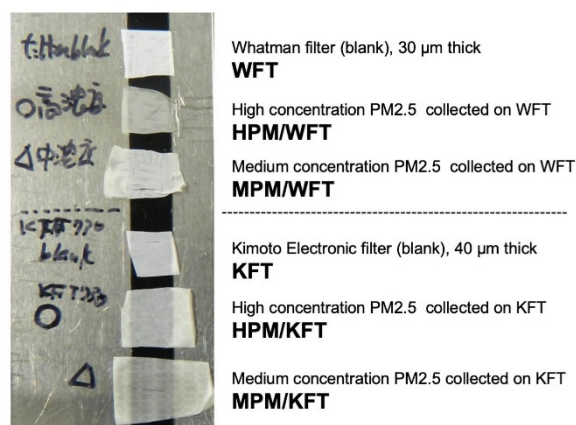


Fig. 1 Photo and specifications of the PM2.5 samples on membrane filters.

3. Results and Discussion

Figure 2 shows sample current spectra of the blank filters and PM2.5 samples. Although the measured sample current was less than 8 pA in 200 ~ 600 eV, absorption peaks can be clearly observed in CK and OK edges. Figure 3 shows the TEY X-ray absorption spectra (XAS) in the 200 ~ 600 eV region of the samples and the subtracted spectra, (PM2.5/filter) - (blank filter). The subtracted spectra show the spectra of PM2.5. Each subtracted spectrum clearly shows intense CK and OK peaks, and small NK peaks. This means that PM2.5 mainly consists of carbon and oxygen with small nitrogen.

Figure 4 shows the TEY CK-XANES of the samples and the subtracted spectra, (PM2.5/filter) - (blank filter). Although blank filters (WFT and KFT) exhibit no π^* peak,

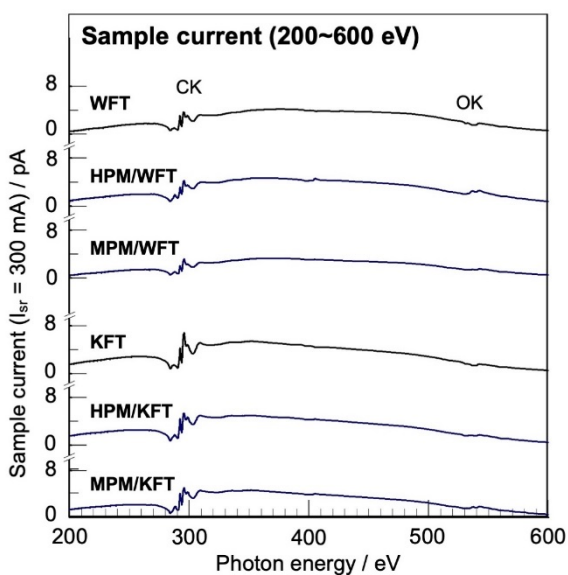


Fig. 2 Sample current spectra in the 200 ~ 600 eV region of blank filters and PM2.5 samples.

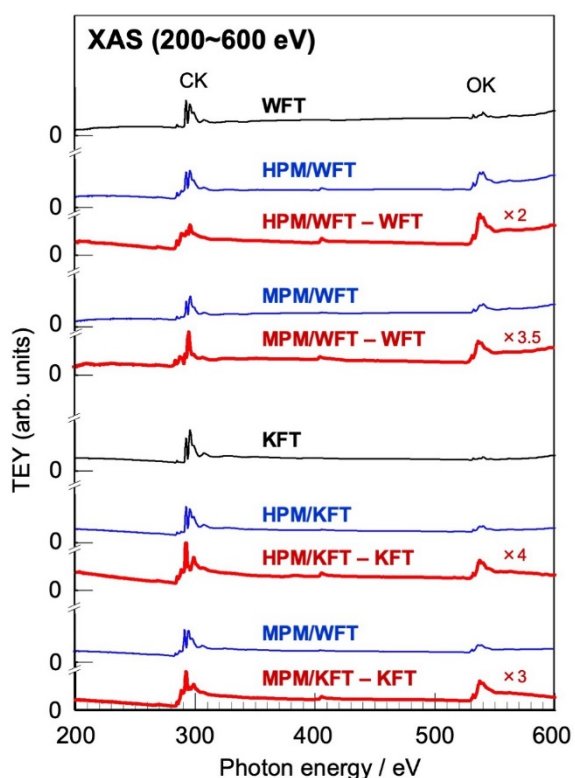


Fig. 3 TEY-XAS in the 200~600 eV region of blank filters and PM2.5 samples. Subtracted spectra, (PM2.5 sample) - (blank filter) are also described.

PM2.5/filter samples exhibit π^* peak near 285 eV and peak near 289 eV. Subtracted spectra which should be the CK-XANES of PM2.5 clearly show the π^* peak and 289 eV-peak. The π^* peak can be assigned to sp^2 carbons forming C=C bond in aromatic or unsaturated aliphatic structures.

The 289 eV-peak can be assigned to sp^3 carbons forming C-C structures. It is therefore confirmed that PM2.5 consists of sp^2 carbon and sp^3 carbons. Figure 4 also shows that the subtraction, PM2.5/filter - filter, easily provides XANES of PM2.5.

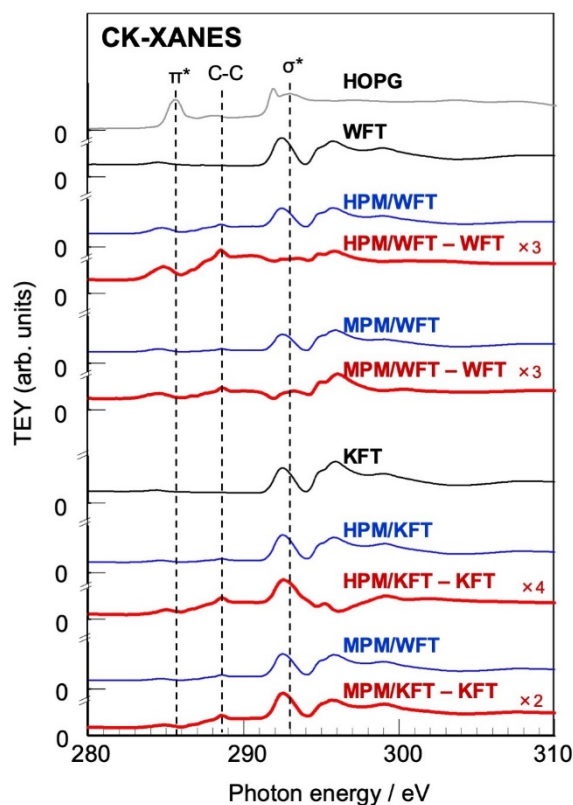


Fig. 4 TEY CK-XANES of blank filters and PM2.5 samples. Subtracted spectra, (PM2.5 sample) - (blank filter) are also described.

4. Conclusion

Soft X-ray absorption spectra of PM2.5 have been successfully and directly measured by using a TEY method. Subtracted spectra of (PM2.5/filter) - (blank filter) provide soft X-ray spectra of PM2.5. The proposed method would be a powerful tool for chemical analysis of atmospheric environmental particles.

5. Reference

- [1] Y. Muramatsu, The 76th Annual Meeting of Analytical Chemistry, Japan, F1010 (2016).
- [2] Y. Muramatsu, Y. Tani, Y. Tobita, S. Hamanaka, and E. M. Gullikson, Adv. X-Ray Chem. Anal. Japan, 49, 219-230 (2018).
- [3] Y. Muramatsu, A. Tsueda, T. Uemura, K. Nambu, T. Ouchi, T. Harada, T. Watanabe, and H. Kinoshita, LASTI Annual Report, 17, 29-30 (2015).

Soft X-ray spectroscopy of coal tars

Kosuke Shirai and Yasuji Muramatsu
Graduate School of Engineering, University of Hyogo

Abstract

XANES in the CK, NK, and OK regions of industrial coal tar samples were measured BL10/NewSUBARU for chemical analysis and structural identification. From the correlation between the height and width of π^* peak in C K-XANES (*i.e.* π^* peak map), it can be suggested that coal tar is aggregates of aromatic molecules whose ratio of edge carbon atoms is approximately 2/3 of the total carbon. It is also confirmed that the π^* peak map is useful for identification of coal tar.

1. Introduction

Coal tar is considered to be aggregates of polycyclic aromatic hydrocarbons (PAHs) from chromatography analysis. However, a novel characterization technique for coal tar has been required in industry, because coal tar takes too complicated structure to easily identify its molecular structure.

Soft X-ray absorption spectroscopy (XAS) using synchrotron radiation has been a powerful tool for characterization of carbon materials. We have recently found that relationship between the width and height of π^* peak (named as “ π^* peak map”) in CK-XANES provide local structure information of graphitic carbon materials [1].

In this study, to identify local structure of coal tar using soft X-ray absorption spectroscopy, we have measured soft X-ray absorption spectra of various industrial coal tar samples and apply the π^* peak map to coal tar for identification.

2. Experiments

Industrial coal tar samples were supplied from Japanese chemical company. The six samples are labelled as T1 ~ T6. Samples of T1 ~ T4 were thin films; T1 ~ T4 were dissolved in organic solvents and put onto a gold (Au) substrates. Samples of T5 and T6 were powders. The powders were pressed and held on an indium (In) substrates. Highly oriented pyrolytic graphite (HOPG) and carbon black (CB, N660) were used as references.

Soft X-ray absorption measurements were performed in BL10/NewSUBARU [2] using a total-electron-yield (TEY) method.

3. Result and Discussion

Figure 1 shows TEY-XAS spectra in the 200 ~ 600 eV region of coal tar samples. Each coal tar sample exhibits mainly CK peak and small NK and OK peaks. This means that coal tar consisting mainly of carbon includes small

amount of nitrogen and oxygen. It is also confirmed that the minor portion of nitrogen and oxygen can be detected by the TEY method.

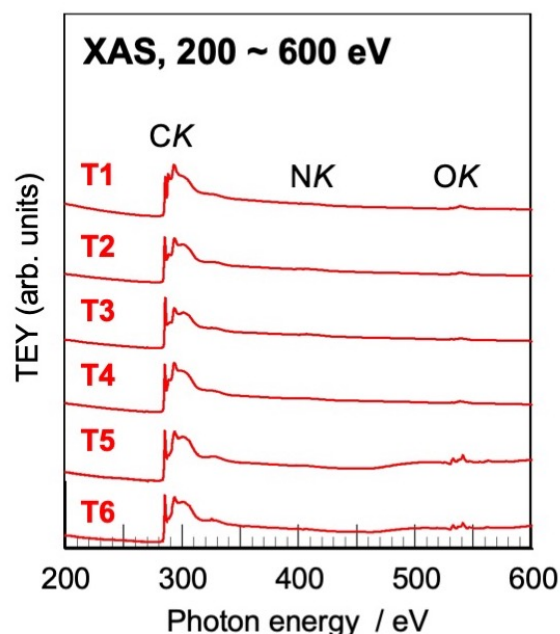


Fig. 1 TEY-XAS in the 200 – 600 eV region of coal tar samples.

Figure 2 shows the CK-XANES of coal tar samples with the reference HOPG and CB. Subtracted spectra of (coal tar) - (HOPG) are also described on XANES. XANES profiles of coal tar exhibit wider π^* peak profile than that of HOPG. Such the wider portions in π^* peak of coal tar can be clearly shown as the peaks near 284.5 eV in the subtracted spectra. The 284.5 eV-peak is labelled as peak *a*. This findings of wider π^* peak profile suggests that the edge carbon atoms of PAH in coal tar can be detected. T1 exhibits peak near 288 eV. This suggests that

T1 has alkyl C-C structures consisting sp^3 carbon atoms.

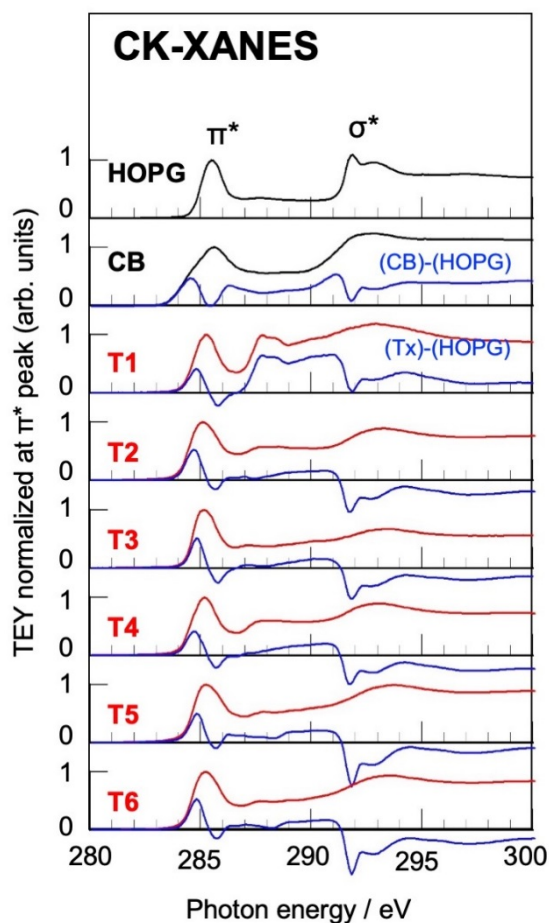


Fig. 2 CK-XANES of coal tar samples with the reference highly HOPG and carbon black (CB). Subtracted spectra of (CB) –(HOPG) and (Coal tar samples) – (HOPG) are described on each XANES.

Figure 3 shows the π^* peak map of coal tar samples (T1 ~ T6) with the nano-graphite [1], carbon black, and various PAHs. Coal tar samples distribute in two groups on the π^* peak map; One is T1 on the line of nano-graphite, another is T2 ~ T6 on the areas of middle peak a height and higher π^* peak height. Such the distribution suggests that T1 take larger hexagonal carbon layer structures similar to carbon black and that T2 ~ T6 are basically PAH molecules. Compared to the distributions of PAH molecules, T2 ~ T6 distributes near the PAHs in which ratio of hydrogen-terminated edge carbon atoms in molecules is approximately $2/3$. This means that the coal tar samples should mainly consist of such the PAH structures.

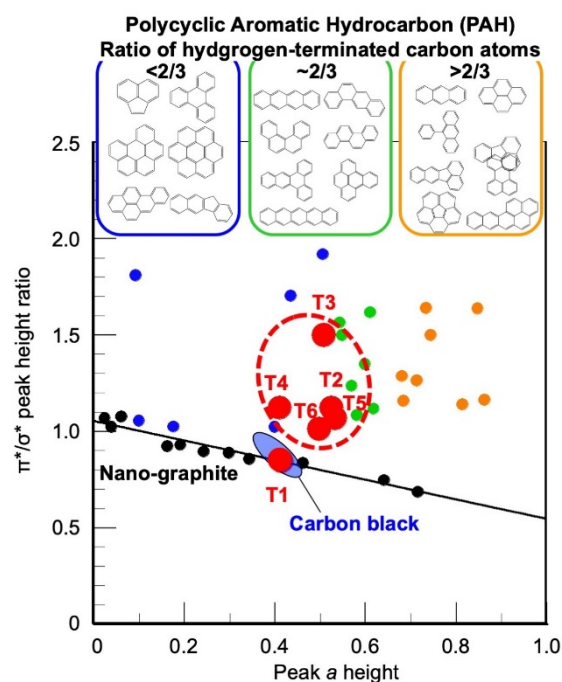


Fig. 3 The π^* peak map of coal tar samples with nano-graphite, carbon black, and various polycyclic aromatic hydrocarbons.

In conclusion, it can be elucidated that the π^* peak map obtained from the CK-XANES is useful for structural identification of coal tar.

References

- [1] Y. Muramatsu, K. Murayama, and T. Okada, Proceedings of the 10th International Symposium on Atomic Level Characterizations for New Materials and Devices '15, ALC'15, 27p-P-38 (2015).
- [2] Y. Muramatsu, A. Tsueda, T. Uemura, K. Nambu, T. Ouchi, T. Harada, T. Watanabe, and H. Kinoshita, LASTI Annual Report, 17, 29-30 (2015).

Controllability of copper particle synthesized by X-ray radiolysis using synchrotron radiation

Akinobu Yamaguchi¹, Ikuo Okada², Ikuya Sakurai², Takao Fukuoka¹, and Yuichi Utsumi¹

¹Laboratory of Advanced Science and Technology, University of Hyogo

²Synchrotron Radiation Research Center, Nagoya University

Abstract

We demonstrate the synthesis and immobilization of caltrop-shaped cupric particles from the $\text{Cu}(\text{CH}_3\text{COO})_2$ solution with an additive alcohol by X-ray radiolysis using synchrotron radiation. The particles could be synthesized in the X-ray radiolysis of aqueous solutions of $\text{Cu}(\text{CH}_3\text{COO})_2$, which also contain methanol, ethanol, 1-propanol, 2-propanol. We found the alkyl alcohol whose chain length is longer than four cannot synthesize any particles. The alcohol solubility plays a significant role in nucleation and synthesis. Our study may shed light on understanding a photochemical reaction route induced under the X-ray irradiation.

Introduction

Conventional chemical synthesis of inorganic materials has been developed for many applications such as catalysis, medicine, electronics, ceramics, cosmetics, and bio/molecular-sensing using surface enhanced Raman scattering (SERS). Recently, a lot nanoparticles and nanostructures, such as nanowires, nanorods, nanoribbons, nanobelt, and nano-flower have been synthesized by various techniques.

The photochemical reaction has a possibility to achieve a novel three dimensional (3D) printing and additive manufacturing process because of its easy and intriguing applicability and engineering applications. There are many techniques which can fabricate 3D structures made of plastic or metallic materials. However, there are few techniques which can create a structure consisting of composite materials such as metallic, plastic, and oxidized materials, etc. The photochemical reaction might be one of the candidates which can fabricate the 3D structure consisting of composite materials.

Here, we demonstrated the synthesis of nano/micro-scale metallic, oxidized and their clusters deposited onto a substrate by the X-ray radiolysis-induced photochemical reaction using Synchrotron Radiation (SR) facility. The advantage of performing X-ray radiolysis-induced photochemical reaction using SR is its atomic level of processing accuracy; fine control; deep lithography and so on. Several groups also reported the synthesis of nano/micro-scale particles by monochromatic X-ray irradiation. [1, 2]

In this study, we have noticed that the additive ethanol plays a significant role in the reduction and synthesis of particles directly from the solution by X-ray radiolysis-induced

photochemical reaction. Therefore, we investigate the alkyl chain length dependence of synthesis to understand the mechanism of particle nucleation, ripening, and aggregation to obtain the deeper understanding of contributions of alcohols.

Experiments

The stock solution was made by dissolving 6.8 g of $\text{Cu}(\text{CH}_3\text{COO})_2$ (Wako Chemical, 99.99%) in 100 mL of doubly distilled water. We syphoned off 200 μL of the solution into a microtube and added 10 μL alkyl alcohols from methanol (R-1) to 1-decanol (R-10), and 2-propanol (R-2') to obtain the mixed solution. An 18 μL aliquot of the mixed solution was then exposed to X-ray irradiation as schematically shown in Fig. 1. In this study, a silicon substrate was dipped into the mixed solution and the specimen was placed on the irradiation system. The specimen was exposed to 5 minute X-rays and then washed using deionized water. The synthesized particles deposited on the silicon substrate were examined by field emission scanning electron microscopy with energy

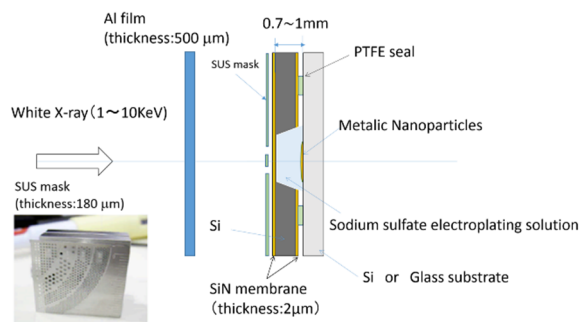


Fig. 1 Experimental setup for the X-ray irradiation of the $\text{Cu}(\text{CH}_3\text{COO})_2$ solution including alkyl alcohol.

dispersive X-ray spectroscopy (EDX). In addition, we obtained Raman spectra using a micro-Raman spectrometer to determine the material characteristics of the synthesized particles.

Results and discussion

No particles were synthesized when the silicon substrate was immersed in an aqueous $\text{Cu}(\text{CH}_3\text{COO})_2$ solution including of no additive and the following alkyl alcohols from 1-butanol to 1-decanol. We also found no particles were synthesized when the acetone and acetic acid were added into the solution. As a result, we reveal that there is an upper limit of a chain length of alkyl alcohol to synthesize the particles in aqueous solution to be 3.

Figures 2 and 3 show typical SEM image and EDX analyses of particles synthesized when the ethanol and 1-propanol were added into the solution, respectively. We found that these synthesized particles are copper oxide materials.

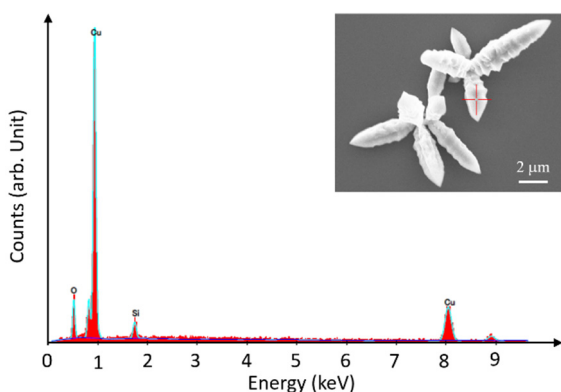


Fig. 2 SEM image and EDX analyses of particles synthesized by the 5 min. X-ray radiolysis-induced photochemical reaction of the $\text{Cu}(\text{CH}_3\text{COO})_2$ solution including ethanol.

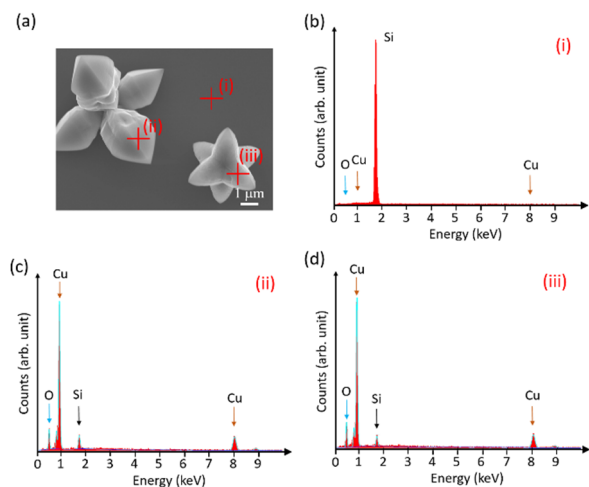


Fig. 3 (a) SEM image and (b) – (d) EDX analyses of (i) substrate and (ii) (iii) particles synthesized by the 5 min. X-ray radiolysis-induced photochemical reaction of the $\text{Cu}(\text{CH}_3\text{COO})_2$ solution including 1-propanol.

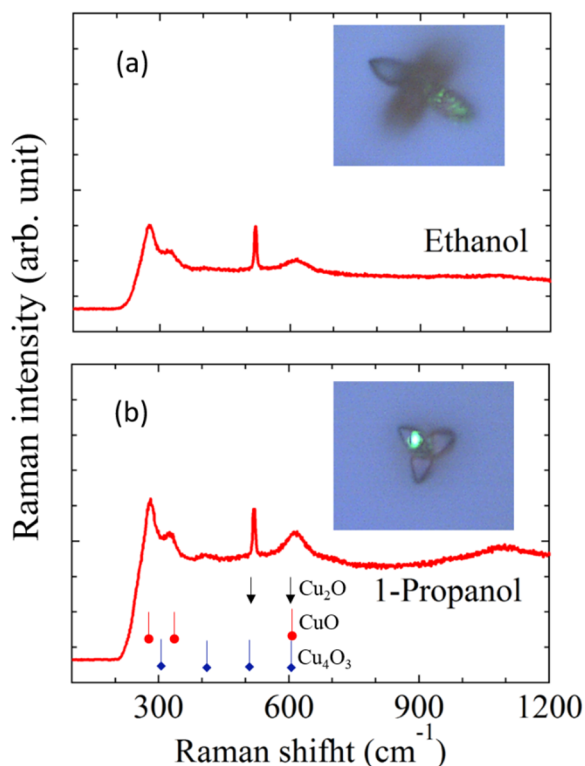


Fig. 4 Micro-laser Raman spectra of the particles synthesized by the X-ray irradiation of aqueous $\text{Cu}(\text{CH}_3\text{COO})_2$ solution including (a) ethanol and (b) 1-propanol, respectively. The insets are optical micrographs of the particles; the position of the green light corresponds to the measurement position of the laser.

We show micro-laser Raman spectra to determine the composition of the synthesized particles as shown in Fig. 4. There are three candidates of copper oxides, CuO , Cu_2O and Cu_4O_3 . Peaks at 283 , 333 , and 622 cm^{-1} are deduced to be Raman signals from Ag and Bg modes of cupric oxide CuO .

Conclusion

Our study demonstrates the synthesis of copper oxide particles deposited onto a Si substrate under the X-ray radiolysis-induced photochemical reaction. This work also leads to additive alcohol chain number dependence of synthesizing particles. This method can also provide novel lithography process.

References

- [1] R. A. Rosenberg *et al.*, *J. Vac. Sci. Technol. B* **16**, 3535 (1998); Q. Ma *et al.*, *Appl. Phys. Lett.* **76**, 2014 (2000).
- [2] A. Yamaguchi *et al.*, *Mater. Chem. Phys.* **160**, 205 (2015); *Jpn. J. Appl. Phys.* **55**, 055502 (2016); *J. Nanometer.* 8584304 (2016); *J. Synchrotron Radiation* **24**, 653 (2017); *J. Synchrotron Radiation* to be published.

Deposition of Polytetrafluoroethylene Film via Synchrotron Radiation

Masaya Takeuchi, Akinobu Yamaguchi, Yuichi Utsumi
Laboratory and Advanced Science and Technology for Industry, University of Hyogo

Abstract

A novel process was developed for fabricating a polytetrafluoroethylene (PTFE) thin film using synchrotron radiation (SR). First, a PTFE substrate was exposed to high-energy X-rays (2–8 keV) at room temperature. Afterwards, the PTFE substrate (target) was heated under atmospheric pressure and fragments desorbed from the surface deposited on a glass substrate to produce a film with a thickness of above 10 μm . The characterization of the chemical structure of the deposited film was carried out using X-ray diffraction (XRD). The results indicated that the crystalline structure of the film became closer to those of the PTFE substrate upon an increase in the X-ray irradiation of the sample. The fabrication process of this PTFE thin film could be applied to various fields because surface modification of the substrate can be easily carried out.

Introduction

Compared with other polymers, polytetrafluoroethylene (PTFE) has high heat resistance, excellent chemical stability, electrical insulation and low friction. Due to these outstanding properties, it is used in various applications, such as piping tube, packing in chemical plants, and cable coating. Also, thin films of PTFE are required for certain applications, such as proton exchange membranes [1] and membranes for desalination [2].

Several methods have been reported for fabricating thin films of PTFE, such as thermolysis [3], ion-beam sputtering [4], laser ablation [5-7], and synchrotron radiation (SR) [8-10]. These are performed by depositing fragments derived from PTFE on a substrate. Films deposited via SR can be specially fabricated with a high deposition rate, with compositions and crystalline features similar to those of the PTFE substrate. The method can be performed by etching has been proposed [12,13], which is carried out by heating an X-ray irradiated PTFE substrate. An etching depth of 1 mm can be obtained using this method.

In this study, a novel process was developed for fabricating a PTFE thin film using SR. First, a PTFE substrate was subjected to high-energy X-rays (2–8 keV) at room temperature. Afterwards, the substrate (PTFE target) was heated under atmospheric pressure and fragments desorbed from the surface deposited on a glass substrate. As previously mentioned, high-energy X-ray photons can penetrate more deeply in the PTFE substrate to induce chain scission. Therefore, more fragments, which desorbed from the surface upon the heating of the PTFE target,

are generated, significantly increasing the number of molecules that can form a deposited film. The chemical structure of the film were then evaluated using X-ray diffraction (XRD).

Experiments and Results

PTFE thin films were prepared via the SR irradiation of PTFE substrates. The exposure was carried out on beamline BL-11 [14] of the NewSUBARU SR facility at the University of Hyogo, Japan. The storage ring electron energy was set at 1.5 GeV. Figure 1 (a) shows the calculated spectrum of the X-ray beam at the exposure stage, which is continuous from 2–8 keV with a peak photon energy of 4.5 keV. Figure 1 (b) shows the photon energy dependence of the transmittance through PTFE substrates with various thicknesses of 10, 20, 50, 100, and 300 μm . X-rays with higher photon energy are able to penetrate deeper into the film, causing scission of the main chain C–C bonds, induced from the PTFE surface to a depth of around 300 μm via X-ray irradiation on beamline BL-11.

A commercially available PTFE substrate (UNIVERSAL Co., Ltd., 00I-251-02) was used to prepare the PTFE target with a thickness of 1.5 mm, which is enough to suppress the distortion of the substrate caused by heating during the deposition. The PTFE substrate was placed perpendicular to the incident X-ray beam in the exposure chamber of beamline BL-11 and vertically scanned at a scanning rate of 5 mm/s. The X-ray irradiation dose was controlled by changing the number of scans. Here helium (He) gas was introduced into the exposure chamber to suppress the temperature rise of the PTFE substrate and evaporation of the depolymerized

PTFE molecules during X-ray irradiation. The PTFE target was heated under atmospheric pressure on a hot plate for 1 hour and the fragments desorbed from the substrate surface were deposited onto a glass substrate. The air-gap distance between the PTFE target and the glass substrate was 3 mm. The PTFE target was used to prepare deposited films using X-ray doses of 1.7, 3.0, and 4.3 J/mm². The thicknesses of the deposited films were measured using a laser microscope and 6.6, 8.1, and 11.9 μm at 1.7, 3.0, and 4.3 J/mm².

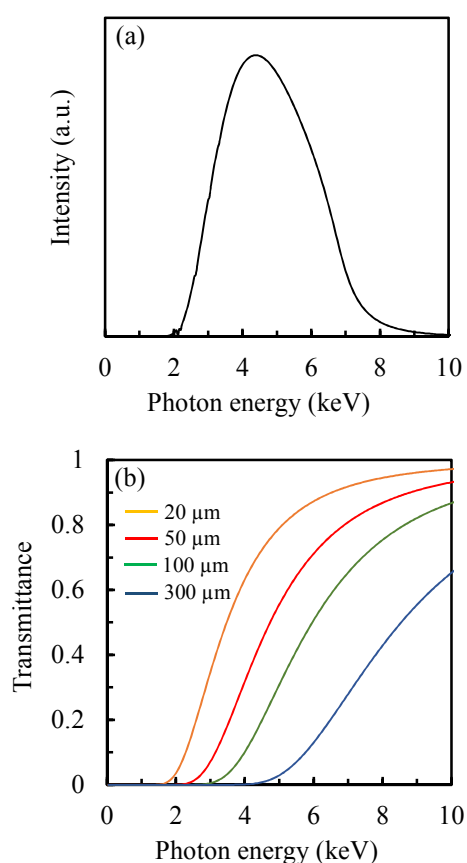


Fig. 1. (a) Calculated SR spectrum at 1.5 GeV recorded at the exposure stage on beamline BL-11. (b) Photon energy dependence of X-ray transmittance through PTFE substrates with various thicknesses of 20, 50, 100, and 300 μm.

The crystalline structures of the deposited films on glass substrates were measured by XRD using a Rigaku-D/tex Ultra 250 equipped with a CuK α radiation source ($\lambda = 1.5406 \text{ \AA}$). The XRD spectrum of a 0.1 mm thick pristine PTFE substrate without SR irradiation is shown in Fig. 2 (a). Diffraction peaks derived from amorphous and crystalline material were observed at $2\theta = 16$ and 18° , respectively, which correspond with previously reported values [9,12]. Figure 2 (b) shows the XRD spectra of the

deposited films fabricated using the PTFE target with various X-ray doses. Peaks were observed at $2\theta = 16$ and 18° at X-ray doses of 3.0 and 4.3 J/mm², similar to those observed for pristine PTFE. This result indicates that the crystalline structure of the deposited film is similar to that of PTFE at these X-ray doses.

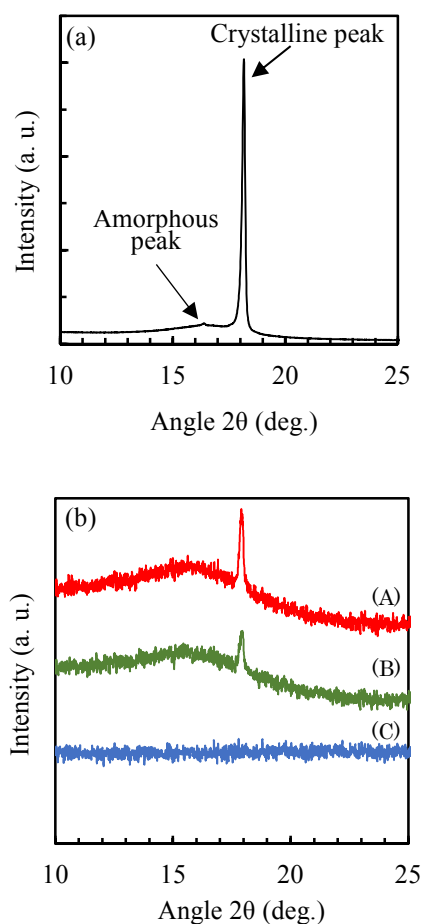


Fig. 2. XRD spectrum of (a) 0.1 mm thick PTFE and (b) the deposited film fabricated using the PTFE target with X-ray irradiation doses of (A) 4.3, (B) 3.0, (C) 1.7 J/mm².

Conclusion

In this study, a novel deposition process was developed to fabricate a thin PTFE film using high-energy X-rays from 2–8 keV. A PTFE substrate was irradiated using X-rays and the deposition was carried out under atmosphere pressure by heating the PTFE target and depositing the fragments desorbed from the surface onto a glass substrate. Using this method, a thin film with a thickness of above 10 μm was achieved. The crystalline structures of the deposited films were evaluated using XRD. The XRD data of the samples were compared with those of the pristine PTFE substrate and it was

found that the crystalline structures of the sample films are similar to those of the pristine PTFE substrate. The technique used in this study to fabricate PTFE thin films can be easily used to perform surface modification and can be applied to various applications.

References

- [1] F. Liu, B. Yi, D. Xing, J. Yu, and H. Zhang, *J. Memb. Sci.*, **212**, pp.213-223 (2003).
- [2] H. Zhu, H. Wang, F. Wang, Y. Guo, H. Zhang, and J. Chen, *J. Memb. Sci.*, **446**, pp.145-153 (2013).
- [3] T. C. Nason, J. A. Moore, and T.-M. Lu, *Appl. Phys. Lett.*, **60**, pp/1866-1868 (1992).
- [4] F. Quaranta and A. Valentini, *Appl. Phys. Lett.*, **63**, pp.10-11 (1993).
- [5] S. G. Hansen and T. E. Robitaille, *Appl. Phys. Lett.*, **52**, pp.81-83 (1988).
- [6] G. B. Blanchet and S. I. Shah, *Appl. Phys. Lett.*, **62**, pp.1026-1028 (1993).
- [7] Y. Ueno, T. Fujii, and F. Kannari, *Appl. Phys. Lett.*, **65**, pp.1370-1372 (1994).
- [8] M. Inayoshi, M. Ikeda, M. Hori, T. Goto, M. Hiramatsu, and A. Hiraya, *Jpn. J. Appl. Phys.*, **34**, pp.L1675-L1677 (1995).
- [9] T. Katoh and Y. Zhang, *Appl. Phys. Lett.*, **68**, pp.865-867 (1996).
- [10] M. Inayoshi, M. Ito, M. Hori, and T. Goto, *J. Vac. Sci. Technol. B*, **17**, pp.949-956 (1999).
- [11] Y. Ukita, M. Kishihara, K. Kanda, S. Matsui, K. Mochiji, and Y. Utsumi, *Jpn. J. Appl. Phys.*, **47**, pp.337-341 (2008).
- [12] A. Yamaguchi, H. Kido, Y. Ukita, M. Kishihara, and Y. Utsumi, *Appl. Phys. Lett.*, **108**, pp.051610-1-051610-5 (2016).
- [13] A. Yamaguchi, H. Kido, and Y. Utsumi, *J. Photopolym. Sci. Technol.*, **29**, pp.403-407 (2016).
- [14] M. Takeuchi, A. Yamaguchi, and Y. Utsumi, *J. Synchrotron. Rad.*, **26**, pp.528-534 (2019).

Modification of optical property of a Polytetrafluoroethylene by Synchrotron Radiation

Masaya Takeuchi, Akinobu Yamaguchi, Yuichi Utsumi
Laboratory and Advanced Science and Technology for Industry, University of Hyogo

Abstract

We demonstrate the modification of transmittance of bulk polytetrafluoroethylene (PTFE) via synchrotron X-ray irradiation. X-ray irradiation of the PTFE substrate is conducted to mechanically suppress the photoevaporation of PTFE molecules. This method drastically increases the ultraviolet and visible transmittance of the irradiated areas of the substrates, with greater than 80% transmittance observed at the 350-nm wavelength. We observed the irradiated area via scanning electron microscopy and determined that this optical property modification is due to the homogenization of the bulk PTFE texture with nanometer to micron-sized pores. We expect that this modified PTFE will be employed as a construction material for various micro system devices such as Lab-on-a-chip and micro total analysis systems.

Introduction

Polytetrafluoroethylene (PTFE) has excellent material properties, such as high heat and chemical resistance, high mechanical strength, electrical insulation, a low dielectric constant, and low coefficient of friction. These ideal characteristics make PTFE an attractive material for microsystems such as micro-electro mechanical systems (MEMS), micro total analysis systems (μ TAS), and Lab-on-a-chip (LOC). However, PTFE microfabrication and its bulk modification are difficult owing to the outstanding thermal and chemical stability of PTFE, with most PTFE research conducted using either x - γ , α , electron beam (EB), or neutron radiation to date [1–17].

The direct etching of PTFE induced by synchrotron radiation (SR) irradiation [1–3] and the precise process characteristics of PTFE etching using a high-energy (2–12 keV) X-ray and heat assistance have been studied extensively [4–7]. For example, tentative bubble-like structures were observed on the X-ray irradiated surface of PTFE substrates via scanning electron microscopy (SEM), and the results indicated that surface liquefaction occurred during the photolysis of bulk PTFE, with the desorption of photoproducts from the surface and subsequent degradation of the PTFE molecules [4–6]. Raman spectroscopy and X-ray diffraction measurements of the X-ray irradiated PTFE surfaces suggested that the chain scissions of PTFE were driven to completion [7], with confirmation that the melting temperature of the irradiated PTFE decreased because the molecular weight decreased owing to the chain scission of PTFE via X-ray irradiation, resulting in the evaporation of photoproducts from the surface.

Furthermore, it has been reported that the modification of the optical properties of PTFE results in the transformation of the original opaque PTFE substrates into transparent PTFE substrates after several MeV of EB irradiation while in the molten state [9].

Here we report on the optical modification of bulk PTFE by suppressing the evaporation of the photoproducts generated via X-ray irradiation on the PTFE substrate, which drastically increases its ultraviolet (UV) and visible transmittance.

Experiments and Results

The SR irradiation experiment on the PTFE substrates was conducted at beam line BL-11 [18] of the NewSUBARU SR facility at the University of Hyogo, Japan. The storage ring electron kinetic energy was set at 1.5 GeV, with a storage ring current of 160–320 mA. Each PTFE substrate (500- μ m thickness) was enclosed in a 12- μ m-thick Al film barrier layer. The sample heating was adjusted to maintain an incident SR beam that was perpendicular to the PTFE surface in the reaction chamber, and the PTFE surface was vertically scanned to ensure a homogeneous intensity distribution, which was performed by moving the exposure stage. The SR irradiation dose was controlled by changing the number of scans. The X-ray irradiation was conducted with heating in a vacuum. The dashed line of Fig. 1 shows the calculated spectrum in BL-11. The line is obtained by the 1.5 GeV operation with a storage ring current of 300 mA. The solid line of Fig. 1 shows the spectrum of the beam adding the transmission of the Al film barrier layer of PTFE substrate to the above spectrum. The photon energy of the X-ray irradiated PTFE substrates

spans the 3–8 keV range. Additionally, the UV and visible transmittance of the irradiated area of the substrates were measured using a spectrophotometer.

We performed X-ray irradiation of the PTFE substrates under 4 ± 2 Pa pressure and a heating temperature of 200 °C. The SR doses were 0, 13, 23, 26, and 33 J/cm² with the 1.5 GeV operation in BL-11. The transmittance increases with higher SR doses, as shown in Fig. 2, with more than 80% transmittance at the 350-nm wavelength and SR dose of 33 J/mm².

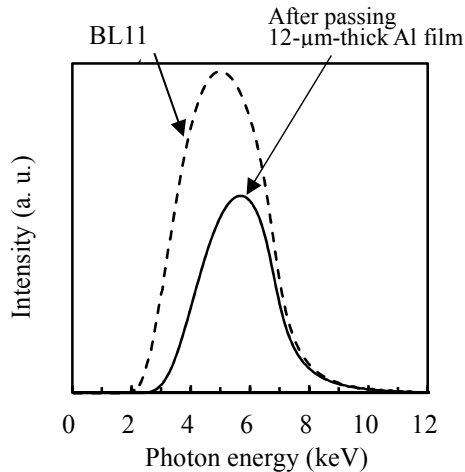


Fig. 1. Calculated photon intensity spectrum of the X-ray obtained from BL-11 at NewSUBARU (1.5 GeV operation; dashed line) and that after passing 12-μm-thick Al film (solid line).

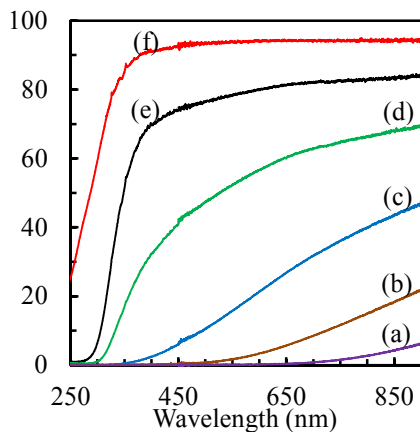


Fig. 2. Transmittance of the X-ray irradiated PTFE in the visible light region: (a) 0, (b) 13, (c) 23, (d) 25, (e) 26, (f) 33 J/mm².

Our results demonstrate that the drastic change in the transmittance of bulk PTFE via SR irradiation is attributed to the homogenization of the bulk PTFE substrate. Commercialized PTFE substrates generally possess a low UV and visible

transmittance owing to light scattering because they are produced via sintering as-polymerized powder, and their bulk morphology comprises a porous texture with nanometer to micron-sized pores [19]. However, it is confirmed that the PTFE melting point decreases via SR irradiation and allows the material from the irradiated area to infiltrate the pores in the non-irradiated area as the melting liquid; this leads the homogenization of the bulk PTFE texture. Figure 3 shows a SEM image of an SR-irradiated PTFE surface that suppressed the evaporation of photochemical products in BL-11, with an SR dose of 33 J/mm². As mentioned above, we confirmed that this optical property modification arose with the homogenization of bulk PTFE. Further, we assume that the degradation in the crystallinity of the PTFE bulk texture owing to SR irradiation is another contributing factor.

Conclusion

In this paper, we demonstrate that X-ray irradiation modifies bulk PTFE by mechanically SR-irradiated surface Original PTFE surface

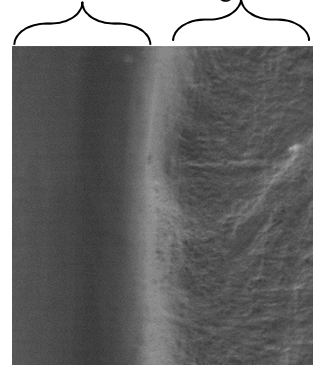


Fig. 3. SEM images of a PTFE surface irradiated in beam line BL-11 at NewSUBARU.

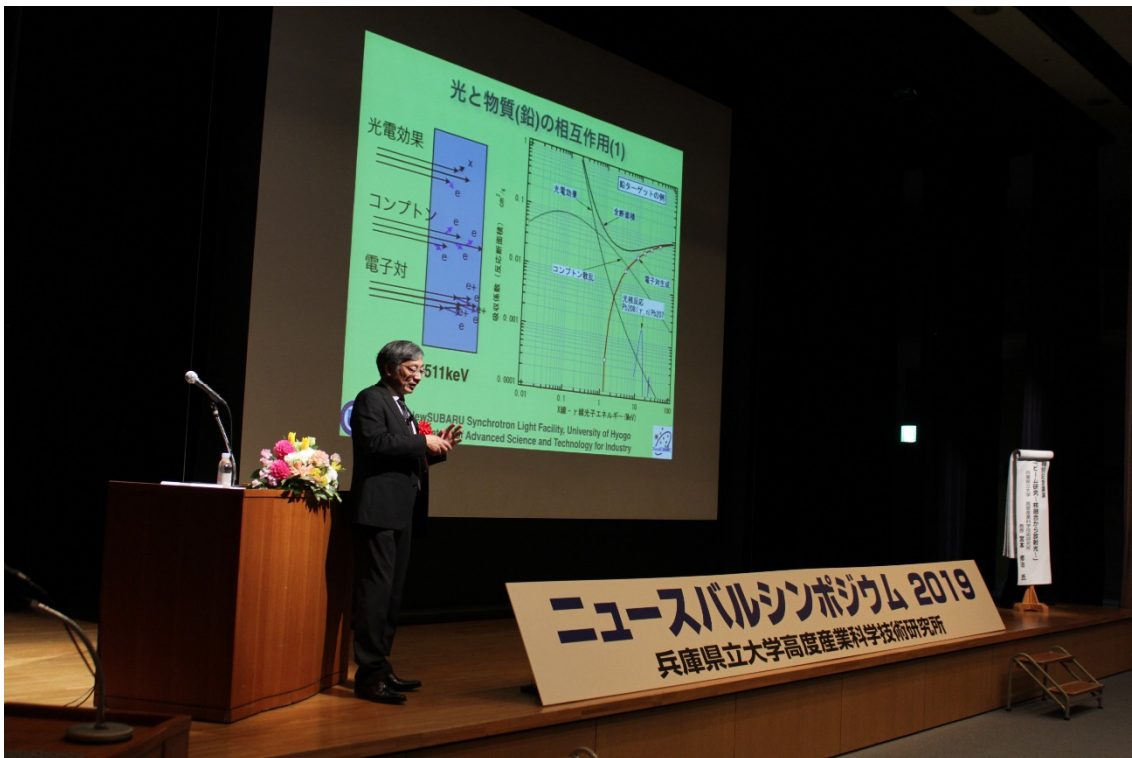
suppressing photoevaporation of the PTFE molecules and drastically increases the UV and visible transmittance of the PTFE molecules. We suggest that the modification of the transmittance of bulk PTFE is caused by the homogenization of bulk PTFE. It is expected that this modified PTFE will be employed as a construction material in various micro system devices, such as LOC and μTAS, for the observation of cells and chemiluminescent immunoassays to detect target substances in microliquids.

References

- [1] Y. Zhang, T. Katoh, M. Washio, H. Yamada, and S. Hamada, *Appl. Phys. Lett.*, **67**, pp.872-874 (1995).
- [2] Y. Zhang and T. Katoh, *Jpn. J. Appl. Phys.*, **35**, pp.L186-L188 (1996).

- [3] M. Inayoshi, M. Ikeda, M. Hori, T. Goto, M. Hiramatsu, and A. Hiraya, *Jpn. J. Appl. Phys.*, **34**, pp. L1675-L1677 (1995).
- [4] Y. Ukita, M. Kishihara, K. Kanda, S. Matsui, K. Mochiji, and Y. Utsumi, *Jpn. J. Appl. Phys.*, **47**, pp.337-341 (2008).
- [5] H. Kido, T. Kuroki, M. Okubo, and Y. Utsumi, *Microsyst. Technol.*, **19**, pp.301-307 (2013).
- [6] A. Yamaguchi, H. Kido, and Y. Utsumi, *J. Photopolym. Sci. Technol.*, **29**, pp.403-407 (2016).
- [7] A. Yamaguchi, H. Kido, Y. Ukita, M. Kishihara, and Y. Utsumi, *Appl. Phys. Lett.*, **108**, pp.051610-1-051610-5 (2016).
- [8] A. Oshima, Y. Tabata, H. Kudoh, and T. Seguchi, *Radiat. Phys. Chem.*, **45**, pp.269-273 (1995).
- [9] A. Oshima, S. Ikeda, T. Seguchi, and Y. Tabata, *Radiat. Phys. Chem.*, **49**, pp.279-284 (1997).
- [10] A. Oshima, S. Ikeda, H. Kudoh, T. Seguchi, and Y. Tabata, *Radiat. Phys. Chem.*, **50**, pp.611-615 (1997).
- [11] U. Lappan, U. Geißler, and K. Lunkwitz, *J. Appl. Polym. Sci.*, **74**, pp.1571-1576 (1999).
- [12] U. Lappan, U. Geißler, and K. Lunkwitz, *Radiat. Phys. Chem.*, **59**, pp.317-322 (2000).
- [13] U. Lappan, U. Geißler, L. Häußler, D. Jehnichen, G. Pompe, and K. Lunkwitz, *Nucl. Instrum. Methods Phys. Res. B*, **185**, pp.178-183 (2001).
- [14] O. K. Harling, G. E. Kohse, and K. J. Riley, *J. Nucl. Mater.*, **304**, pp.83-85 (2002).
- [15] D. L. Pugmire, C. J. Wetteland, W. S. Duncan, R. E. Lakis, and D. S. Schwartz, *Polym. Degrad. Stab.*, **94**, pp.1533-1541 (2009).
- [16] A. M. S. Galante, O. L. Galante, and L. L. Campos, *Nucl. Instrum. Methods Phys. Res. B*, **619**, pp.177-180 (2010).
- [17] Y. Tabata, H. Suzuki, and S. Ikeda, *Radiat. Phys. Chem.*, **84**, pp.14-19 (2013).
- [18] M. Takeuchi, A. Yamaguchi, and Y. Utsumi, *J. Synchrotron. Rad.*, **26**, pp.528-534 (2019).
- [19] S. A. Khatipov, S. A. Serov, N. V. Sadovskaya, and E. M. Konova, *Radiat. Phys. Chem.*, **81**, pp.256-263 (2012).

Part 3. List of Publications



Retirement memorial lecture of Prof. Shuji Miyamoto

List of publications

(1) Papers

1. **"Performance measurement of HARPO: A time projection chamber as a gamma-ray telescope and polarimeter"**
P. Gros, S. Amano, D. Attié, P. Baron, D. Baudin, D. Bernard, P. Bruel, D. Calvet, P. Colas, S. Daté, A. Delbart, M. Frotin, Y. Geerebaert, B. Giebels, D. Götz, S. Hashimoto, D. Horan, T. Kotaka, M. Louzir, F. Magniette, Y. Minamiyama, S. Miyamoto, H. Ohkuma, P. Poilleux, I. Semeniouk, P. Sizun, A. Takemoto, M. Yamaguchi, R. Yonamine, S. Wang
Astroparticle Physics, 97, pp.10-18 (2018).
2. **"Development of positron annihilation measurement system with fast positron created by laser Compton scattering γ -ray at NewSUBARU synchrotron facility"**
Fuminobu Hori, Kento Sugita, Akihiro Iwase, Mititaka Terasawa, Shuji Miyamoto
日本陽電子科学会「陽電子科学」第10号, ISSN 2188-0107 pp.21-28(2018).
3. **"Photon-flux determination by the Poisson-fitting technique with quenching corrections"**
H.Utsunomiya, T. Watanabe, T. Ari-izumi Daiki Takenaka, T. Araki, K. Tsuji, I. Gheorghe, D. M. Filipescu, S. Belyshev, K. Stopani, D. Symochko, H. Wang, G. Fan, T. Renstrøm, G. M. Tveten, Y.-W. Lui, K. Sugita, S.Miyamoto
Nuclear Instruments and Methods in Physics Research A, 896, pp.103-107 (2018).
4. **"Measurements of Neutrons from Photonuclear Reactions using Laser Compton Scattering Gamma rays"**
S. Miyamoto, A. Takemoto, M. Yamaguchi, K. Sugita, S. Hashimoto, S. Amano
Plasma and Fusion Research, 13, 2404066 (2018).
5. **"A Comprehensive Analysis of Polarized γ -ray Beam Data with the HARPO Demonstrator"**
R.Yonamine, S. Amano, D. Attié, P. Baron, D. Baudin, D. Bernard, P. Bruel, D. Calvet, P. Colas, S. Daté, A. Delbart, M. Frotin, Y. Geerebaert, B. Giebels, D. Götz, P. Gros, S. Hashimoto, D. Horan, T. Kotaka, M. Louzir, F. Magniette, Y. Minamiyama, S. Miyamoto, H. Ohkuma, P. Poilleux, I. Semeniouk, P. Sizun, A. Takemoto, M. Yamaguchi, and S. Wang
Proceedings of International Conference on Technology and Instrumentation in Particle Physics 2017, pp. 27-30 (2018).
6. **"Photoneutron cross sections for Ni isotopes: Toward understanding (n, gamma) cross sections relevant to the weak s-process nucleosynthesis"**
H. Utsunomiya, T. Renstrøm, G. M Tveten, S. Goriely, S. Katayama, T. Ari-izumi, D. Takenaka, D. Symochko, B. V. Kheswa, V.W. Ingeberg, T. Glodariu†, Y.-W. Lui, S. Miyamoto, A. C. Larsen, J. E. Midtbø, A. Görgen, S. Siem, L. Crespo Campo, M. Guttormsen, S. Hilaire, S. Péru, and A. J. Koning
Physical Review C, 98, 054619 (2018).
7. **"The γ -ray Strength Function for Thallium Isotopes relevant to the ^{205}Pb - ^{205}Tl Chronometry"**
H. Utsunomiya, T. Renstrøm, G. M Tveten, S. Goriely, T. Ari-izumi, D. Filipescu, I. Gheorghe, Y.-W. Lui, W. Luo, S. Miyamoto, A. C. Larsen, S. Hilaire, S. Péru, and A. J. Koning
Phys. Rev. C 99, 024609 (2019).
8. **"レーザーコンプトン散乱ガンマ線による高速陽電子を用いた材料欠陥検査システムの開発"**
杉田健人, 森本悠介, 橋本智, 天野壮, 堀 史説, 岩瀬彰宏, 寺澤倫孝, 宮本修治
日本物理学会第73回年次大会予稿集, 25aK606-4 (2018).
9. **" γ 線 Tracking 検出器の開発と性能評価"**
甲田 旭, 青井 考, 山本康嵩, 井手口栄治, MUKHI KUMAR RAJU, Hoang Thi Ha, Tung Thanh Pham, 嶋達志, 柳原陸斗, Viljamaa Topi Benjamin, 宮本修治, 静間俊行
日本物理学会第73回年次大会予稿集, 25aK302-10 (2018).
10. **"NewSUBARU BL01 ビームラインの整備と実験"**
宮本 修治

原子力学会春の年会(2018)予稿集, 放射線工学部会セッション, 2H_PL03
「レーザー逆コンプトン放射線場による放射線工学の新たな展開」

11. **"帯域可変ガンマ線分光器のための櫛歯結晶の設計と試作"**
羽島良一, 早川岳人, 静間俊行, 沢村勝, 永井良治, 宮本修治, 松葉俊哉
原子力学会春の年会(2018)予稿集, 2018.3.26-28 大阪大学吹田キャンパス.
12. **"巨大共鳴領域で金から発生する光中性子の非等方性パラメータ"**
波戸 芳仁, 桐原 陽一, 佐波 俊哉, 糸賀 俊朗, 中島 宏, 宮本 修治, 浅野 芳裕
原子力学会春の年会(2018)予稿集, 2018.3.26-28 大阪大学吹田キャンパス.
13. **"光中性子エネルギースペクトルに対する入射光子エネルギー依存性の測定"**
佐波俊哉, 桐原陽一, 波戸芳仁, 糸賀俊朗, 中島宏, 宮本修治, 浅野芳裕
原子力学会春の年会(2018)予稿集, 2018.3.26-28 大阪大学吹田キャンパス.
14. **"Development of a variable-bandwidth monochromator for next-generation gamma sources"**
Ryoichi Hajima, Takehito Hayakawa, Toshiyuki Shizuma, Masaru Sawamura, Ryoji Nagai, Shuji Miyamoto, Shunya Matsuba
Proceedings of the 15th Annual Meetings of Particle Society of Japan, THP021 (2018).
15. **"Study of laser Compton gamma-ray source using laser diode array"**
Sho Amano, Taku Yoshikawa, Shuji Miyamoto
Proceedings of the 15th Annual Meetings of Particle Society of Japan, THP107 (2018).
16. **"Material Inspection by positron generated by LCS gamma-ray"**
Shuji Miyamoto, Kento Sugita, Fuminobu Hori, Mititaka Terasawa, Akihiro Iwase, Sho Amano, Satoshi Hashimoto
Proceedings of the 15th Annual Meetings of Particle Society of Japan, THP108 (2018).
17. **"Present status of the NewSUBARU synchrotron light facility"**
Shuji Miyamoto, Yoshihiko Shoji, Satoshi Hashimoto, Yasuyuki Minagawa, Kazuyuki Kajimoto, Yousuke Hamada
Proceedings of the 15th Annual Meetings of Particle Society of Japan, FSP025 (2018).
18. **"How Students Understand the Visual Grade Report"**
Yoshihiko Shoji and Yoshihiro Kokubo
Proc. of 7th International Conference on Learning Technologies and Learning Environments (LTLE2018), IEEE Explore.
19. **"Erosion of fluorinated diamond-like carbon films by exposure to soft X-rays"**
Kazuhiro Kanda, Hiroki Takamatsu, Eri Miura-Fujiwara, Hiroki Akasaka, Akihiro Saiga, and Koji Tamada
Japanese Journal of Applied Physics 57, 045501 (2018)
20. **"Low-temperature activation of boron ion in silicon substrate using B10H14+ cluster and by soft X-ray irradiation"**
Akira Heya, Naoto Matsuo, and Kazuhiro Kanda
Japanese Journal of Applied Physics 57 (2018) 116502,
<https://doi.org/10.7567/JJAP.57.116502>.
21. **"Semimetallicity of free-standing hydrogenated monolayer boron from MgB₂"**
I. Tateishi, N. T. Cuong, C. A. S. Moura, M. Cameau, R. Ishibiki, A. Fujino, S. Okada, A. Yamamoto, M. Araki, S. Ito, S. Yamamoto, M. Niibe, T. Tokushima, D. E. Weibel, T. Kondo, M. Ogata, and I. Matsuda
Phys. Rev. Mater., 3, 024004 (2019) DOI: 10.1103/PhysRevMaterials.3.024004.

22. **"Removal of carbon contamination on oxidation-prone metal-coated mirrors using atomic hydrogen"**
Masahito Niibe, Tetsuo Harada, Akira Heya, Takeo Watanabe, Naoto Matsuo
AIP Conf. Proc. 2054, 060010 (2019). DOI: 10.1063/1.5084641
23. **"Effects of ultraviolet wavelength and intensity on AlGaN thin film surfaces irradiated simultaneously with CF4 plasma and ultraviolet"**
Retsuo Kawakamia, Masahito Niibe, Yoshitaka Nakano, Shin-ichiro Yanagiya, Yuki Yoshitani, Chisato Azuma, Takashi Mukai
Vacuum, 159, 45-50 (2018). doi.org/10.1016/j.vacuum.2018.10.017
24. **"Electron Structure of Boron Doped HOPG: Selective Observation of Carbon and Trace Dope Boron by Means of X-ray Emission and Absorption Spectroscopy"**
Masahito Niibe, Noritaka Takehira, Takashi Tokushima
e-J. Surf. Sci. Nanotech, 16, 122-126 (2018). doi: 10.1380/ejssnt.2018.122
25. **"Laser plasma soft X-ray source in the water window based on cryogenic targets"**
S.Amano
Electronics and Communications in Japan, Vol.101, Issue 1, 55- 60(2018)
26. **"Laser plasma vacuum ultraviolet light source using solid rare-gas targets"**
S.Amano
Jpn. J. Appl. Phys., Vol. 57, 086201(2018)
27. **"Water-window soft X-ray source using cryogenic Ar laser plasma"**
S.Amano
Jpn. J. Appl. Phys., Vol. 57, 126201(2018)
28. **"Plasmon confinement by carrier density modulation in graphene"**
Ngoc Han Tu, Makoto Takamura, Yui Ogawa, Satoru Suzuki, and Norio Kumada
Japanese Journal of Applied Physics 57, 110307 (2018).
29. **"Surface structures of graphene covered Cu(103)"**
Yui Ogawa, Yuya Murata, Satoru Suzuki, Hiroki Hibino, Stefan Heun, Yoshitaka Taniyasu, and Kazuhide Kumakura
Japanese Journal of Applied Physics 57, 100301 (2018).
30. **"Quasi-free-standing monolayer hexagonal boron nitride on Ni "**
Satoru Suzuki, Yuichi Haruyama, Masahito Niibe, Takashi Tokushima, Akinobu Yamaguchi, Yuichi Utsumi, Atsushi Ito, Ryo Kadowaki, Akane Maruta and Tadashi Abukawa
Materials Research Express, Volume 6, Number 1, 016304, 2019
31. **"H2O/O2 Vapor Annealing Effect on Spin Coating Alumina Thin Films for Passivation of Silicon Solar Cells"**
Abdullah Uzum, Hiroyuki Kanda, Takuma Noguchi, Yuya Nakazawa, Shota Taniwaki, Yasushi Hotta, Yuichi Haruyama, Naoyuki Shibayama, and Seigo Ito
International Journal of Photoenergy, Volume 2019, Article ID 4604932, 7 pages
<https://doi.org/10.1155/2019/4604932>
32. **"Water Electrolysis using Flame-Annealed Pencil Graphite Rods"**
Ryuki Tsuji, Hideaki Masutani, Yuichi Haruyama, Masahiro Niibe, Satoru Suzuki, Shin-ichi Honda, Yoshiaki Matsuo, Akira Heya, Naoto Matsuo and Seigo Ito
ACS sustainable chemistry engineering, 7, 5681-5689, 2019

- Takeo Watanabe
HORIBA Technical Journal, Readout, 1, 50-55, 2018.
34. **"Reflectance measurement of EUV mirrors with s- and p-polarization light using polarization control unit"**
Tetsuo Harada, Takeo Watanabe
Proc. SPIE 10809 (2018) 108091T.
 35. **"Development of Absorption-Coefficient-Measurement Method of EUV Resist by Direct-Resist Coating on a Photodiode"**
Shota Niihara, Tetsuo Harada, Takeo Watanabe
Proc. SPIE 10809 (2018) 108091Y.
 36. **"Fabrication of High-Aspect-Ratio Transmission Grating Using DDR Process for 10-nm EUV Resist Evaluation by EUV Interference Lithography"**
Mana Yoshifuji, Shota Niihara, Tetsuo Harada, and Takeo Watanabe
J. Photopolym. Sci. Technol. 31 (2018) pp. 215-220.
 37. **"Synthesis and Property of Tannic Acid Derivatives and Their Application for Extreme Ultraviolet Lithography System"**
Hiroto Kudo, Shizuya Ohori, Hiroya Takeda, Hiroki Ogawa, Takeo Watanabe, Hiroki Yamamoto, Takahiro Kozawa
J. Photopolym. Sci. Technol., 31, 221-225 (2018).
 38. **"In-Situ Measurement of Outgassing Generated from EUV Metal Oxide Nanoparticles Resist During Electron Irradiation"**
Seiji Takahashi, Hiroko Minami, Yoko Matsumoto, Yoichi Minami, Mikio Kadoi, Atsushi Sekiguchi, Takeo Watanabe
J. Photopolym. Sci. Technol., 31, 257-260 (2018).
 39. **"Synthesis of Hyperbranched Polyacetals Containing C-(4-t-butylbenz)calix[4]resorcinarene: Resist Properties for Extreme Ultraviolet (EUV) Lithography"**
Hiroto Kudo, Mari Fukunaga, Kohei Shiotsuki, Hiroya Takeda, Hiroki Yamamoto, Takahiro Kozawa, Takeo Watanabe
Reactive and Functional Polymers, 131, 361–367 (2018).
 40. **"Ferromagnetic resonance of Ni wires fabricated on ferroelectric LiNbO₃ substrate for studying magnetic anisotropy induced by the heterojunction"**
Akinobu Yamaguchi, Akiko Nakao, Takuo Ohkochi, Akira Yasui, Toyohiko Kinoshita, Yuichi Utsumi, Tsunemasa Saiki and Keisuke Yamada
AIP Advances 8, 056411 (2018).
 41. **"Heterojunction-induced magnetic anisotropy and magnetization reversal of Ni wires on LiNbO₃ substrate"**
Akinobu Yamaguchi, Takuo Ohkochi, Akira Yasui, Toyohiko Kinoshita, and Keisuke Yamada
Journal of Magnetism and Magnetic Materials, 453, 107-113 (2018).
 42. **"環境分析や食品安全のための高次ナノ構造体を用いた微量分子検出システムの検討"**
山口明啓, 福岡隆夫, 内海裕一
電気学会誌 E 部門誌 Vol. 138, No. 5, pp. 191-197 (2018).
IEEE Transaction on Sensors and Micromachines Vol. 138, No. 5, pp. 191-197 (2018).
 43. **"Study on fabrication of molecular sensing system using higher-order nanostructure for environmental analysis and food safety"**
Akinobu Yamaguchi, Takao Fukuoka, Yuichi Utsumi

Electron Comm. Jpn. Vol. 101, pp. 38-44 (2018).

44. **"5.8 GHz (2.45 GHz) Microwave Applicator Using Post-Wall Waveguide"**
"ポスト壁導波路を用いた 5.8 GHz (2.45 GHz) マイクロ波アプリケーション"
Yu Nishie, Mitsuyoshi Kishihara, Akinobu Yamaguchi, Yuichi Utsumi
Journal of Japan Society of Electromagnetic Wave Energy Applications, Vol. 2, pp. 18-25 (2018)
日本電磁波エネルギー応用学会論文誌, Vol. 2, pp. 18-25 (2018)
45. **"Fabrication of Integrated PTFE-Filled Waveguide Butler Matrix for Short Millimeter-Wave by SR Direct Etching"**
Mitsuyoshi Kishihara, Masaya Takeuchi, Akinobu Yamaguchi, Yuichi Utsumi, Isao Ohta
IEICE Transactions on Electronics, Vol.E101-C, No.6, pp.416-422 (2018)
46. **"Development of a high-sensitive electrochemical detector with micro-stirrer driven by surface acoustic waves"**
Hiroaki Sakamoto, Hiroki Kitanishi, Satoshi Amaya, Tsunemasa Saiki, Yuichi Utsumi, Shin-ichiro Suye
Sensors and Actuators B: Chemical, Volume 260, 1 May 2018, Pages 705-709 (2018)
47. **"Nano-polycrystalline diamond synthesized from neutron-irradiated highly oriented pyrolytic graphite (HOPG),"**
Mititaka Terasawa, Shin-ichi Honda, Keisuke Niwase, Masahito Niibe, Tomohiko Hisakuni, Tadao Iwata, Yuji Higo, Toru Shinmei, Hiroaki Ohfuji, Tetsuo Irifune, Diamond & Related Materials, 82, 132-136 (2018).
48. **"Quenchable compressed graphite synthesized from neutron-irradiated highly oriented pyrolytic graphite in high pressure treatment at 1500 °C "**
Keisuke Niwase, Mititaka Terasawa, Shin-ichi Honda, Masahito Niibe, Tomohiko Hisakuni, Tadao Iwata, Yuji Higo, Takeshi Hirai, Toru Shinmei, Hiroaki Ohfuji, Tetsuo Irifune, Journal of Applied Physics, 123, 16 (2018).

(2) International meetings

1. **"Photoneutron measurements for IAEA CRP on updating the current photonuclear data library"** (Oral)
I. Gheorghe, H. Utsunomiya, T. Ari-izumi, D. Takenaka, S. Belyshev, K. Stopani, V. Varlamov, D. Filipescu, M. Krzysiek, G. Tveten, T. Renstrøm, D. Symochko, H. Wang, G. Fan, S. Miyamoto
Nuclear Photonics 2018, 24-29 June 2018, Brasov, Romania.
2. **"Research Project on Laser-Driven Neutron sources and applications at ILE, Osaka University"** (Poster)
M. Nakai, Y. Arikawa, A. Yogo, Y. Abe, Y. Kato, S. Matsubara, S. Tosaki, K. Koga, N. Iwata, H. Nagatomo, A. Moracel, K. Mima, Y. Otake, S. Miyamoto, H. Nihsimura, S. Sakabe and S. Inoue
Nuclear Photonics 2018, 24-29 June 2018, Brasov, Romania.
3. **"Non-distractive Inspection of Material Defect by Positron Generated by Laser Compton Scattering Gamma-ray Beam"** (Oral)
S. Miyamoto, K. Sugita, M. Terasawa, F. Hori, A. Iwase, S. Amano and S. Hashimoto
Nuclear Photonics 2018, 24-29 June 2018, Brasov, Romania.
4. **"Development of a positron annihilation measurement system by implantation of 17 MeV gamma beam into bulk materials"** (Oral)
K. Sugita¹, S. Miyamoto, M. Terasawa, A. Iwase, K. Umezawa, F. Hori
International Conference on Positron Annihilation, ICPA18, Orlando, August 19-24 (2018).
5. **"Photoneutron Cross Section Measurements for 165Ho by Direct Neutron-Multiplicity Sorting at NewSUBARU"** (Oral)
M. Krzysiek, H. Utsunomiya, I. Gheorghe, D. M. Filipescu, T. Renstrøm, G. M. Tveten, S. Belyshev, K. Stopani, H. Wang, G. Fan, Y-W. Lui, D. Symochko, S. Goriely, A-C. Larsen, S. Siem, V. Varlamov, B. Ishkhanov, T. Ari-izumi, S. Miyamoto
Zakopane Conference on Nuclear Physics, 26th August to 2nd September 2018, Zakopane, Poland.
6. **" γ -ray Strength Functions and Partial GDR Cross Sections in the IAEA Photonuclear Data Project"**
H. Utsunomiya, I. Gheorghe, D.M. Filipescu, K. Stopani, S. Belyshev, T. Renstrøm, G.M. Tveten, S. Goriely, Y.-W. Lui, T. Ari-izumi, S. Miyamoto, V. Varlamov, B. Ishkhanov, A.C. Larsen, S. Siem
6th International Workshop on Compound-Nuclear Reactions and Related Topics, CNR18, Berkeley, September 24-28 (2018).
7. **"NewSUBARU BL05 - A industrial analysis beam line in soft and tender X-ray region"** [2P059]
Takayuki Hasegawa, Masaharu Uemura, Tohru Awane, Noboru Fukada, Kazuhiro Kanda, Sei Fukushima
ICG Annual Meeting, 2018.9.23-26, Pacifico Yokohama
8. **"Local structure analysis of Si-containing DLC films by X-ray absorption spectroscopy"** [key note]
Kazuhiro Kanda
The 3rd SLRI-NUT-SIAT Colloquium 2018, 2018.11.21, Synchrotron Light Research Institute, NakhonRatchasima, Thailand
9. **"¹H NMR Detection on Nitrogen Terminated Diamond by Shallow Nitrogen Vacancy Centers"** [EP09.03.03]
Takahiro Sonoda, Sora Kawai, Hayate Yamano, Jorge J. Buendia, Taisuke Kageura, Yu Ishii, Kiro Nagaoka, Ryosuke Fukuda, Takashi Tanii, Moriyoshi Haruyama, Keisuke Yamada, Shinobu Onoda, Wataru Kada, Osamu Hanaizumi, Alastair Stacey, Kazuhiro Kanda, Masaharu Uemura, Tokuyuki Teraji, Junichi Isoya, Shozo Kono and Hiroshi Kawarada

MRS Fall Meeting & Exhibit, 2018.11.25-30, the Hynes Convention Center Boston, Massachusetts, USA

10. **"Development of On-site Cleaning Method of Carbon Contamination with Atomic Hydrogen"**
Masahito Niibe, Takashi Tokushima, Tomohiko Kono, Yusuke Hashimoto, Yuka Horikawa, and Hiroaki Yoshida
The 23rd Hiroshima International Symposium on Synchrotron Radiation, Higashi-Hiroshima, 7-8, March 2019.
11. **"Effect of Atmospheric-Pressure O₂ Plasma-Assisted Annealing on Photocatalytic Activity of TiO₂ Nanoparticles"**
Yuki Yoshitani, Retsuo Kawakami, Hirofumi Koide, Naoki Takami, Masahito Niibe, Yoshitaka Nakano, Chisato Azuma and Takashi Mukai
Proceedings of International Symposium of Dry Process 2018, 255-256, Nagoya, Nov. 2018.
12. **"Hydrophilic Modification of Polypropylene Film Surfaces Treated by Atmospheric-Pressure Air Plasma Jet"**
Retsuo Kawakami, Yuki Yoshitani, Kimiaki Mitani, Naoki Takami, Hirofumi Koide, Norihiro Sugimoto, Masahito Niibe, Yoshitaka Nakano, Chisato Azuma and Takashi Mukai
Proceedings of International Symposium of Dry Process 2018, 253-254, Nagoya, Nov. 2018.
13. **"Water Electrolyzing Catalyst of Pt and Fe, Ni, Ru-O Catalysts Deposited by Flame-Annealing on Carbon Electrode"**
R. Tsuji, H. Masutani, M. Niibe, Y. Haruyama, A. Heya, S. Nakajima, N. Matsuo, H. Fujisawa, S. Honda, S. Ito
2018 Annual Nanotechnology Conf., Viena, Austria, Sep. 3-5 2018.
14. **"Water Electrolysis using Flame-Annealed Pencil Carbon Electrode"**
H. Masutani, R. Tsuji, M. Niibe, A. Heya, N. Matsuo, Y. Matsuo, S. Honda, S. Ito
2018 Annual Nanotechnology Conf., Viena, Austria, Sep. 3-5 2018.
15. **"Removal of carbon contamination on easily-oxidizable-metal coated mirrors for synchrotron radiation beamline using atomic hydrogen"**
Masahito Niibe, Tetsuo Harada, Akira Heya, Takeo Watanabe, Naoto Matsuo
Inter'l. Conf. Hot Wire & Initiated Chemical Vapor Deposition (HWCVD10), Kitakyushu, Japan, 3-6, Sep. 2018.
16. **"Removal of carbon contamination on oxidation-prone metal-coated mirrors using atomic hydrogen"**
Masahito Niibe, Tetsuo Harada, Akira Heya, Takeo Watanabe, Naoto Matsuo
Inter'l. Conf. Synchrotron Rad. Instrumentation (SRI 2018), Taipei Taiwan, 10-15, June 2018.
17. **"Cryogenic-Ar laser-plasma-source"**
S.Amano (Invited)
World Congress on Plasma Science and Technology (WCPST2018), Stockholm, Sweden, November 4-7, 2018.
18. **"Growth Process of Hexagonal Boron Nitride in the Diffusion and Precipitation Method Studied by X-ray Photoelectron Spectroscopy"**
Satoru Suzuki, Yuichi Haruyama
14th Int. Conf. Atomically Controlled Surfaces and Interfaces (ACSIN14), Sendai, October 22, 2018.

19. **"Quasi-Free-Standing Monolayer Hexagonal Boron Nitride on Ni Studied by XAS, XES, and PEEM"**
 Satoru Suzuki, Yuichi Haruyama, Masahito Niibe, Takashi Tokushima, Akinobu Yamaguchi, Yuichi Utsumi, Atsushi Ito, Ryo Kadowaki, Akane Maruta, and Tadashi Abukawa
 International Workshop on Trends in Advanced Spectroscopy in Materials Science (TASPEC), Hiroshima, October 6, 2018.

20. **"Evaluation on the molecular orientation in photoreactive liquid crystalline polymer films by NEXAFS spectroscopy"**
 Y. Haruyama, M. Okada, M. Kondo, and N. Kawatsuki
 14th International Conference on Electron Spectroscopy and Structure (ICESS-14), ShanghaiTech University, Shanghai, China, October 8, 2018

21. **"EUV Application Research at NewSUBARU"**
 T. Watanabe and T. Harada
 Optics and Photonics International Congress, Yokohama, 2018/4/23-27. (Invited)

22. **"Synthesis and Property of Tannic Acid Derivatives and Their Application for Extreme Ultraviolet Lithography System"**
 Hiroto Kudo, Shizuya Ohori, Hiroya Takeda, Hiroki Ogawa, Takeo Watanabe, Hiroki Yamamoto, Takahiro Kozawa
 The 35th International Conference of Photopolymer Science and Technology, Makuhari Messe, Chiba, Japan, 2018/6/25-28. (Invited)

23. **"In-Situ Measurement of Outgassing Generated from EUV Metal Oxide Nanoparticles Resist During Electron Irradiation"**
 Seiji Takahashi, Hiroko Minami, Yoko Matsumoto, Yoichi Minami, Mikio Kadoi, Atsushi Sekiguchi, Takeo Watanabe
 The 35th International Conference of Photopolymer Science and Technology, Makuhari Messe, Chiba, Japan, 2018/6/25-28.

24. **"Fabrication of High-Aspect-Ratio Transmission Grating Using DDR Process for 10-nm EUV Resist Evaluation by EUV Interference Lithography"**
 Mana Yoshifuji, Shota Niihara, Tetsuo Harada, and Takeo Watanabe
 ICPST35, Chiba, Japan, 2018/6/25-28.

25. **"Photopolymer Technology for Extreme Ultraviolet Lithography"**
 Takeo Watanabe, Tetsuo Harada
 Polymer World Congress, Stockholm, Sweden, 2018/9/3-6. (Invited)

26. **"Reflectance measurement of EUV mirrors with s- and p-polarization light using polarization control unit"**
 Tetsuo Harada, Takeo Watanabe
 EUV Lithography Symposium 2018, Monterey, USA, 2018/9/18.

27. **"Development of Absorption-Coefficient-Measurement Method of EUV Resist by Direct-Resist Coating on a Photodiode"**
 Shota Niihara, Tetsuo Harada, Takeo Watanabe
 EUV Lithography Symposium 2018, Monterey, USA, 2018/9/18.

28. **"Research Activities of Extreme Ultraviolet Lithography at University of Hyogo"**

Takeo Watanabe, Tetsuo Harada
Micro Nano Engineering 2018, Copenhagen, 2018/9/24-27.

29. **"Research activity of evaluation tools including soft X-ray optics for the research of EUV lithography at University of Hyogo"**
Takeo Watanabe, Tetsuo Harada
Physics of X-Ray and Neutron Multilayer Structures (PXRNMS) 2018, Paris, 2018/11/7-9.
30. **"Development of EUV Phase Imaging Microscope for Mask-3D-Effect and Defect Evaluation"**
Tetsuo Harada, Takeo Watanabe
MNC2018, Sapporo, Japan, 2018/11/14. (Invited)
31. **"Fabrication of High-Aspect-Ratio Transmission Grating Using DDR Process for 10-nm EUV Resist Evaluation by EUV Interference Lithography"**
Mana Yoshifuji, Tetsuo Harada, Takeo Watanabe
MNC2018, Sapporo, Japan, 2018/11/14.
32. **"Magnetic field dependence of ferromagnetic resonance of Ni wires fabricated on ferroelectric LiNbO₃ substrate for studying magnetic anisotropy induced by the heterojunction"**
A. Yamaguchi, A. Nakao, Y. Utsumi, T. Saiki, Y. Takizawa, T. Ogasawara, K. Yamada
INTERMAG 2018 Conference, Singapore, April 23-27, 2018
33. **"Heterojunction-induced Magnetic Anisotropy of Ni Wires on LiNbO₃ Substrate"**
Akinobu Yamaguchi
5th International Conference of Asian Union of Magnetism Societies (IcAUMS 2018), Jeju, Korea, June 3-7, 2018, (INVITED)
34. **"Dielectrophoresis-controllable aggregation and dispersion of Au nanoparticles-decorated polystyrene beads with SERS-activity"**
Akinobu Yamaguchi, Yuichi Utsumi, Takao Fukuoka
International Conference on Advancing Molecular Spectroscopy, Nishinomiya Campus of Kwansai Gakuin University, Hyogo, Japan, June 30 - July 1, 2018
35. **"The Self-assembly of Gold Nanoparticles is Available to SERS Nanobeacons"**
Takao Fukuoka, Yasushige Mori, Akinobu Yamaguchi
International Conference on Advancing Molecular Spectroscopy, Nishinomiya Campus of Kwansai Gakuin University, Hyogo, Japan, June 30 - July 1, 2018
36. **"The study on magnetization reversal of zebra-stripe domain structure in Ni wires fabricated on a LiNbO₃ substrate"**
A. Yamaguchi, K. Yamada, A. Nakao, T. Saiki, Y. Utsumi and T. Ogasawara
21st International Conference on Magnetism (ICM2018), San Francisco, USA, July 15-20, 2018
37. **"Wire width dependence of ferromagnetic resonance in Ni wires on ferroelectric LiNbO₃ substrate for studying heterojunction-induced magnetic characteristics"**
A. Yamaguchi, A. Nakao, T. Saiki, Y. Utsumi, T. Ogasawara and K. Yamada
21st International Conference on Magnetism (ICM2018), San Francisco, USA, July 15-20, 2018
38. **"The Study on the Generation of Magnetic Anisotropy Induced by the Heterojunction between Ferromagnetic and Ferroelectric Materials"**
A. Yamaguchi, T. Ogasawara, Y. Utsumi, K. Yamada, A. Nakao

23rd International Colloquium on Magnetic Films and Surfaces (ICMFS 2018), UC Santa Cruz, USA, July 22-27, 2018

39. **"Study on magnetic characteristics modulated by Ferromagnetic/Ferro electric heterojunction"**
A. Yamaguchi
The 34th International Conference of Photopolymer Science and Technology
9th JEMS Conference 2018, Mainz, Germany, September 3-7, 2018
40. **"Ferromagnetic resonance study on Ni wire"**
Akinobu Yamaguchi
The 34th International Conference of Photopolymer Science and Technology
Micro Nano Engineering 2018, Copenhagen, Denmark, September 24-27, 2018
41. **"Study on surface acoustic wave actuator utilizing gravity for feeding various kinds of micro-powders"**
T. Saiki, K. Iimura, A. Yamaguchi, M. Takeo, Y. Utsumi, M. Suzuki
Micro Nano Engineering 2018, Copenhagen, Denmark, September 24-27, 2018
42. **"Study on fabrication system of 3D printing or additive manufacturing process using X-ray radiolysis"**
A. Yamaguchi, I. Sakurai, I. Okada, A. Yamaguchi, M. Ishihara, T. Fukuoka, S. Suzuki, Y. Utsumi
Micro Nano Engineering 2018, Copenhagen, Denmark, September 24-27, 2018
43. **"Characteristics of new deep X-ray lithography beamline (BL11) at new SUBARU"**
Masaya Takeuchi, Akinobu Yamaguchi, Yuichi Utsumi
JCK MEMS/NEMS 2018 Conference, Dalian, China, July 13-15, 2018
44. **"Anisotropic pyrochemical etching of PTFE induced by synchrotron radiation irradiation"**
Masaya Takeuchi, Akinobu Yamaguchi, and Yuichi Utsumi
29th Micromechanics and Microsystems Europe Workshop, 28, Smolenice, Slovakia, August 26-29, 2018

(3) Academic degrees

Master of Engineering

Yuta Kajino (University of Hyogo)

放射光利用光電子分光法によるアルミニウムの腐食進行に関する研究

"Aluminum Erosion Analysis Using HAXPES at SPring-8 BL24XU "

Fuki Sato (University of Hyogo)

NewSUBARU BL3 における EUV～VUV 領域用反射率計の開発

"Development of Reflectometer in EUV – VUV Wavelength Region at NewSUBARU BL-03A"

Shota Niihara (University of Hyogo)

高感度 EUV レジスト開発のための軟X線評価手法の開発

"Development of Evaluation Methods in Soft X-ray for High-Sensitive EUV Resis"

Laboratory of Advanced Science and Technology for Industry
University of Hyogo

3-1-2 Kouto, Kamigori, Ako-gun, Hyogo 678-1205 Japan

兵庫県立大学 高度産業科学技術研究所

〒678-1205 兵庫県赤穂郡上郡町光都 3-1-2